NEW IMAGING CAPABILITIES FOR MATERIALS ENABLED BY THE ELECTRON MICROSCOPE PIXEL ARRAY DETECTOR (EMPAD)

A Dissertation

Presented to the Faculty of the Graduate School

of Cornell University

In Partial Fulfillment of the Requirements for the Degree of

Doctor of Philosophy

by

Kayla Nguyen

December 2018

NEW IMAGING CAPABILITIES FOR MATERIALS ENABLED BY THE ELECTRON MICROSCOPE PIXEL ARRAY DETECTOR (EMPAD)

Kayla Nguyen, Ph. D.
Cornell University 2018

Transmission electron microscopy is a ubiquitous tool for materials and biological characterization from the micron to atomic scales. While the most common use of transmission electron microscopy is to determine atomic-scale structures, from the protein signatures of Alzheimer's disease to the arrangement of atoms within a transistor, the scattered electron beam encodes a wealth of information about the structure, chemistry, electrical, optical, and magnetic properties of matter. Conventional electron detectors, however, discard much of this information. A next frontier of atomic scale characterization of matter will be to detect, analyze, and utilize these new scattering signals. Here, a new generation of direct imaging detectors have already enabled pioneering work for cryo-electron microscopy to solve structures of biomolecules, giving us an atomic-scale view into the intricate workings of life and winning the Nobel Prize in Chemistry in 2017.

To go beyond traditional electron microscopy techniques, new detectors must also be developed for diffraction imaging. During my PhD at Cornell, I helped developed and co-invented the Electron Microscope Pixel Array Detector (EMPAD), a fast, highly efficient "universal" detector for the electron microscope that is designed to

re-capture and harness this missing information. The EMPAD is poised to have broad scientific and technological impact: we have licensed the EMPAD design to FEI, a subsidiary of Thermo Fisher Scientific. Moreover, in the two years since the first paper was published demonstrating the use of the EMPAD, initial studies applying the EMPAD to various materials and biological systems have demonstrated its broad, cross-disciplinary impact. In my dissertation, I will highlight: previous works on diffraction imaging and STEM diffraction detectors currently available in the field (Chapter 1), the EMPAD and its capabilities beyond traditional STEM imaging (Chapter 2), imaging magnetic fields and magnetic phases in FeGe thin films with the EMPAD (Chapter 3), and new physics from ferroelectric polarization vortices (Chapter 4). In Chapter 5, I will discuss the future works that can be done with EMPAD. In fact, it is extremely encouraging to know that the imaging examples described in this thesis only represent a small fraction of the potential impact the EMPAD can achieve for the field of electron microscopy.

BIOGRAPHICAL SKETCH

I believe in order for young girls and women to learn about the power of facing failure with resilience, people must use their success as a platform to expose not only their accomplishments, but also their challenges. I have noticed that many scientists choose to only acknowledge the highlights of their scientific careers, rather than their entire journey. Of course, there are struggles but what a general audience sees are the end results: the Nobel Prize, the MacArthur Genius award etc. These awards are a great honor; however, they do not teach young scientists that they will face challenges and failures throughout their path to success. For these reasons, I want to start off by sharing who I am and what I have struggled with before I discuss my work as a scientist and as an inventor.

Before I was born, my grandfather was a Vietnamese Airforce General who helped the US during the Vietnam war. Because of this, he was a prisoner of war for 17 years in a reeducation camp. I was born while he was gone, in Gia Dinh Province in Ho Chi Minh City, Vietnam. Once he was released in 1992, my family and I gained political asylum and immigrated to America in 1993.

As an immigrant family living in the US, we struggled with social, economic and language barriers. My weekends consisted of either helping my mother clean laundry rooms of apartment complexes or collecting cans from garbage bins with my grandmother to make revenue from recyclables.

Even though my family worked full time low-wage jobs, the pursuit of education was always of the upmost importance to them. So therefore, in addition to working and raising me, my mother attended community college. My mother graduated with a B.S. in Biochemistry from California State University, Fullerton (CSUF) in 2002 at the age of 40. She is the reason I understand the value of hard work. Obstacles and failures never led to her abandoning the things she cared about: providing for her family, raising me and continuing her education. Because of her, I have never felt 'turned away' by failure.

As a student, my grades were always a bit polarizing. Certain subjects like math and physics came naturally to me, but history and Latin were time-consuming and extremely difficult. I was never good at spelling or multiple-choice exams and as a result, I never did well in those classes. As a high school student, I got Cs and Ds in history and Latin, grades that would be appalling to the regular PhD students in physics, chemistry or any type of science.

However, I did know what I was good at, and that was building stuff. As a kid, I would build skateboards or simple experimental contraptions like a mini tornado inside of a coke bottle. These experiences helped build my passion for invention.

I decided to major in physics and attend the University of California Santa Barbara (UCSB) where I was part of a special program called the College of Creative Studies. Here, exams were oral and based on important physical concepts. Because it was an alternative way to test compared to written exams, I was able to thrive as an undergraduate physics student. For my undergrad research project, I built an

electrostatic force microscopy set-up that could image the surface charges of organic photovoltaics under laser illumination, further extending my passion for invention.

After I graduated from UCSB, I came to Cornell University to pursue my PhD under Professor David Muller. I struggled a lot when I first started my PhD. I had difficulty recognizing the differences between letters, shapes and objects and completing timed exams. These weaknesses made it challenging for me to perform at the level the PhD program required and in effect, I did not perform as well as my peers.

Professor Muller noticed that although I understood the material and the physics extremely well, I still had problems differentiating between letters, shapes and objects. By his suggestions and support, I tested for ADHD. I instead, found out that I had a vision processing disorder. I knew that I always had issues disentangling similar visualizations, but I thought that if I worked hard enough, am careful enough or found alternative methods of studying, I could overcome these barriers.

In addition, even after my diagnosis of the disorder, my family and friends told me that what I had was normal. They emphasized that everyone struggles with some sort of visualization problem, whether it was right-left handedness or shapes and objects. They told me that I did not have a learning disability otherwise I would not have gotten into a PhD program; I didn't need help. This lack of support and acknowledgement of my diagnosis made it difficult for me to accept and feel comfortable with it.

Even worse, although I could understand why certain things would take me twice as long to accomplish in comparison to other students, I was still embarrassed by

my challenges. So much so, that I ended up not vocalizing my disability to the other professors and staff in the department. Instead of asking for help, I continued with my struggles – this became the biggest regret of my life.

Over time, I realized that if I talk about my struggles with vision processing disorder, it can let other young people with learning disabilities know that they are not alone and that they should not feel ashamed.

Graduate school requires an immense amount of work and mental prowess. I knew my vision processing disorder would make achieving success more challenging, but I told myself I could not give up. Through hard work and dedication, myself and a group of amazing scientists co-invented the electron microscope pixel array detector (EMPAD), an electron diffraction detector.

The EMPAD, enables us to observe what happens inside computer chips, proteins important to Alzheimer's disease or nanocomposite in paintings like "The Scream" by Edvard Munch. The EMPAD accomplishes these tasks by extracting structural, optical, chemical, electronic and magnetic properties from atoms. This same data could also be used to create faster computers, cheaper electric cars, better biological scoping/treatment, art conservation and drugs that we design to cure diseases.

I hope my story as a child who grew up in a predominantly immigrant community with a learning disability can inspire people not to give up on their dreams and goals no matter what life gives them. My perseverance has led to many amazing opportunities including: receiving the Lemelson-MIT Student Prize award and licensing

EMPAD to ThermoFisher Scientific, which enabled it to be sold around the world. This October, I will also travel to Vienna, Austria to give a TEDxVienna talk about EMPAD. Additionally, after I receive my PhD, I will continue my research at the University of Illinois in Urbana Champaign.

So much of my success has been made possible because of the incredible support I received from professors and mentors throughout my journey. They understood, and taught me, that learning comes in different forms and every brain is wired to retain information in its own way. Without their efforts to accommodate for my learning needs, I could not have finished my PhD or become a scientist. Ultimately, my hope is that both my research and personal story can help and inspire people everywhere.

Dedicated To Mananya Tantiwiwat

ACKNOWLEDGMENTS

"If there is no struggle, there is no progress." – Frederick Douglass

The last 7 and a half year in Ithaca has been somewhat of an adventure, one that I will remember for the rest of my life. I am grateful to Professor David Muller who taught me everything there is to know about patience and other weird things that I was curious about like electron microscopy. Thank you for enduring my sense of humor, incredibly awesome, lame jokes and teaching me that my impulsive actions have serious consequences. Aside from that, thank you for kicking me out of your research group (with a PhD).

I would also like to acknowledge the tool managers at Cornell, John Grazul, Mick Thomas, Mariena Ramos, and of course Don Werder. You guys are seriously the best. In addition, thank you to all the Muller group students, current and past, Lena, Robbie, Peter, Huolin, Megan, Barnaby, Elliott, Yi, Paul, Zhen, Ela, Ariana, Celesta, Michael, Pratiti, Swathi, Jack and Yimo. I would especially like to thank Pinshane for giving me a job after graduation. Hopefully when I get kicked out of your group, I would have some other entity paying my salary or hourly wages. The Kourkoutis Group, David B, Michael Z, Ismail, and Katie, thank you for all your help and support. Nev and Dotti Pak, I hope you guys get to see this one day, thank you for being awesome human beings and Mark Walsh, thank you for letting me teach diffraction physics to teachers and young students, the experiences I've gathered through the CCMR outreach programs have extremely affected me as a scientist, for the better of course. I would like to thank all the people at FICCC especially Panle, Mavis, and Hildy who taught me that success is not worth the sacrifice if the cost is too great. Professor Abruna,

Professor DiSalvo, Professor Gruner, Professor Fuchs, Professor Ralph, and Professor Thuc-Quyen Nguyen, thank you for listening to me and encouraging me to stick to science even when the going gets hard. I would like to highlight my best friends at Cornell, Rebecca, Pamela, Johary, Camille and Eli, and my best friends back in California, Vicky, Janet, Chauan, and Victoria, for giving me the encouragement to continue working through my PhD every day.

Thank you to my family for their love and support always.

Finally, I am so happy that I had the opportunity to study at Cornell and meet Nikolay, who has given me comfort, confidence and compassion. Nik, I love you with all my heart.

TABLE OF CONTENTS

LIST OF TABLES

LIST OF FIGURES

CHAPTER 1

INTRODUCTION

Electron microscopy is an important tool for the study of materials either through direct imaging, such as in transmission electron microscopy (TEM), or via observing key relevant regions of the electron scattering distribution, as in scanning transmission electron microscopy (STEM). Historically, TEM has been the purview of imaging detectors, where the information is recorded in a single snapshot. STEM has usually been performed using fixed geometry sensors that monitor one or, at most, a few relevant but fixed regions of the scattering distribution. Dynamic range and frame throughput limitations have severely limited imaging devices for STEM work in the past.

In this chapter, we highlight previous works done for diffraction imaging where we review advances in detector technology for electron microscopy starting from film emulsion, leading to charge couple devices and then eventually the hybrid mixed-mode technology of the electron microscope pixel array detector (EMPAD) specifically made for STEM imaging. Among the detectors that are currently available today for electron microscopy – we highlight a handful of detectors that have capabilities such as fast readout and high dynamic range important for diffraction imaging: the pnCCD [1], monolithic active pixel sensors – MAPS [2], Medpix3 [3] and EMPAD [4]. We investigate their specifications in regards to modulation transfer function (MTF). In the following plots for different detectors, the MTF is obtained by a knife edge resolution

method where the MTF is plotted as a function of spatial frequency for increasing beam energies. From which, we can develop the background and intuition to further push detector development for future generations.

Detector	Sensor Size	Pixel size (um)	Readout Speed (fps)
pnCCD	264 x 264	48	1150 (4xbinning 4000)
MAPS - K2 Summit	3838 x 3710	5.0	400
Medipix3	256 x 256	55	2032
EMPAD	128 x 128	150	1167

Table 1.1 represents the detectors in the following sections in details.

1.1 Background: From Film to CCD

Historically, advances in imaging technology, when applied to electron microscopy, have enabled new possibilities in materials analysis. Emulsion films provided good spatial resolution and contrast but non-linear response, low dynamic range, chemical development and post processing made the imaging plate a better alternative [5]. Although imaging plates require post processing, the readout is digital and they provide good linear response and dynamic range, but with limited signal-to-noise ratio (SNR) [5] . The offline nature of processing emulsion films and imaging plates posed some limitations on advanced imaging experiments demanding automated and high throughput data acquisition [6]. Charge couple devices (CCDs) [7] are widely used in such applications. Direct conversion in a CCD has excellent single electron sensitivity but suffers with limited dynamic range as the charge created by only a few primary electrons per pixel saturates the CCD. Scintillator-coupled CCDs reduce the average recorded signal per microscope electron, extending the dynamic range per frame but

suffer from limited spatial resolution due to electron and optical scattering in scintillator screens [5, 8, 9],

1.2 pnCCD

The pnCCD is a pn-junction charge-coupled device detector based on the principle of sideward depletion used in silicon drift detectors (SDD [1]. Here, primary electrons enter the detector through an ultra-thin entrance window which allows for sufficient acquisition at low electron energies down to 5 keV. By avoiding the metal oxide semiconductor (MOS structures), the pnCCD is radiation hard where the 450 um thick silicon bulk allows for the high energy primary electrons to be deposited onto the detector. The advantage of the pnCCD is that the MTF is optimal at low beam energies. However, because the pixel size is 55 um, the interaction volume causes a lateral spread charge into adjacent pixels at higher beam energies. Therefore, at higher beam energies 200-300 keV, the MTF is greatly decreased (Figure 1.1).

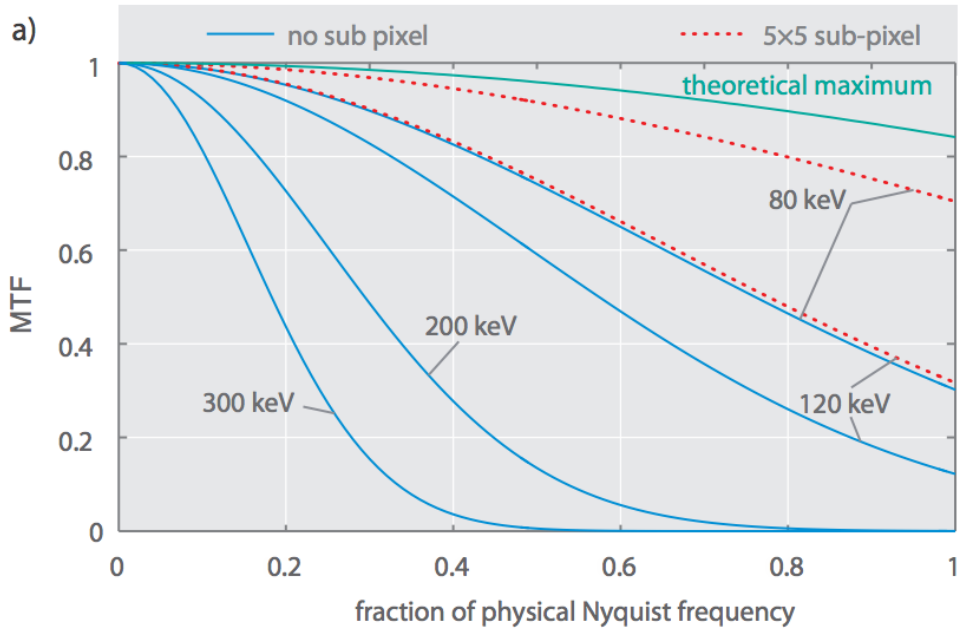

Figure 1.1: (a) Modulation transfer functions for TEM electron energies of 80 keV, 120 keV, 200 keV and 300 keV with no sub-pixel resolution (blue solid lines). The MTFs with a 5 × 5 sub-pixel resolution are shown for electron energies of 80 keV and 120 keV (red dotted lines) [1].

Figure 1.1 also shows that the MTF is close to optimal when using the 5x5 subpixel resolution application at low beam voltages. Although this increases the MTF for lower beam energies, higher beam energies of 200-300 keV still performs at lower MTF due to the lateral spread of electrons to adjacent pixels. In addition, although (Ryll, 2016) states that the dynamic range of the pnCCD can sustain a large number of "signal" electrons (i.e. electron-hole pairs) . Each primary electron generates ~20,000 signal electrons per primary electron, and the maximum number of electrons per well that can be accommodated linearly is 160,000, resulting in a 8 electrons per pixel/frame, or 15 electrons/pixel/frame with distortions. Typical frame times are 0.25-1 ms, resulting in

saturation currents on the order of 5 fA/pixel. These values will be reduced for increased beam voltages. Typical electron microscope beam currents are 10-1000 pA for comparison. Figure 1.2 shows the need for the use of a beam stop when observing the CBED pattern on the JEOL-200ARMF [10]. Here, the intensity of the bright field disk causes saturation of the diffraction pattern and therefore, the lower scattered signal for high angles cannot be observed at the same time along with the intensity of the central disk. By applying a beam stop, this limits the pnCCD capabilities for ptychography and other imaging techniques that require the full diffraction pattern. The pnCCD detector is therefore most efficient at lower beam energies and lower doses.

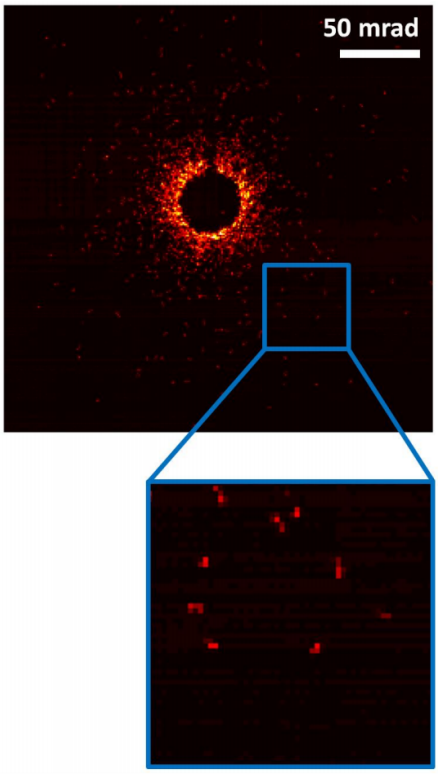

Figure 1.2: Due to the intensity differences of the bright field disk and the outer scattered electrons, a beam-blanker was used to block the bright field disk [10].

1.3 Monolithic Active Pixel Sensors (MAPS)

Recent developments in monolithic active pixel sensors (MAPS) have made them a high-throughput alternative to CCDs. The MAPS detector is a direct electron detection system incorporating sensor and readout electronics in a single layer and using standard Complementary Metal Oxide Semiconductor (CMOS) technology, originally designed as vertex detectors for particle accelerators. This enables the MAPS detector to have large numbers of pixels (4K by 4K) with small pixel size of 5 um. With smaller pixels, this gives a larger field of view with the same active area, good for angular resolution and direct TEM imaging. In the MAPS detector, the active region is very thin typically 8 um and at 200-300 keV, the lateral spread of electrons is 1-2 um [11]. Due to this, MAPS detector do not have large signal contributions from laterally scattering at beam energies higher than 200 keV and can be used to image systems that require 300 keV beam energy.

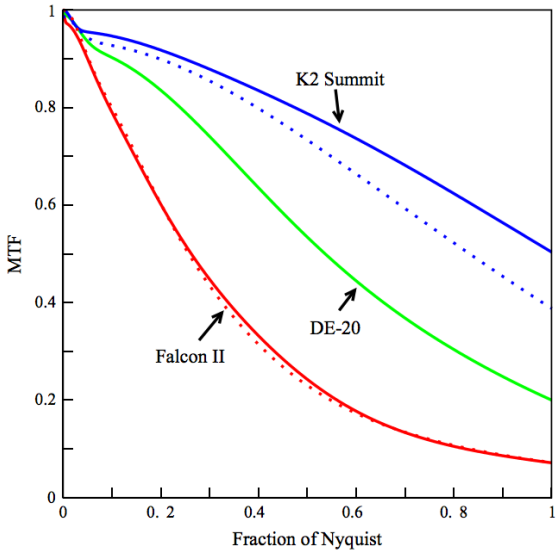

Figure 1.3: A recent review comparing the performance of commercial MAPS detectors

is given by McMullan et. al., 2014. Here, different MAPS detectors, Gatan K2 Summit, DE-20 and Falcon II are compared to each other at 300 keV. From the detectors available, the Gatan K2 shows the highest MTF.

To understand how the detectors response to the fluctuation of energy loss, we investigate straggling, the intrinsic variability of the energy loss by the electron passing through a thin detector, by fitting the probability distribution function, $p(\Delta)$ of the electron events, Δ, from each of the three detectors, to a scaled Landau distribution $\phi(\lambda)/\xi$ where $\lambda=[\Delta-(\Delta_{mp}-\xi\lambda_0)]/\xi$. Here, $\lambda_0=-0.2228$ is the position of the maximum of $\phi(\lambda)$, ξ is a fitted width parameter and Δ_{mp} is the position of the most probable value of $p(\Delta)$. In Figure 1.4 a-c, random areas for detectors a) DE-20, b) Falcon II and the c) K2 Summit at 300 keV of 256x256 pixels show individual electron events. The measured probability distributions for the integrated signal of individual single electron events (Figure 1.4 a-c) are plotted as a function of signal for each of the three detectors; their plots compare relatively well to the Landau distribution (Figure 1.4d). The small shoulder to the left of the distribution at low Δ is due to the inclusion of noise events.

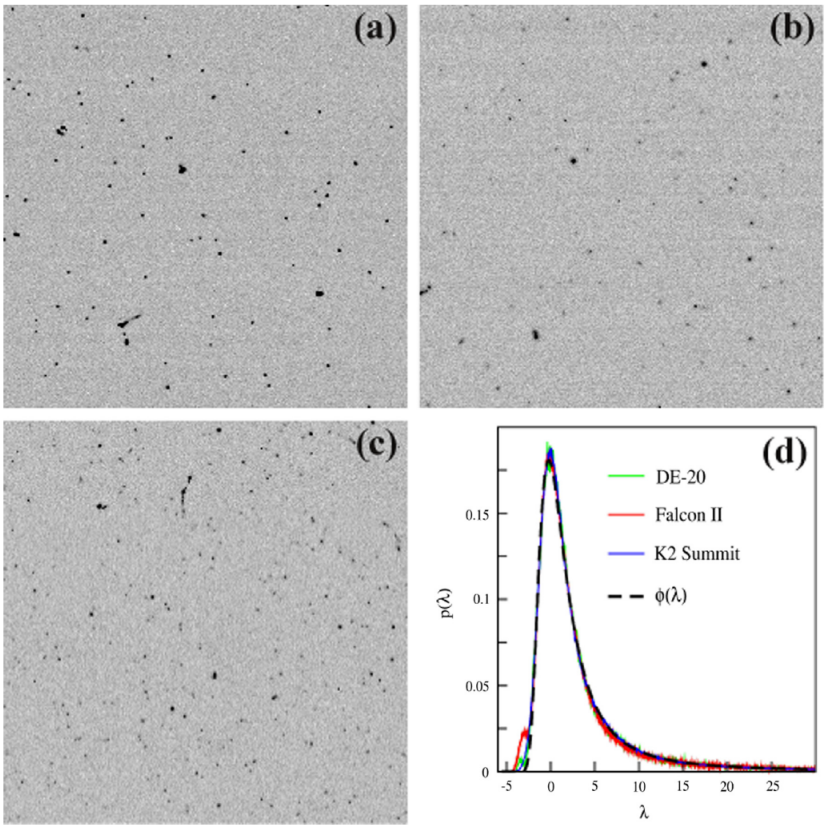

Figure 1.4: Randomly chosen 256×256 areas from single frames showing individual 300 keV electron events as recorded on the (a) DE-20, (b) Falcon II and (c) K2 Summit detectors. (d) Landau distribution comparisons of the measured probability distribution from DE-20, Falcon II and K2 Summit detectors.

However, MAPS detector lack the dynamic range needed for diffraction imaging where the central beam is extremely bright compared to the higher scattered angles of the convergent beam electron diffraction pattern (CBED). In addition, MAPS detectors typically work at higher beam energies to avoid damage to the detector at lower beam energies. Here, when beam energies are lowered, the interaction volume stays within the detector where there is more lateral spread to adjacent pixels. Therefore, when

operating at 60 keV, the typical energy used to image atomic layered materials such as graphene, the MAPS detector would experience more lateral spreading in the active layer, damage to the detector, and electron backscattering from the substrate. Due to electron backscattering, MAPS detectors are typically backthinned to less than 50 um. Although using the MAPS detector is not optimal for diffraction imaging, MAPS detectors are extremely well tuned for lose-dose imaging at high beam energies ~300 keV and direct TEM imaging, important advantages for cryo-electron microscopy [2].

1.4 Hybrid Pixel Array Detectors

Hybrid pixel array detectors (PADs) [11-17] while the PADs usually consist of a thick sensor layer (silicon or CdTe) bump-bonded to the silicon readout electronics underneath. PADs combine the efficiency of a fully-depleted diode sensor coupled pixel-by-pixel to a CMOS readout chip which is custom tailored to the imaging problem at hand.

The two PAD design that will be discussed are the dynamic pixel array detector (DPAD) architecture such as the Medipix3 which employs counting the current pulses generated by the incident electrons and the analog pixel array detector (APAD) such as the EMPAD which integrates the total charge generated. Here we discuss the advantages and disadvantages of both types of detection mechanism, where we will go into more depth about the EMPAD in Chapter 2.

1.4.1 Medipix3

The Medipix3 design is originally developed by CERN for proton and particle detection [18]. Here, the DPAD system used in the Medipix3 design employs a pulse counting architecture which yields a very high S/N ratio for single electron hits. For the Medipix3, this is called the Single Pixel Mode (SPM), where the pixels register a count if it exceeds the preset lower threshold dispersion [3]. However, this technique also limits the maximum rate of incoming electrons per pixel to below 10^6 Hz [19]. These detectors work well for imaging at low doses, but saturate quickly when exposed to high fluxes common with diffraction patterns.

In addition, the Medipix3 has a pixel size of 55 um which attributes to a reduction in the MTF with increasing electron energy (Figure 5). From the Figure 1.5, we observe a degradation in the MTF signal with increasing beam energies corresponding to increasing lateral spread in charge where 60 keV – 24 lateral um, 80 keV- 39 um, 120 keV – 83 um and 200 keV – 170 um, reducing the sharpness of the diffraction pattern with increasing beam energy.

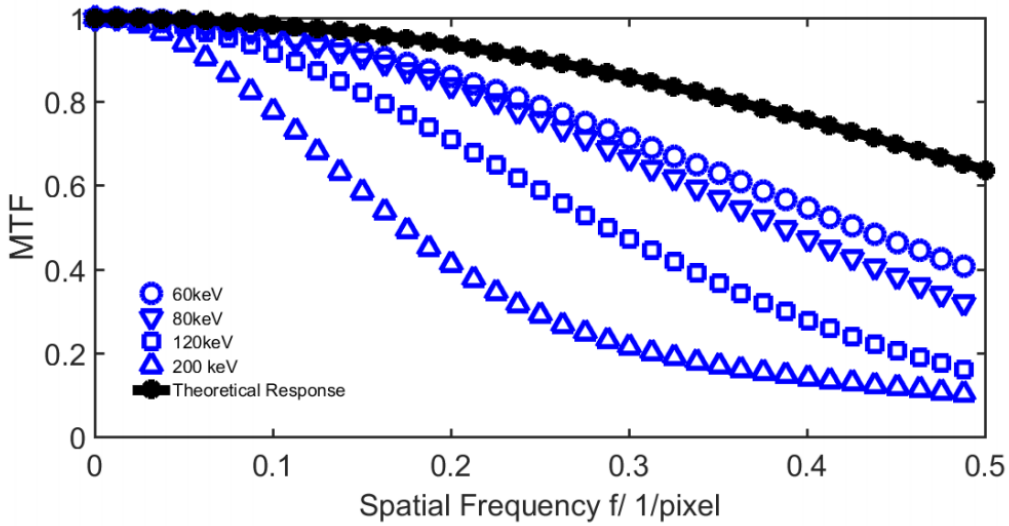

Figure 1.5: MTF vs spatial frequency. Here we observed that with increasing electron beam energies, the MTF decreases due to the lateral spread in charge which leaks to adjacent pixels [3].

1.4.2 EMPAD

For APAD architectures which measure the integrated charge do not need to distinguish individual pulses and can extend the rate limitation many orders of magnitude higher. In this architecture, one could choose an integration stage with either a high gain for good single electron sensitivity, or a low gain for a high dynamic range per frame, but not both.

The EMPAD is derived from the APAD architecture; however, it uses a high-gain charge integration front end combined with in-pixel logic to effectively reset the pixel while integration is ongoing. A concurrent trigger to an in-pixel counter extends

the dynamic range per frame while the high gain amplifier maintains single electron sensitivity. Some of the high rate capability of charge integrating PADs is sacrificed, but it remains several orders of magnitude higher than pulse counting architectures. Details of the EMPAD will be discussed in Chapter 2.

1.5 Discussion of Detector Optimization

There are two main aspects of the detector where trade-offs can be considered: first, how many pixels do we need for a diffraction camera, and second, how many electrons per pixels should we be able to record? To a fair extent, these two questions are coupled. A thick sensor will require large pixels to match the inherent charge spread, but a thicker sensor will also collect electrons far more efficiently. For imaging sensors, a high pixel count is desirable, but as a STEM detector, extra sensor pixels are undesirable because of resulting bandwidth and storage problems for high speed readouts. Moving from a 128×128 pixel sensor to a 256×256 pixel sensor will quadruple the storage requirements per 4D EMPAD-STEM map from 4GB to 16 GB for a simple 256×256 probe position map.

The question of how many sensor element pixels are needed will depend on the measurement planned. For phase reconstruction of the bright field disk using ptychography, there is a diminishing return beyond 16×16 pixel elements for an atomic-sized probe [20]. For COM and its extreme limit of DPC imaging, obviously it is possible to detect very small beam deflections using only 2×2 pixels. The question of

what is the optimum number of pixels has been studied heavily in the optical super-resolution community where the location of fluorescent centers to sub wavelength accuracy is essential. Thompson, Larson and Webb [21], have shown that the optimal ratio of sensor size, *a*, to spot size, *s*, is

$$\left(a/s\right)^4 = 96\pi b^2/N\,, \qquad \text{-(2)}$$

where N is the number of primary counts in the beam and *b* is noise/pixel in primary counts. Here *s* is the standard deviation of the point spread function, which is assumed to be Gaussian. A similar analysis with a different scaling coefficient would hold for a top hat function. The main trend is that for a noisy detector, fewer elements are desirable, and as the detector's signal/noise ratio improves, more detector elements can be considered. From previous inferences of center of mass calculations [4], the EMPAD operating at 200 keV with N=1000 primary electrons would be optimal with 16 pixels for locating the center of mass. At 10,000 electrons, this grows to 28 pixels, with an accuracy of 1% of the spot size, although the curve is relatively flat vs number of pixels, with the root mean square error given by [21]

$$\langle(\Delta x)^2\rangle = \frac{s^2 + a^2/12}{N} + \frac{4\sqrt{\pi}\, s^3 b^2}{aN^2} \qquad \text{(3).}$$

About 16 pixels per diffraction disk is sufficient for tracking the center, thus our 128×128 pixel sensor could record 8×8 diffraction spots in parallel if optimally configured. For differentiating between polarity and tilt contributions to the center of mass signal, imaging diffraction patterns with non-overlapping disks can be very helpful.

Although this analysis is worth keeping in mind as we consider more detailed analyses of diffraction patterns, we observed that we could also analytical derive the precision of our center of mass measurement that is not as dependent on the number on pixels as much as the electron dose, N, and the semi-convergence angle α. From Chapman et. al, 1984 [22], we derived a simple equation based on the convergence angle of the electron beam and the dose in the signal:

$$center\ of\ mass = 0.785\frac{\alpha}{\sqrt{N}} \tag{4}.$$

Derivation is shown in Appendix 1. From the analytical formula in Equation 4, we find that when we increase the number of electrons for our measurement, while keeping the number of pixels above 2, we obtained a more accurate and precise center of mass signal regardless of increasing the number of pixels on our detector. In Chapter 3 we support this claim by performing an iterative simulation to deduce the dependence of dose and the number of pixels on our detector to find the relative error in the standard deviation with Poisson noise. We find that there is little dependence on the number of pixels when perform center of mass measurements compared to the dose (number of electrons) used in deciphering our signal. Therefore, so long as there are more than 10^3 electrons detected, we can measure to a precision of less than >1 % of the shift (see Chapter 3).

For measuring the shift of excess and deficit HOLZ lines, more pixels might be desirable for angular resolution, but the contrast also depends on the number of electrons

per pixel, so large signals and beam are required. Many of the monolithic active pixel sensors (MAPS) use relatively thin active layers and as a result can only hold relatively few (25 to 1000 electrons) primary electrons per pixel, severely limiting their dynamic range, and the angular range that they can record simultaneously. In exchange, the thin layer results in less charge spreading, and can use a smaller pixel size. Our current EMPAD design uses larger and deeper active pixel volumes (150×150×500 microns) which greatly improves the SNR/primary electron, reducing *b* in equations 2 and 3.

One benefit of the thick detector where almost all the energy from each electron is collected by the detector is that the energy distribution is relatively narrow. In contrast, thin transmission detectors which are designed to allow most electrons to pass through with little spatial spread, result in an energy spread that follows a Landau distribution e.g [2]. The Landau distribution has a large straggle and a mean energy is very sensitive to the energy cutoff. Thus charge integration with a thin detector would result in a very noisy signal that would be difficult to quantify. The thin detectors obtain their good signal to ratios by operating in counting mode instead, resulting in both limited dynamic range and low count rates per pixel, but can use a much smaller pixel size.

The thick and thin detectors have very different energy dependences. The point spread increases with primary voltage for the charge-integrating thick detector, which is the reverse to that found for thin sensors operating in counting mode. At higher voltages, less than 100% of the energy is deposited in the thin sensor, leading to reduced

sensitivity but an improved MTF as fewer electrons have an opportunity to scatter within the pixel. In contrast the thick sensor retains a high sensitivity, but exhibits a degraded MTF once the beam spread becomes comparable to the pixel size.

The existing pixel array module was designed for x-ray imaging and no modifications were made to the ASIC or sensor when it was adapted to the present STEM application. Redesign of the pixel array sensor and ASIC are certainly feasible, though by no means trivial. For example, use of high atomic weight sensor materials (e.g., CdTe) could help to increase the pixel count, as per the discussion above, without increasing the detector area or compromising the SNR. Sensors with pixels of a different area and/or thickness are possible, as are ASICs that frame more quickly and have a higher dynamic range. However, it should be noted that pixel array detector design is typically sufficiently expensive (millions of dollars) and time consuming (many person years) that redesign should be approached with a great deal of thought and in response to pressing unfulfilled requirements. Thus, in our opinion, it is likely wisest to gain experience with the present design on many more real materials applications before plunging into a redesign effort of the fundamental MM-PAD module.

With these high-throughput, high-dynamic range imagers one can now envisage that imaging detectors can be routinely applied to STEM applications. While previous PAD designs have been optimized for real-space imaging, where intensity distributions are relatively uniform and a large number of detector pixels are required, recording diffraction patterns for STEM imaging requires both a high dynamic range and good

single-electron sensitivity, which the current design is optimized for, while a high pixel count is less critical.

1.7 Conclusion

In STEM diffraction imaging, the entire scattering image is recorded at each scan point, and can be processed simultaneously extract bright field, dark field, center of mass and differential phase contrast information by defining appropriate regions of interest from the detector. However, much more information is contained within the diffraction patterns than is extracted in the typical bright or dark field analyses. Broadening the set of tools used to fully utilize the scattering images is where the true advantages in applying imaging detectors to STEM will become apparent. Some of these ideas have already been tested in earlier detector designs with the limitations discussed above [23 - 26]. For instance, ptychography for phase recovery that has been demonstrated with CCD detectors [27-28] would benefit from the improved contrast and dynamic range of an EMPAD, as would strain mapping based on nano-beam electron diffraction [25]. For the rest of the thesis, we explore new imaging abilities with the EMPAD using diffraction patterns extracted. From which, we learn how the EMPAD can contribute to a deeper understanding of how the STEM diffraction imaging leading to new physics and scientific breakthroughs.

CHAPTER 2

ELECTRON MICROSCOPE PIXEL ARRAY DETECTOR

Scanning transmission electron microscopy (STEM) has been used to study material and biological properties from nanometer to atomic scale where to observe local structural changes are observed in the sample. In STEM imaging, the electron beam is focused to a sub-angstrom spot which scans over the sample. While an atomic resolution image can be reconstructed, image contrast is constrained by detector configurations where scintillator-based and charge-coupled device (CCD) detectors must integrate the signal collected due to their slow acquisition speeds. In addition, only a single contrast value is extracted at each scan position and any other information about the specimen encoded in the electron diffraction pattern is thrown away. As a remedy, various attempts have been made to record the full electron diffraction pattern at each scan position with CCD or direct electron detectors, but limited dynamic range cause these detectors to saturate or damage at electron beam energies lower than 100keV, and slow acquisition speeds make it hard to collect suitable data in real-time albeit sample drift.

To overcome the imaging constraints posed by conventional detectors, Professor David Muller and Professor Sol M. Gruner formed a collaboration aimed to retrofit an x-ray detector onto an electron microscope. Here, an x-ray detector optimized at 10 keV x-ray energy could also be used for a 200 keV electron source since they have similar interaction profiles. In 2006, the first prototype detector was tested. It consisted

of only 16 by 16 pixels, and it turned out to be short-lived. The scan board, a National Instrument Board, was broken, and after only one experiment, beam damage caused the pixels to saturate too quickly. The electronics and detector were destroyed and only one data set was taken [11]. This experiment demonstrated the challenge posed by the fact that electron sources tend to be thousand times brighter than x-ray sources. An entirely new design was needed in order to have the required sensitivity to capture the full diffraction pattern of the beam, and yet to be able to withstand the high brightness of the central peak.

Learning from the design complications of the previous detector, the project to put a new prototype detector into the electron microscope started again in 2014 with me and my lab mate Robert Hovden (now professor at Univ. of Michigan) and two other staff scientists, Prafull Purohit and Dr. Mark Tate, from Prof. Gruner group. This time we tested a new prototype detector optimized for the free electron laser which could handle the large electron doses required for STEM diffraction imaging. This prototype detector eventually led to the electron microscopy pixel array detector (EMPAD), a 4-dimensional detector used in STEM mode that collects the full electron diffraction pattern at each point in the scan (4-dimensional refers to real space: x and y, and momentum (diffraction) space: k_x and k_y).

2.1 Electron Microscope Pixel Array Detector (EMPAD)

In this chapter, we present a hybrid pixel array detector (EMPAD - electron

microscope pixel array detector) adapted for use in electron microscope applications, especially as a universal detector for scanning transmission electron microscopy. The 128 × 128 pixel detector consists of a 500 μm thick silicon diode array bump-bonded pixel-by-pixel to an application-specific integrated circuit (ASIC). The in-pixel circuitry provides a 1,000,000:1 dynamic range within a single frame, allowing the direct electron beam to be imaged while still maintaining single electron sensitivity. A 1.1 kHz framing rate enables rapid data collection and minimizes sample drift distortions while scanning. By capturing the entire unsaturated diffraction pattern in scanning mode, one can simultaneously capture bright field, dark field, and phase contrast information, as well as being able to analyze the full scattering distribution, allowing true center of mass imaging. The scattering is recorded on an absolute scale, so that information such as local sample thickness can be directly determined. This chapter describes the detector architecture, data acquisition (DAQ) system, and preliminary results from experiments with 80 to 200 keV electron beams.

2.2 Materials and Methods

A pixel array detector (PAD) consists of a pixelated sensor bump-bonded, pixel-by-pixel, to an underlying application specific integrated circuit (ASIC) which processes the charge generated in each sensor pixel. A typical arrangement of a PAD is shown in Figure 2.1.

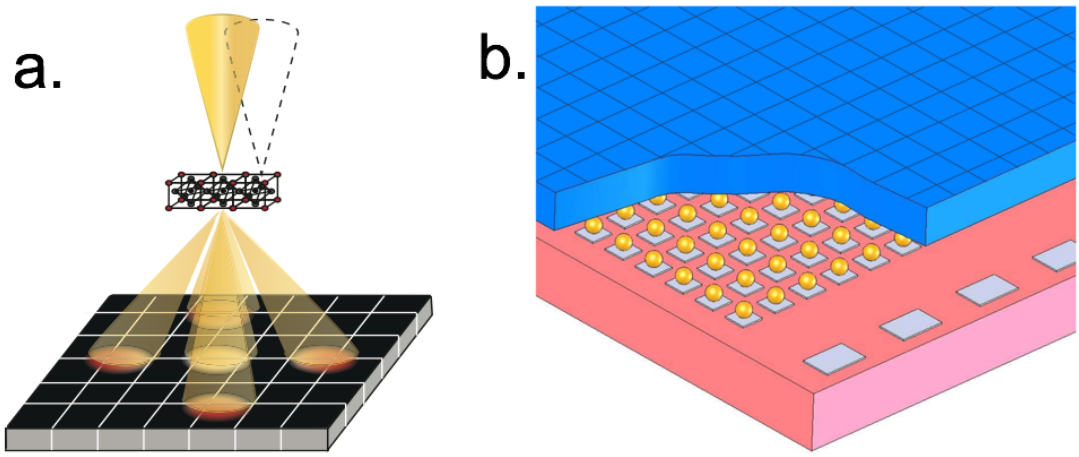

Figure 2.1. a.) Schematic of STEM imaging using the EMPAD in where the beam is stepped at each scan position and the full CBED diffraction pattern is recorded. b) Schematic of the physical structure of the EMPAD. The pixelated sensor (shown in blue with a corner removed) is bump-bonded (solder bumps represented here as gold balls) pixel-by-pixel to the underlying signal processing chip (in pink).

Here the sensor is a 500 μm thick diode array fabricated in high-resistivity silicon to allow for full depletion of the diode with a bias of 150 V (SINTEF, Norway). The ASIC is designed and fabricated using standard CMOS tools in a 0.25 μm process (TSMC, Taiwan). Both layers were originally designed as part of a high-dynamic-range, 128 × 128 pixel x-ray imager known as the mixed-mode pixel array detector (MM-PAD) or the electron microscope pixel array detector (EMPAD) [29 – 32]. This same design turns out to be compatible with electron imaging over a wide primary beam energy range as well. We have tested it for close to a year at up to 200 keV without any obvious degradation in performance.

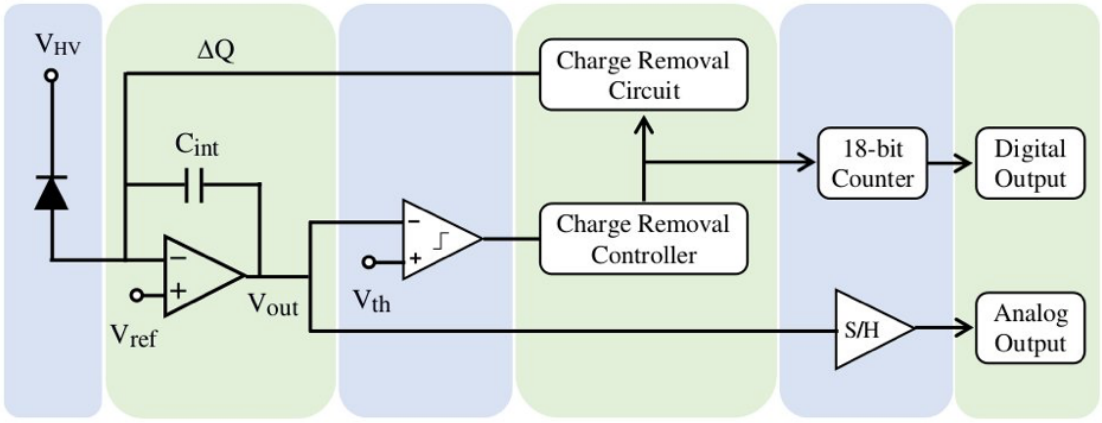

Figure 2.2. Pixel schematic of the EMPAD. Charge generated in the reversed biased diode at left is integrated onto a capacitor, C_{int}. A comparator stage compares the integrator voltage, V_{out}, with a defined threshold, V_{th}. When this voltage is exceeded during exposure, circuitry is triggered which removes a charge, ΔQ, from the integrator, keeping the integrator in its operating range. At the same time, an in-pixel counter is incremented. At exposure end, V_{out} is digitized and combined with the digital output of the 18-bit counter to yield a high-dynamic range value for the pixel signal.

2.2.1 Pixel Array Detector Description

The pixel design, shown in Figure **2.**2, consists of a front-end amplifier that integrates charge coming from the reverse-biased sensor diode onto a feedback capacitor, C_{int}. The output, V_{out}, of the integrator is compared with a pre-defined threshold voltage, V_{th}. The comparator triggers both a charge removal circuit and an 18-bit, in-pixel counter each time the V_{out} exceeds V_{th} during integration. Each charge removal step takes away a calibrated charge, ΔQ, keeping the input amplifier within its

operation range. At the end of integration period, the 18-bit digital value from the counter and the residual analog voltage are read. A field programmable gate array (FPGA) applies a calibrated scale factor to the 18-bit digital value and combines the result with the 12-bit digitization of the analog residual to provide a 30-bit output to the acquisition computer. The value of C_{int} was chosen to be 50 fF for this device to provide high gain for single 8 keV X-ray sensitivity. A future detector designed specifically for electron imaging could easily use a larger integration capacitor to increase the maximum rate of incoming electrons while still maintaining single electron sensitivity.

For readout, the 128 × 128 pixel array is divided into 8 banks of 128 × 16 pixels each. Banks are read in parallel, with pixel outputs buffered sequentially through 8 analog to digital converters and 8 digital I/O lines for the in-pixel counter data. The FPGA is used to control exposure and to receive analog and digital data from the detector. The entire detector can frame continuously at up to 1.1 kHz.

2.2.2 Detector Assembly

Figure 2.3 shows a conceptual design sketch of the prototype detector assembly. The system is composed of three main components – the detector housing on the microscope, the detector control unit (DCU), and a data acquisition and control PC.

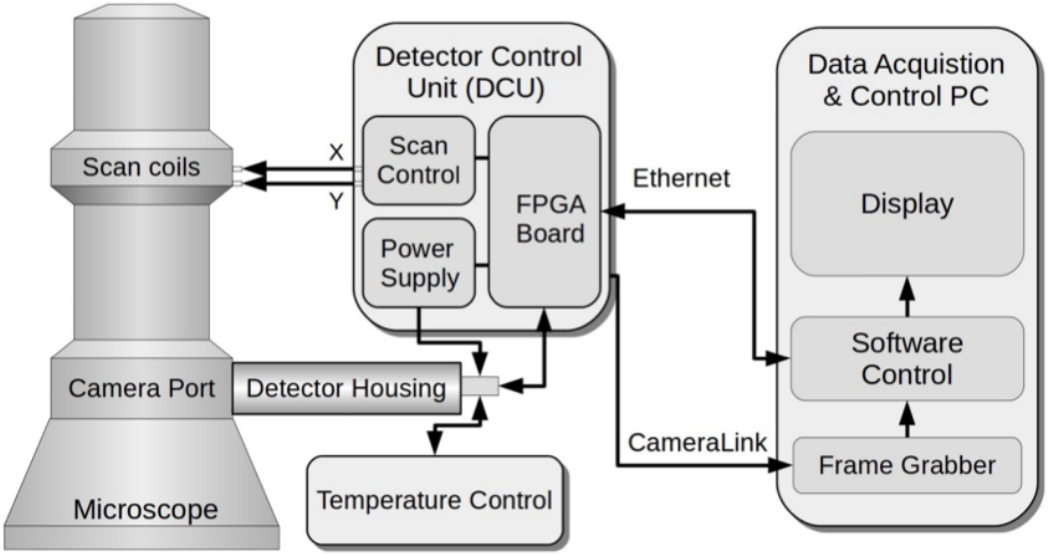

Figure 2.3. Detector Overview. The Detector Housing connects to a standard camera vacuum port on the microscope. The Detector Control Unit (DCU) provides control signals to the detector and captures the image data stream. Beam scan voltages are synchronized with image acquisition in SEM mode and are connected to the microscope's external scan control inputs. Images are transferred to the data acquisition computer via a CameraLink interface. Instructions for camera control and setup are sent to the DCU via Ethernet commands.

2.2.3 Detector Housing

The detector housing is adapted from a Fischione-3000 HAADF detector, with a custom insert containing the EMPAD camera (Figure 2.4a) replacing the HAADF camera. The Fischione housing pneumatically slides the EMPAD camera insert in and out of the microscope column in order to move the detector in and out of the main

electron beam. The insert includes the detector module (Figure 2.4c), the vacuum feed-through board (Figure 2.4b), and cooling mechanisms for the detector. The detector module consists of a small printed circuit board which is mounted onto an aluminum heat sink and wire-bonded to the detector ASIC. A long printed circuit board epoxied into a vacuum flange provides the vacuum feedthrough, along with 8 channels of analog to digital conversion and signal buffering to the FPGA.

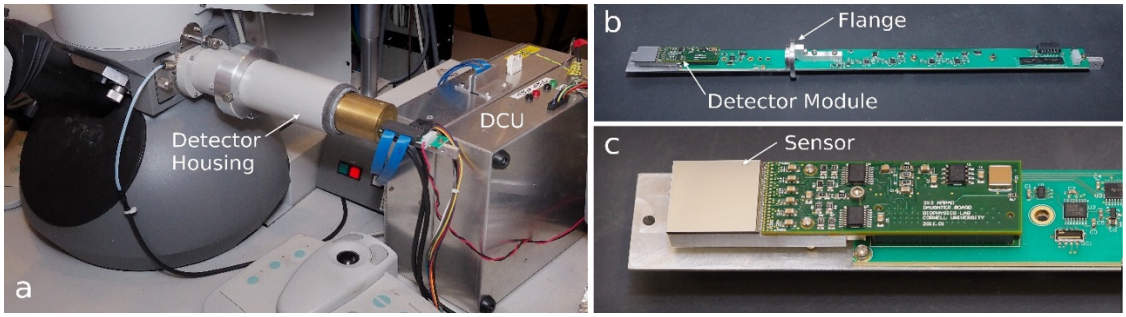

Figure 2.4. Detector Housing and camera insert. a) Fischione housing with EMPAD detector mounted on microscope. Also shown is the Detector Control Unit (DCU) b) EMPAD camera insert. The EMPAD detector module is at far left and is plugged into a long printed circuit board which is epoxied into a vacuum flange. Items to the left of the flange are in vacuum. Connectors on the right provide power and control signals. Not shown are the copper aperture covering the detector module and the additional radiation shielding near the connectors. c) Detail of detector module. The EMPAD sensor is the small gray square on the left, which is wire-bonded to the dark printed circuit board. These pieces are attached to an aluminum heat-sink. A thermoelectric module (not shown) is sandwiched between this heat-sink and the larger aluminum piece underneath, which is machined as one part with the vacuum flange as acts as a water

cooled manifold for the thermoelectric module.

The detector module is actively cooled by a thermoelectric module to -16.0 +/- 0.05 C to reduce dark current noise and provide thermal stability (the exact temperature is not as important as the temperature stability). The thermoelectric is mounted between the detector module and the vacuum flange, which doubles as a water manifold to provide a heat sink for the thermoelectric module. A copper aperture shields everything but the detector sensor from direct illumination by electrons. Radiation shielding was integrated into the insert to mesh with the shielding present in the Fischione housing to eliminate stray radiation escaping from the microscope.

2.2.4 Detector Control Unit

The detector control unit is connected to the detector housing via a 0.5 m long high-signal density cable to provide control signals to, and data reception from the detector housing. Detector housing power is also provided from this unit, as are signals sent to the external scan coil control of the microscope. An FPGA board (Xilinx Virtex-6 ML605) controls data acquisition and the communication between different components of the detector system. It drives the detector control signals and captures data from 8 banks of pixels. The captured data is processed and sent to the DAQ computer through a dedicated CameraLink interface. It receives user commands from the DAQ computer using Ethernet communication. Integration timing is set using a 36-bit programmable counter in the FPGA. The scan control consists of two 16-bit digital-to-analog

converters (Texas Instruments DAC8718) which are programmed by the FPGA via high-speed serial peripheral interface (SPI) in synchrony with the image acquisition. The number of scan points and the scan range are programmable. The scan control output is connected to the external scan control input of the microscope. The DCU includes a custom power supply board that provides regulation and monitoring for different power lines going to the detector chip. The regulation and monitoring is controlled by the FPGA via a dedicated serial SPI interface.

2.2.5 Data Acquisition and Control Computer

The data acquisition computer is a Linux workstation running Ubuntu 12.04 with 64 GB of RAM for image buffering. Images are acquired using a Matrox Radient eCL CameraLink board which can collect frames with a bandwidth of up to 5 Gb/s. Control is provided with a custom software package which meshes the needed FPGA command sequences with the frame grabbing. The software provides a live display of the diffraction frames as well as the scan images acquired as the electron beam is progressively scanned over the sample. The intensity at each scan image point is computed from user-defined regions of interest (ROIs). Multiple live ROIs can be defined and can easily be set for bright-field, dark-field, or differential phase contrast imaging. A mode which provides continuous imaging at a fixed scan position can be used for both beam and sample alignment. A mode which uses continuous electron beam scanning with a reduced number of scan points provides a refresh rate which is fast enough to allow for microscope focusing and alignment. Before each data session, a

dark reference image is determined by averaging at least 100 images taken with no illumination. This reference image is subtracted from each data image coming from the detector and is stable over the course of at least one day. Background subtracted diffraction images from a scan are stored in a single file in a raw block format of 32 bit floating point numbers. A 256 × 256 point scan then results in a file 4 GB in size, and 512 × 512 is 17 GB.

2.2.6 Detector Characterization

To characterize the detector response, a number of imaging tests were performed at various electron energies. The results are summarized in Table 2.1.

Table 1. Detector Parameters.

Sensor format	128 × 128 pixels
Sensor thickness	500 μm silicon
Pixel size	150 × 150 μm^2
Dynamic range	30 bits
Full well	3.7×10^6 100 keV electrons/pixel/frame
Signal/electron (100 keV)	197 ADU
Read noise	2.8 ADU 0.014 electrons (@100 keV equivalent)
Dark current at −16°C	2.7 electrons/s (@100 keV equivalent)
Dark noise for 1 s exposure	0.01 electrons (@100 keV equivalent)
Read time	0.86 ms/image

ADU, analog-to-digital units.

The signal per incident microscope electron was characterized at various electron energies by broadly illuminating the detector at low fluence (<<1

electron/pixel/frame). Each electron of a given energy produces a well-defined number of electron-hole pairs in the sensor (one electron-hole pair for each 3.6 eV of incident microscope electron energy).

A histogram of the pixel response over a large number of frames yields an energy response histogram to these monochromatic electrons. Figure 2.5 shows the pixel response to electrons with 80, 120, 160, and 200 keV energy over 10,000 frames with a mean illumination intensity level of ~ 0.06 electrons/pixel/frame. The curve at each energy has a peak at 0 ADU, corresponding to pixels with no electrons. For the 80 keV curve, discrete peaks at 151, 303, and 454 ADU, correspond to 1, 2, and 3 electrons contained in a single pixel. The curves at higher electron energy have discrete electron peaks at proportionately higher ADU values. These curves together show a response of 1.97 ADU/keV of microscope electron energy. A read noise of 2.8 ADU rms can be computed from the width of the 0 electron peak. This corresponds to a noise of 1.4 keV equivalent microscope electron energy, or 0.014 of a single 100 keV electron. Note that the sensor is constructed with a p+ implant region at the input face that is insensitive to the collection of ionizing radiation. As the incoming electrons traverse this region, a fraction of the energy from each electron will be lost. Thus we observe, for instance, that the 2 electron peak position for 80 keV electrons does not exactly match the position of the 1 electron peak from the 160 keV curve. Fitting to the electron peak positions from the series of energies allows us to estimate a dead region of ~ 1 μm thickness, consistent with parameters obtained from the sensor manufacturer.

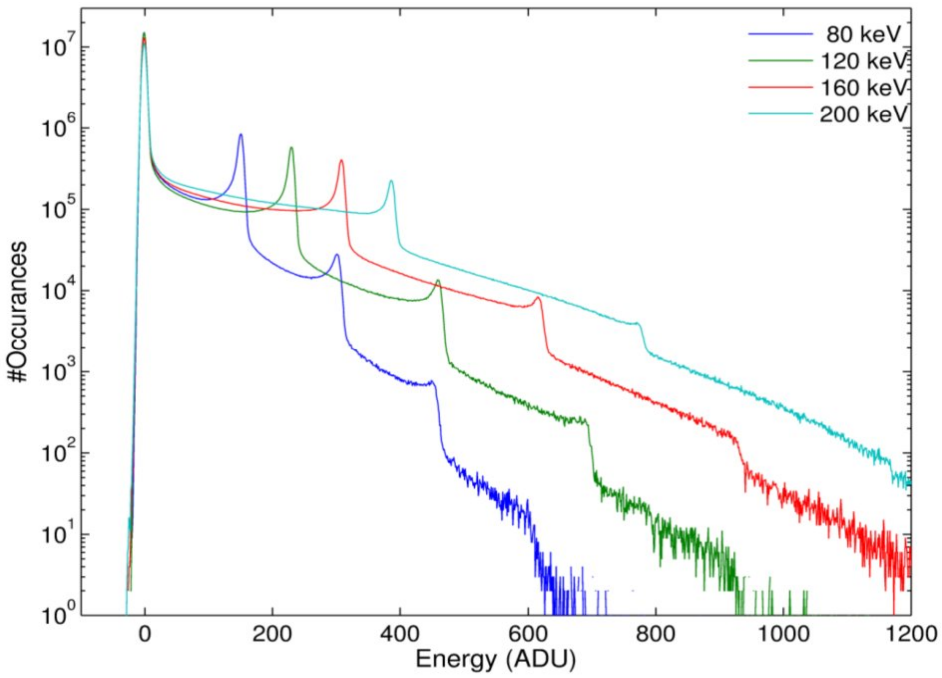

Figure 2.5. 2. from 10,000 frames for very low, uniform illumination of the detector with electrons of 80, 120, 160, and 200 keV energy. The peak at 0 ADU corresponds to pixels with no electrons. For the 80 keV curve, the peaks at 151, 303, and 454 ADU correspond to peaks from 1, 2 and 3 microscope electrons per pixel. Intensity between the peaks arises to the signal from some electrons being shared between adjacent pixels. Discrete electron peaks for higher energy electrons occur at proportionately higher ADU values.

The sensor generates a dark current in the absence of illumination at a rate of $7x10^4$ electron-hole pairs/s/pixel at -16 C. This is an equivalent signal to 2.7 primary electrons (at 100 keV) incident on a pixel per second. The noise associated with this dark charge is only 268 electron-hole pairs, equivalent to 0.01 incident electrons (100 keV equivalent) for exposures of up to one second. The dark current is insignificant at typical frame rates of 0.86ms/image.

For 100 keV electrons, the analog well of the integration stage is chosen to accumulate up to 14.2 electrons before the charge removal circuitry is activated. Note that it is not required that an integer number of primary microscope electrons be contained in the analog well. Combining the analog well depth with the 18 bit counter yields a full well of 3.7×10^6 100 keV electrons/pixel/frame. Note the charge removal circuitry is limited to a rate of ~ 2MHz, which gives a maximum rate of 2.8×10^7 100 keV electrons/pixel/s. Thus for 1 ms images, there is a limit of 2.8×10^4 100 keV electrons/pixel/frame. This selected rate corresponds to a beam current of 4.5 pA/pixel. This is not a fundamental limit, but a design choice, and in future designs could be increased by changing the accumulation threshold or counter speed.

The pixel response histograms also show nonzero intensity between the discrete electron peaks due to sharing of charge between pixels. One expects some charge sharing, especially for electrons that strike the sensor near a pixel border. By comparing the area of the first electron peak to that of the charge sharing tail, we can obtain a measure of the charge sharing for randomly placed electron events. Table 2.2 shows the fraction of incident electrons whose energy is recorded in a single pixel.

Table 2. Charge Spread in Sensor.

Energy (keV)	Fraction of Single Pixel Electrons	Radius (μm) to Collect 50% of Charge	Radius (μm) to Collect 95% of Charge
80	0.54	14	32
120	0.40	30	67
160	0.26	49	112
200	0.13	74	167

Note that for higher energies, a higher fraction of the incident electrons have charge shared among pixels, indicating a larger charge spread for these electrons. Monte Carlo simulations were used to estimate the radial distribution of energy deposition in silicon (Win X-ray) [33]. Table 2.2 shows the radii at which 50 % and 95 % of the energy from incident electrons is collected. Note that for 200 keV, the radius for complete charge collection is larger than could be contained within a single pixel. If each electron lost energy according to this mean response profile, then no single electron peak would be seen for 200 keV. However, each electron undergoes a random walk through the sensor, losing energy along a unique track, some of which are entirely contained within a pixel. Figure 2.6 shows 200 such tracks for 80 through 200 keV incident electrons obtained from Win X-ray Monte Carlo simulations.

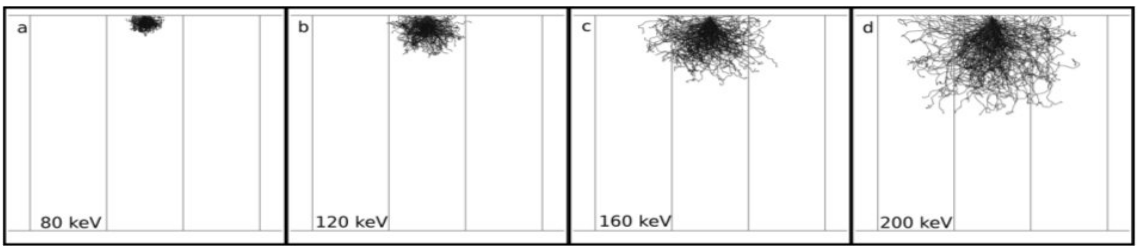

Figure 2.6. Monte Carlo simulations of electron tracks in silicon for a) 80, b) 120, c)

160, and d) 200 keV electrons. Each panel shows 200 individual electron tracks which impinge on the sensor at the top of each panel (3 pixel area covered in each panel). Pixel dimensions of 500 μm thickness (top to bottom) and 150 μm laterally are indicated by gray lines.

While single electron tracks can be sharper than the mean spatial response, the spatial response at higher levels of illumination should match the mean response of the sensor. To measure the base response of the system, the knife edge response was measured under illumination by 8 keV x-rays. By using 8 keV x-rays, the energy deposition in the sensor is highly localized to a small volume rather than along a track as with high-energy electrons. Thus the edge response measures the diffusive spread of the charge as it traverses the sensor and is collected at the pixelated nodes. At 150 V sensor bias, this gives a value of 10 - 15 μm FWHM for the diffusive charge spread cloud in the sensor. Under illumination with electrons, this diffusive spread will be convoluted by the charge spread due to the random walk of the primary electron as it loses energy in the sensor. The 50% charge collection radius in Table 2.2 shows that the width of this convolution should be dominated by the electron track spreading for all but the lowest energies. Measurements of the detector's point spread function and modulation transfer function are given below in the results section (Quantification of Detector Performance). If one were to construct a PAD with smaller pixels, some gain in spatial resolution can be expected for lower electron energies. Little would be gained by using smaller pixels for energies 200 keV or above, unless the detector was thinned as well, which would then introduce straggle into the energy distribution.

2.2.7 Quantification of Detector Performance

To investigate the spatial response of the detector, we measured the line spread function (LSF) and the modulation transfer function (MTF) from an edge resolution test. We imaged the edge of a large (800 micron) selected area aperture projected onto the detector at low magnification in TEM mode. We summed 100 successive images of the edge (0.1 s total acquisition time), and calculated the LSF from the derivative of the image. The results are shown in Figure 2.7 a,b for 80 and 200 keV respectively. We calculated the MTFs from the Fourier transform of the LSF and these are shown in Figure 2.7c. The effect of the increased LSF tails at 200 keV vs 80 keV is apparent, and is expected, given the spread seen in the simulations of Figure 2.6.

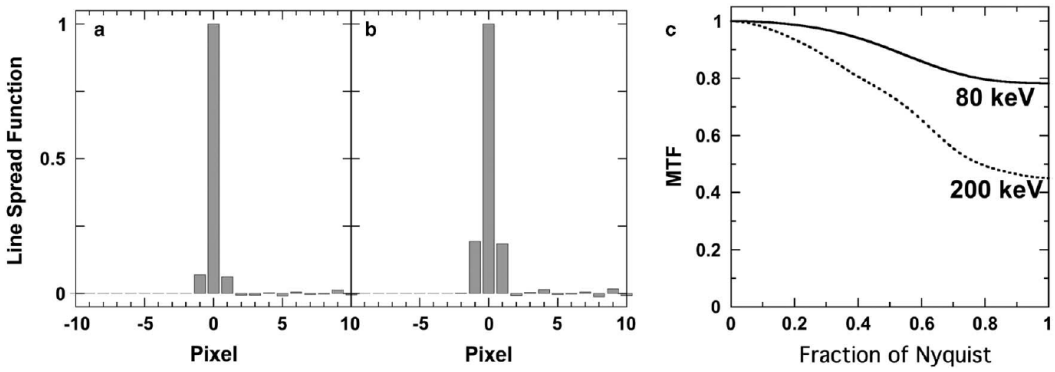

Figure 2.7: Measured detector response from the edge of an aperture imaged onto the detector. Line spread functions (a) 80 and (b) 200 keV were calculated from the derivative of 100 images of the edge. The modulation transfer function (MTF) (c) obtained from the Fourier transforms of the line spread functions, with spatial frequency

plotted as a fraction of the Nyquist frequency.

To measure the detective quantum efficiency (DQE) we use the noise binning method [34] and extrapolate the measured noise as a function of bin size to account for the effect of the point spread function. We work from a series of 100 images and use the difference between successive images to follow the same approach as has been used to benchmark previous MAPS detectors [34]. The DQE is a function of dose rate – at low rates readout and dark noise will dominate, and at high rates gain variations between pixels become significant. For a count rate of roughly 0.2 electrons/pixel/frame, the extrapolated DQE at 80 kV is 0.88, and at 200 keV is 0.93. For a mid range count rate of roughly 700 electrons/pixel/frame, the extrapolated DQE at 80 kV is 0.93, and at 200 keV is 0.94. The difference is probably within the extrapolation error.

The DQE for systems that operate in counting mode, are typically reported at doses of well below 1 electron/pixel as the DQE of counting mode systems degrades as the count rate increases due to coincidence losses (Appendix C of [2]) suggests roughly a 10% loss in DQE at 10 electrons/pixel/frame). The EMPAD, which relies on charge integration instead, retains a high DQE over many orders of magnitude more than that.

While a frequency dependent DQE is often used to characterize imaging detectors that operate with relatively flat fields such as imaging low-contrast objects, it does less well at capturing the key performance properties of a detector intended for

diffraction work. Diffraction patterns display very large dynamic ranges, and spill over from tails of high intensity diffraction peaks can swamp small features nearby. A similar challenge is present for detectors used for electron energy loss spectroscopy when measuring features near the zero loss peak. With these larger intensity variations, measures such as the full width at $1/100^{th}$ maximum (FWCM) and full width at $1/1000^{th}$ maximum (FWKM) are a better reflection of diffraction performance. For the EMPAD, the FWCM is 3 pixels at both 80 and 200 keV, and the FWKM is 3 pixels at 80 keV and 5 pixels at 200 keV. A comparison measurement of the EMPAD's FWKM with other reported direct electron detectors to date does not appear possible as the signal required to measure a $1/1000^{th}$ of the maximum exceeds their designed dynamic ranges per frame.

2.3 Results and Discussion

To investigate the imaging performance of the detector, we mounted it in the 35 mm port of a FEI Tecnai F20 200 keV Schottky field emission STEM. The microscope is uncorrected, and can form a sub-0.2nm spot size with 10 pA of beam current at a 10 mrad convergence semi-angle. The first sample selected was a film of $BiFeO_3$. This is a ferroelectric material grown epitaxially on a $SrRuO_3$ electrode lattice matched to a $DyScO_3$ substrate.

2.3.1 Imaging examples

As an illustration of the detectors sensitivity and dynamic range, Figure 2.8 shows the diffraction pattern recorded along the [010] pseudocubic zone axis in $BiFeO_3$. Figure 2.8a shows a pattern recorded in 1 ms and displayed on a log scale, calibrated in the number of primary electrons. Even at 1 ms, the recorded diffraction pattern shows both the central beam and Kikuchi band details out to the HOLZ line, where the high SNR ratio for single electron detection is essential for resolving the HOLZ line itself. Fig 2.8b shows the accumulation of data over 100 frames. The data now spans over 4 orders of magnitude and the details of the unsaturated central beams as well as the Kikuchi bands and HOLZ lines are much clearer.

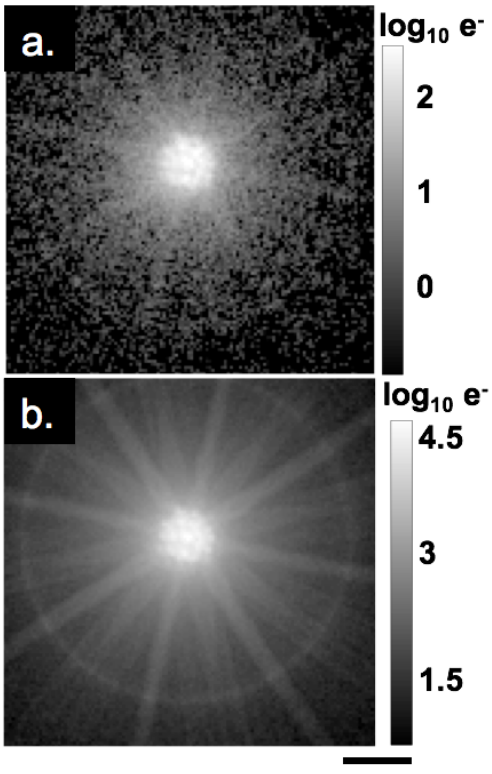

Fig 2.8: a.) CBED pattern of $BiFeO_3$ recorded in a) 1 ms and b) 100ms with 10 pA of

beam current at a single scan position. All CBED images shows the number of electrons detected on the EMPAD detector, showing quantitative measurements of electron counting. Black bar on the lowermost far right represents 20 mrad for the diffraction patterns above.

Throughout our work, we have not yet been able to saturate the detector, even with the unscattered beam placed directly on the detector. This allows us to record full diffraction patterns without the need for a beam stop. Consequently, we can quantify any extracted signal as either a fraction of the incident beam, or as an absolute number of electrons. The former is useful for quantitative atom counting and thickness determination [35], and avoids the challenges of having to correct for the integrated, non-uniform response of an ADF scintillator.

With these issues in mind, Figure 8 shows the bright field (BF), High Angle Annular Dark Field (HAADF), Differential Phase Contrast (DPC), and Center of Mass (COM) signals all extracted from the same EMPAD-STEM data set. All signals are therefore aligned to each other, and their relative (and absolute) intensities can be compared directly. The HAADF signal from 50 to 250 mrad (Fig 2.9b) is plotted as a fraction of the incident beam (I/I_0), which can be compared to multislice simulations to extract the local variations in thickness. Even signals whose overlapping nature would make them incompatible if recorded on distinct detectors (e.g., BF (a) or annular bright field versus DPC) can be simultaneously determined. The bright field image from 0 to

5mrad is shown in Fig 2.9a. The DPC and COM signals in Fig 2.9c,d require integration over the entire diffraction pattern to meet the strong quantum measurement condition [36], and ensure lateral incoherence [37 – 39].

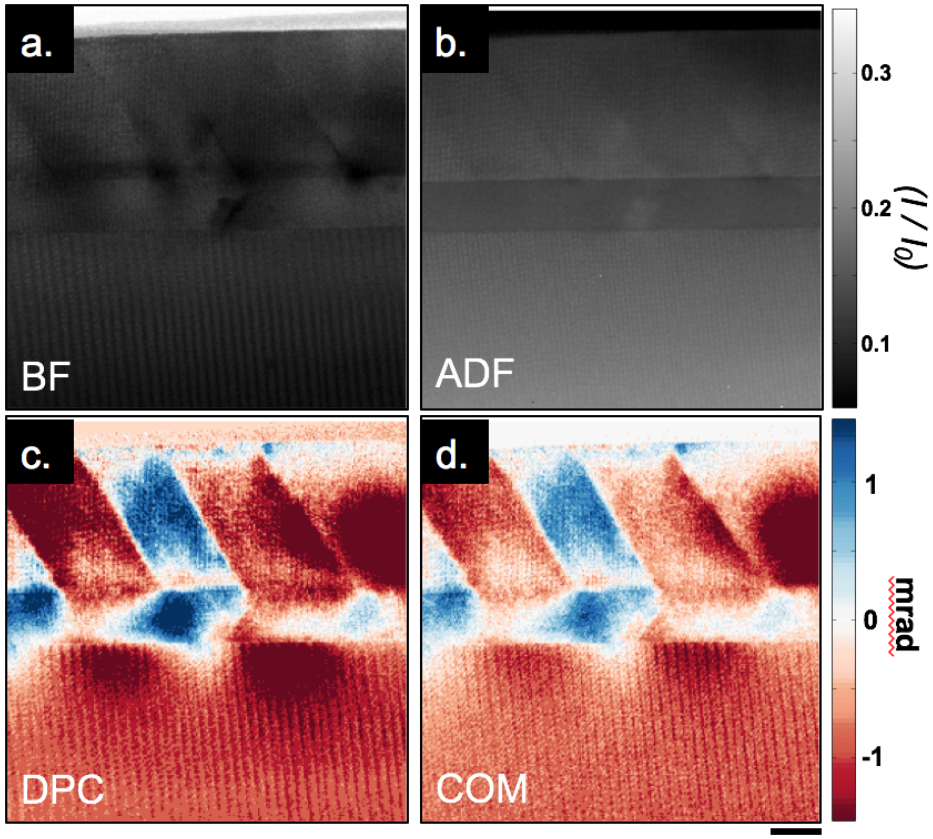

Fig 2.9. Different imaging modes extracted from a EMPAD-STEM image of 137 nm thick $BiFeO_3$film grown on a 54 nm $SrRuO_3$ electrode on a $DyScO_3$ substrate. 65 second acquisition time. a.) Bright field signal from 0 to 5 mrad, b) annular dark field signal from 50-250 mrad, c) differential phase contrast in the x-direction and d) center of mass shift in the x-direction. COM deflections are shown in milliradians. The black scale bar under d), which is common to all the images is 50 nm. The (I/I_0) colorbar is common to the BF and HAADF images of panels a and b. The striations are aliasing artifacts

from undersampling of the atomic lattice with an atomic-sized probe.

For very thin specimens, the net deflection of the electron beam can be related to the electric field in the sample [24, 36, 39-42]. For thicker objects or imaging at atomic resolution, considerably more caution is required for the interpretation of these deflection images [36, 43]. From a theoretical standpoint, calculating the center of mass of the diffraction pattern, $I(\vec{p})$, gives

$$\langle \vec{p} \rangle = \int \vec{p}\, I(\vec{p})\, d\vec{p}\,, \tag{2.1}$$

the expectation value of the net momentum transfer, $\langle \vec{p} \rangle$, integrated through the depth of the film [36, 39, 41]. With previous detectors, direct measurement and integration of the diffraction pattern has not been possible, making Figure 2.9d probably the first experimental realization of direct center of mass imaging. Instead, the approach has been to employ a split or quadrant detector [40, 42, 44] to measure the deflection of the beam by shifts of intensity between the split segments. The resulting differential phase contrast (DPC) image provides a qualitative approximation to the COM image – the DPC image of figure 2.9c is visually similar, albeit slightly noisier, to the COM image of figure 2.9d. More careful analysis shows that the DPC phase contrast transfer function is anisotropic, with about 20-30% reduction in transfer at midrange frequencies, and the amplitude contrast transfer function has a cutoff along k_x at about half that of the COM detector [39].

With the EMPAD, both the DPC and COM signals are easy to extract. The convention of normalizing the DPC signal as the difference/sum of the split segments to minimize diffraction contrast does introduce nonlinearities and the potential for numerical instabilities as is evident at the top of Figure 2.9c. In terms of noise, the COM signal appears to perform more robustly in our experience (contrast with Figure 2.9d). As a matter of convenience, the COM signal has one further advantage, that is once the diffraction pattern (such as Figure 2.8) is calibrated, then it follows from equation (2.1) that so the COM image is also calibrated. In general, once we know the camera length, the same calibration can be used to a few percent accuracy for the COM image. Quantification of the fractional DPC shift is more problematic, and depends on knowing the shape of the diffraction, with small changes in shape and centering leading to artifacts [45-46].

Atomic-resolution imaging is also possible with the EMPAD detector. Figure 2.10 shows the HAADF and *x* and *y* COM images of a domain boundary in the $BiFeO_3$ film. While there is a clear shift of the beam between the two domains, it would be incorrect to interpret this as an electric field, consistent with recent cautions [39, 43]. In both Figures 2.9 and 2.10, the domains in the $BiFeO_3$ film are oriented along the [111] zone, while the film is viewed down the [001] pseudocubic zone. The distortion of the unit cell in the ferroelectric state forces a tilt of the domains to retain coherent boundaries, with a resulting tilt of the diffraction pattern on the order of mrad. By examining EMPAD-STEM images with a smaller convergence angle, the tilting of the Ewald sphere across these domains is very obvious. The contrast in the COM images

is dominated by a mixture of tilt and polarity difference. In these images, tilt plays a larger role than polarity, but that will depend on the sample geometry. The large integration angles appear to suppress any Fresnel contrast at the boundary in general, although these particular images are recorded in focus. We also note contrast differences with thickness as diffracted beams oscillate vary in intensity with thickness.

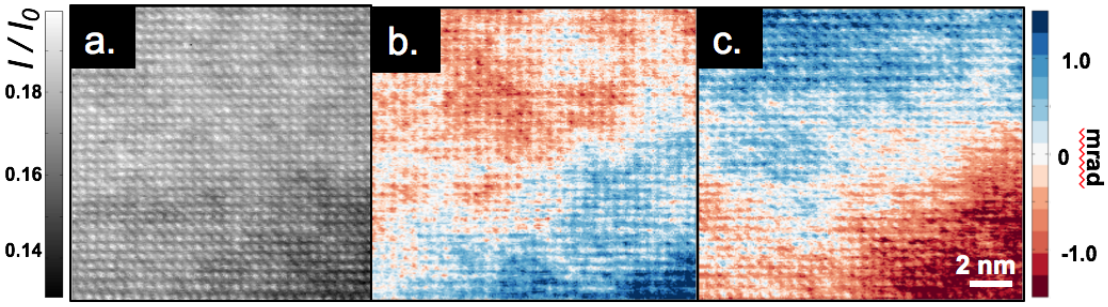

Fig 2.10: a) Atomic resolution HAADF image of $BiFeO_3$ taken using the MMPAD at a domain boundary. b) center of mass image taken in x and c) y showing structure changes at the atomic domain boundaries where deflections are shown in milliradians. The 2 nm scale bar in c also corresponds to a and b. All images are extracted from the same EMPAD-STEM data set, with 65 second acquisition time.

A final imaging example of true field measurement is shown in Figure 2.11. Here a 50 nm-thick Co film is imaged in low-magnification STEM (LM-STEM) mode with the objective lens turned off for field-free imaging. In this configuration the beam is highly parallel, which makes COM detection highly sensitive to small shifts in magnetic field. Additionally, the beam is larger than the grain size in the cobalt film, thus averaging over the grain contrast that is apparent in regular STEM mode with a

smaller spot size. The deflection of the beam appears as a uniform shift of a few microradians. With the film thickness known, the deflection is converted to magnetic field – e.g., equation 2.1 of [22]. The result is a quantitative image of both the x and y components of the magnetic field ripples in the cobalt film. Again, the center of mass analysis gives a simple and direct calibrated image.

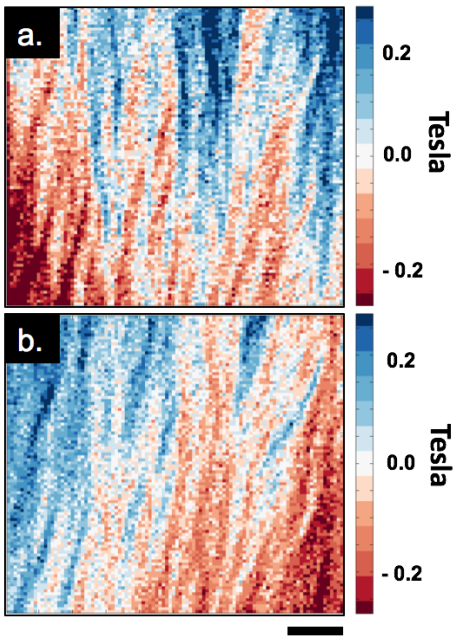

Fig 2.11: Center of Mass measurements of magnetic deflections (converted from mrad to Tesla) for 50 nm Co specimen on silicon nitride in a) x- and b) y-directions. Black scale bar represents 4 microns. Recorded in LM-STEM mode with the objective lens turned off for field free-imaging.

2.4 Conclusion

This high dynamic-range EMPAD provides convenience in defining custom

regions of interest which can reproduce any of the conventional STEM imaging metrics such as bright field, annular dark field, or differential phase contrast. However, the real impact of this type of detector will likely be the ability to define new modalities which will allow quantitative measures and decoupling of parameters such as tilt, electric and magnetic fields to be extracted from a data set, or since almost every electron that is transmitted through the sample is recorded, the potential for post-hoc optimally dose-efficient image reconstruction. Recording the full diffraction pattern on one detector allows the scattering to be placed on an absolute scale, with a direct measurement of the magnitude of diffraction spot deflections possible. Careful consideration of effects due to sample tilt and thickness must be given to separate those effects from underlying deflections from internal sample fields. This may require one to choose to image with beam optics to be optimized and aligned with non-standard parameters.

The range of electron energies could be extended well below the 80 keV tested here. As an x-ray imager, good signal to noise for single x-rays has been demonstrated down to 8 keV. Lower energies than this can be used since the charge integration nature does not need to resolve individual incoming quanta. The EMPAD detector has been used successfully with X-ray energies as low as 2.5 keV. The lower energy threshold is limited primarily by the aluminized bias contact and the diode p+ implant on the input side of the sensor. At higher electron energies (over 200 keV), one must consider lattice displacement damage in the sensor, and ultimately, radiation damage to the readout chip once the electron range in silicon becomes greater than 500 μm. Alternative, higher atomic number sensor materials could alleviate these concerns to some degree, as well

as improve the spatial resolution of the detector.

While performance of this converted x-ray imager has been quite good for imaging electron scattering, some improvements could improve the utility of the device for use on electron microscopes. The addition of a data latch in the pixel would allow integration during readout, which would improve the duty cycle of operation. Secondly, since the signal/noise ratio is very high for electrons in this energy range, one could implement amplifiers with higher bandwidth (and higher noise) to reduce read time and improve frame rate. At higher frame rate, an improvement to the incoming electron rate would prove beneficial. One can choose a larger integration capacitor and optimize the charge removal circuitry to improve the maximum incoming rate. Changes to the readout architecture such as implementing selective addressing of pixels or selective ganging of pixels could also improve read speed to 10 kHz or beyond.

With the present detector format, there is an inherent trade-off in choosing the camera field of view for diffraction imaging. Capturing high-angle scattering usually used for HAADF images will limit the angular resolution at which details of lower-order diffraction disks are acquired. A larger format detector can alleviate this. Besides the higher data collection bandwidth and storage needed, the maximum size of the ASIC die is limited. Larger x-ray detectors of similar design have already been constructed using multiple ASICs attached to a larger sensor.

CHAPTER 3

MAGNETIC IMAGING OF IRON GERMANIUM

Lorentz Transmission Electron Microscopy (LTEM) has been widely used to investigate the real space magnetization profiles of chiral and topological spin textures, e.g. helices and magnetic skyrmions [47]. Although LTEM provides few-nanometer spatial resolution, defocusing the electron beam, which is necessary to obtaining magnetic contrast, causes overwhelming Fresnel fringes from the grain contrast leading to misinterpretation of magnetic textures [48-49]. Lorentz Scanning Transmission Electron Microscopy (LSTEM) presents another alternative [39, 50]; here LSTEM measures the deflection of the electron beam from the electromagnetic field similar to differential phase contrast (DPC) imaging [51] to study internal structures of magnetic skyrmions. In LSTEM, a focused electron beam is deflected from the local magnetic fields and this deflection is used to reconstruct a quantitative magnetic field [41]. Although DPC and transport of intensity reconstructions from LTEM are roughly connected, the incoherent response function for DPC imaging effectively doubles its information limit, and allows all the information needed to be recorded in a single, in-focus scan [39]. However, there are multiple constraints to DPC imaging including limited dynamic ranges of the detectors, nonlinearities introduced by the signal normalization when the detector is not perfectly centered, and changing beam shape [36,52]. In addition, current STEM studies have focused on single-crystal samples that exhibit sparse grains and few defects, thus presenting a structurally uniform medium for imaging.

For technology, however, materials must be grown using scalable techniques like sputtering, which typically produce polycrystalline grains. Recently, proposals for power efficient spintronic memory devices based on chiral magnetism have been made by sputtering thin films [53 -55] where the chiral magnetism that arises is a result of the noncollinear spin texture from the Dzyaloshinskii-Moriya interaction (DMI) [56], present at interfaces and in the volume of noncentrosymmetric materials with broken inversion symmetry. Therefore, to study real magnetic devices used in modern-day scalable techniques, we focus our investigation on thin-film cubic B20 crystalline FeGe sputtered on top of silicon and explore how chiral magnetism is affected by the sub-micron scaled grains and grain boundaries|, previously observed to be modified under substrate-induced strain [57]. We do so using LSTEM aided by the EMPAD, where we capture every diffraction pattern at each scan position, selectively choosing regions of grain contrast from regions of magnetic contrast in the diffraction patterns, and probing each effect independently. Our technique is only enabled by the high-dynamic range and high-speed of the EMPAD where we expect a magnetic field sensitivity with high spatial resolution.

3.1 Background Theory

Previously, reconstruction of electromagnetic fields has been attempted using techniques such as differential phase contrast (DPC) or center of mass (COM) imaging. Here, a strong phase object approximation (SPOA) is used to represent the transmitted

electron wave function as an approximation to the probability current flow, $< \boldsymbol{p} >$, where $< \boldsymbol{p} >$ is then directly related to electromagnetic fields [Wardell, Chapman 1974] [1].

In SPOA**,** the incident wave function is written as $\psi_0(r) = A(r)e^{i\zeta(r)}$ where A(r) is the amplitude of the wave function and ζ is the initial phase of the wave function. The specimen transmittance function can be written as $t(r) = B(r)e^{-i\sigma V(r)}$, where B(r) is the amplitude term, σ is the interaction parameter representing the coupling strength and V is the specimen potential. Using the SPOA, we assume that the transmission amplitude is constant such that B(r) =1. Our scattered wave function becomes

$$\psi(r) = \psi_0(r)\, t(r) \approx \psi_0(r)\, e^{-i\sigma V(r)} \tag{1}$$

By taking the Fourier transform of the electron wave function, the first moment can be directly calculated from the intensity of the scattered wave function, the CBED pattern, as:

$$< \boldsymbol{p} > = \int \psi(p)^* \hat{p} \psi(p) d\vec{p} = \int \hat{p} |\psi(p)|^2 dp = \int \hat{p} I(p) dp \tag{2}$$

where ψ is the electron wave function, $I(p)$ is the intensity of the CBED pattern, and p is the momentum operator [39].

If we write equation (2) back into real space, we observed that [39-40]

$$< \boldsymbol{p}(\boldsymbol{r}) > = \sigma|\psi|^2 \otimes \nabla V(r) \tag{3}$$

From which, we observed that DPC imaging is a linear imaging technique where the signal is approximated as the first moment, center of mass of the CBED pattern, or as the averaged value of the momentum operator $< \boldsymbol{p} >$. By representing the amplitude of the wave function as such, we observed that its shape is constraint and not allowed to change.

By rewriting $< \boldsymbol{p} >$in real space, we observe that $< \boldsymbol{p} >$is directly related to the probability current flow $\boldsymbol{< j >}$. Thus, in general, and going beyond the SPOA, $< \boldsymbol{p} >$is also an evolving electron wave function[15, 16] where the electron beam is changing as it propagates through the specimen.

$$\langle \vec{p} \rangle = \frac{\hbar}{2i} \int \Psi^*\left(\vec{r}, \vec{r}_p\right) \vec{\nabla} \Psi\left(\vec{r}, \vec{r}_p\right) - \Psi\left(\vec{r}, \vec{r}_p\right) \vec{\nabla} \Psi^*\left(\vec{r}, \vec{r}_p\right) \mathrm{d}\vec{\mathrm{r}} = 2m\langle \vec{j} \rangle \tag{4}$$

Moreover, a relation to Ehrenfest's theorem and Lorentz force law are used for $< \boldsymbol{p} >$ [4, 17], and are typically used to reconstruct the electromagnetic field,

$$\frac{d\langle \vec{p} \rangle}{dt} = \left\langle \left[\hat{H}, \hat{p}\right] \right\rangle = \left\langle q\left(\vec{E} + \vec{v} \times \vec{B}\right) \right\rangle \tag{5}$$

although every signal from $< \boldsymbol{p} >$ results in a signal for the atomic, electric and magnetic fields. Here, H is the Hamiltonian, q is the charge of the electron, E is the electric field, v is the velocity at which the electron is traveling and B the magnetic field.

For Lorentz Microscopy, we consider a parallel electron beam source that is incident perpendicular to the plane of the specimen, along the z-axis. Here, we assumed that stray field effects are ignored and the deflection is only due to the in-plane magnetic field, our equation for deflection then is given as:

$$\beta(x) = e\lambda B_0 t/h, \tag{6}$$

where B_0 is the local magnetic field, e is the electron charge, λ is the wavelength of the electron beam, t is the sample thickness and h is Planck's constant [22]. This shift of the electron beam can be measured by tracking the center of mass (COM) of the diffraction pattern for each position as we scan the electron beam and this deflection can be related back to the magnetic field. For a beam energy of 200 keV, sample thickness of 50 nanometer and a saturation B field of 0.5 T, the deflection angle is 3.0 * 10^{-5} radians. Here the typical deflection angle from Bragg diffraction is 0.01 radians, meaning that the deflection from the magnetic field is 1/1000 times that of crystallographic diffraction.

3.2 Calculating the Standard Deviation and Relative Error for the Center of Mass (COM)

How well we can track this deflection essentially tells us the resolution limit of magnetic field for our technique. Therefore**,** to quantify how accurate our measurement of the

magnetic field, we must first calculate the standard deviation and relative error from our COM measurement. We do so by analyzing how the standard deviation and relative error in our center of mass (COM) measurement depends on the number of pixels, the electron dose, and readout speed. Our model assumes a one-dimensional detector with that is incident by an electron beam in the form of a Gaussian distribution. We add Poisson noise to our ideal Gaussian probe such that our simulation results may reflect the distribution of a real electron source.

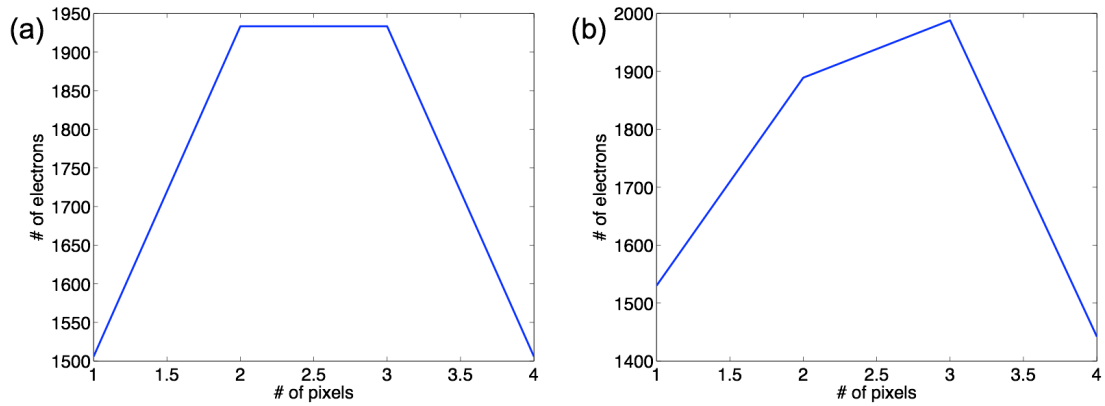

Fig 3.1: Simulated Electron Probe for a One-Dimensional Pixel Detector. (a) Ideal Gaussian and (b) non-ideal Gaussian with Poisson noise of the Electron probe.

To obtain the standard deviation from the average, we generate 1000 samples of an ideal Gaussian with random Poisson noise to imitate the shape of the electron beam. Here we calculate the COM for N = 1000 different types of electron sources with varying Poisson noise:

$$center\ of\ mass = \bar{\mu} = \sum_{i=0}^{N-1} \frac{n_i}{n_{tot}} w_i$$

(5)

where n_i is the number of electrons in each pixel, n_{tot} is the total number of electrons for all pixels, and w_i is the number of pixels in 1 dimensions. We then calculate the standard deviation $\sigma_{center\ of\ mass}$

$$\sigma_{center\ of\ mass} = \sqrt{\frac{1}{\sqrt{N-1}}\sum_{i=0}^{N-1}((\mu_i - \bar{\mu}))^2}$$

(6)

where N is the number of samples, μ_i is the COM for each sample and $\bar{\mu}$ is the mean of the all COM values μ_i from our N number of samples.

From our equation, we want to vary the number of electrons, n_{tot}, and the number of pixels, w_i, on our detector and observe how $\sigma_{center\ of\ mass}$ changes. As we increase the number of pixels, we must normalize the standard deviation, the explanation is a as follows: as the number of pixels increase on our detector, the area on the detector that is covered by the beam has an increased number of pixels – meaning that the actual size of our pixels decreases relative to the size of the electron beam. We define the relative error as:

$$\sigma_{normalized} = \frac{\sigma_{center\ of\ mass}}{w_i} \quad (7).$$

Here, the signal to noise from our analysis can be written as SNR = $1/\sigma_{normalized}$. We proceed to ploting the SNR and its dependence on the number of electrons in our electron probe and the number of pixels on our detector. From our observations, SNR

is much more dependent on the number of electrons than it is on the number of pixels on our detector.

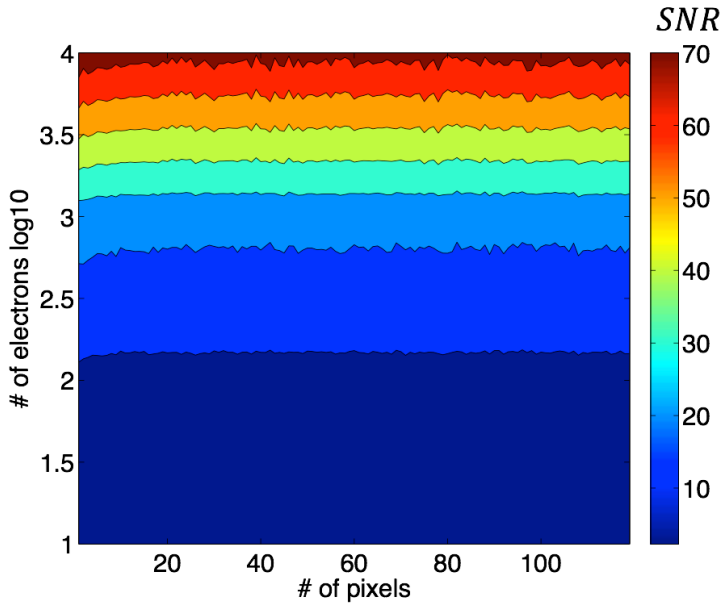

Fig 3.2: SNR dependence on the number of electrons and pixels on the detector.

When then we reduce the number of pixels and electron dose and observed that the SNR is still more highly dependent on the number of electrons than the number of pixels on our detector. Even if we keep increasing the number of pixels on our detector, our SNR remains below 5 if the number of electrons is less than 100.

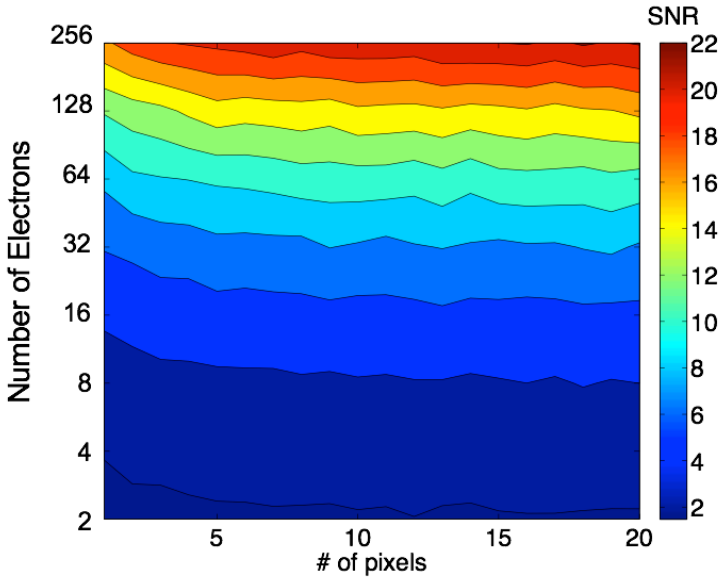

Fig 3.3: Low number of electrons and pixels on our detector. We realized that no matter how many pixels is added to our detector, if the number of electrons remain under 100, the SNR will remain under 5.

3.3 Magnetic Imaging Analysis

The goal of our simulation above is to relate our simulated error to the smallest possible detectable deflection of the electron beam from a magnetic field. We assume that our electron beam has a 200 μrad semi-convergence angle from which we observed how the error in deflection changes as we add more pixels to our detector, whilst keeping the beam the same size and therefore, as more pixels are added, the overall size of each pixel is reduced.

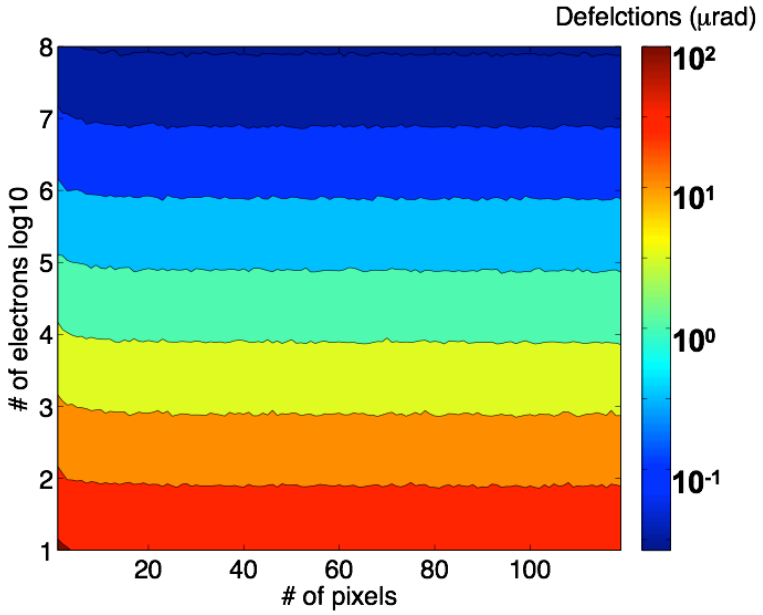

Figure 3.4: Relative error for measuring the deflection of the electron beam with respect to the number of electrons and the number of pixels on our detector.

To convert our relative error for our COM into a magnetic or electric field, we use the SPOA and Ehrenfest's Theorem shown in section 3.2 to relate the COM measurements and the magnetic field. If we assume that our beam energy is 200 keV, our beam diameter is 400 urads, and the thickness of our sample for Fe is 100 nm, we can modify our $\sigma_{normalized}$ into units of magnetic field (Figure 5).

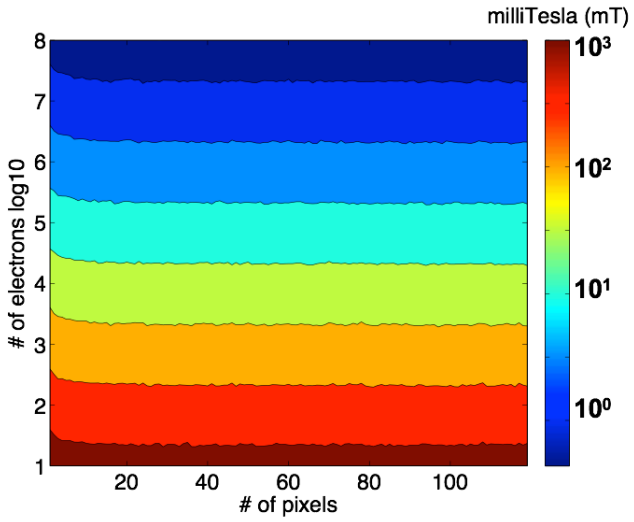

Figure 3.5: Error in resolution of magnetic fields.

However, even with the capabilities of detecting sensitive magnetic fields, we must also make sure that our signal is not dominated by crystallographic scattering effects. For electron microscopy, the magnetic deflections are on the order of ~ 40 microradians which is 1/1000 times that from crystallographic diffraction [22]. The EMPAD presents a solution because it exhibits a SNR of 140:1 for a single electron, high dynamic range - allowing detection of 1 to $>10^6$ electrons per pixel per image at 0.8 millisecond per frame, and 128 by 128 pixel architecture. With the EMPAD, we have the sensitivity for sub miliTesla imaging in addition to identification of effects arising from sample thickness, tilt, and grain contrast without saturating the detector.

3.4 Magnetic Imaging with the EMPAD

To establish the experimental capability of the EMPAD for magnetic imaging,

we first imaged bulk single-crystal FeGe in a structurally uniform environment using LSTEM. We prepared the sample using a focused ion beam and subsequently imaged at 300 keV with a 230 microradian semi-convergence angle on a FEI-Titan. It was cooled to 240 K using a Gatan cryo holder and imaged under a 135 mT magnetic field. During scanning, we record the full convergent beam electron diffraction (CBED) pattern, containing all crystallographic information, for each pixel with high-dynamic range, and high speed using the EMPAD [4] (Figure 3.6a). From the CBED pattern, we extract the center of mass (COM) to reconstruct the magnetic field. Here, we obtain the magnitude (Figure 3.6b) and from which, we observed an edge resolution (Figure 3.6 c-d) 8 nanometers for the skyrmion lattice in single-crystal FeGe. Our results for the skyrmions lattice is in agreement with prior measurements using LTEM [48] and DPC [58] where skyrmions have been observed showing similar shapes and magnitude.

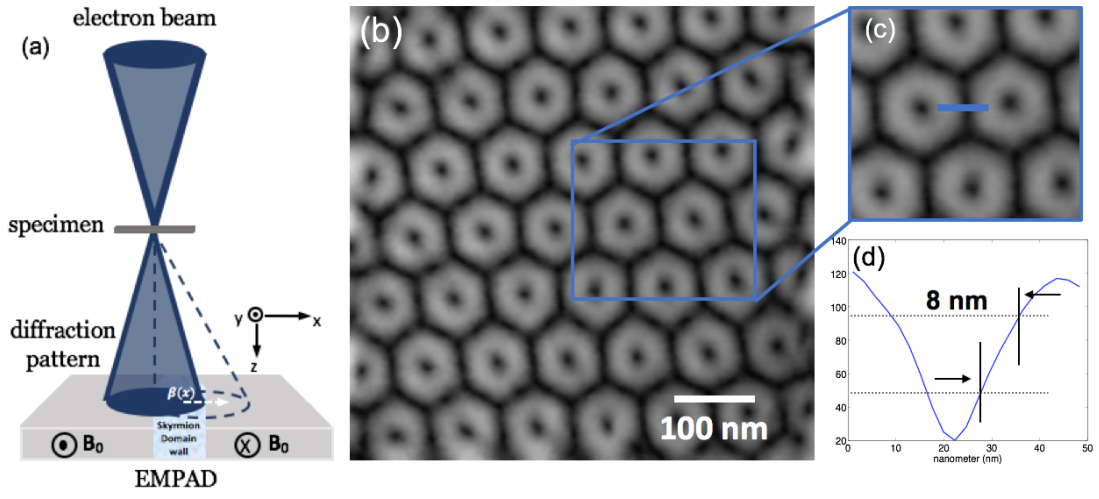

FIG. 3.6. (a) Schematic of magnetic imaging with EMPAD in LSTEM mode. We capture full CBED pattern with the electron microscope pixel array detector (EMPAD) at every scan position, from which we can also reconstruct the (b) magnitude where (c)

represents the inset of (b) within which a (d) line profile is drawn corresponding to an edge resolution of 8 nanometers.

3.5 Magnetic Imaging of Chiral Sputtered B20 FeGe on Silicon

Although our results show superior imaging for single crystal material, it is even more important that we observed real sputtered materials on thin films typically used in spintronics devices, where disentangling magnetic from grain contrast becomes extremely important. Sputter-deposited B20 FeGe on Si is a model system for the study of chiral magnetic textures that are being actively investigated as the basis for a low-power, high-density magnetic memory technologies in a scalable material platform. Although Lorentz transmission electron microscopy and differential phase contrast imaging each provide the requisite spatial resolution to probe chiral magnetic textures in single-crystal FeGe, probing the magnetism of sputtered B20 FeGe is more challenging because of the sub-micron crystal grains. Such small-scale structure can create imaging artifacts such that the signal from grain contrast and the signal from magnetic textures can be difficult to distinguish.

As a test specimen, we first perform LSTEM with the EMPAD on FeGe sputtered on holey carbon grid. We observed magnetic domains formed when we cooled our sample to 100 K (Figure 3.7a). These magnetic domains are not observed at room temperature (Figure 3.7b). In addition, we measured the magnetic field of our sample and found that we have an in-plane saturation field of -0.2 T and a spatial resolution of 7 nanometer

(Figure 3.7a) by the performing the edge resolution test. This resolution can be further pushed if we apply other techniques to our data set such as electron ptychography. From our results, we show that (i) the EMPAD has superior field and spatial resolution and (ii) when detecting small magnetic deflections the number of electrons matter more than the number of pixels on our detector.

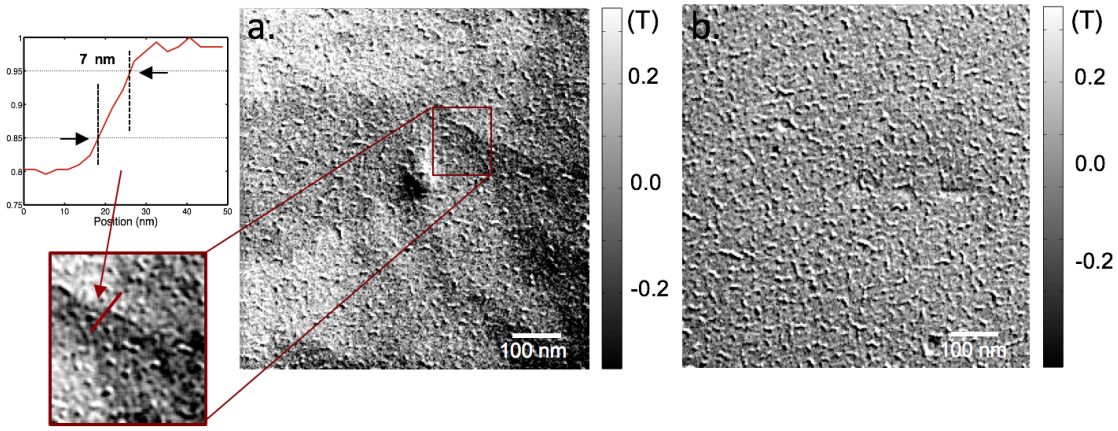

Figure 3.7: Magnetic imaging of FeGe sputtered on silicon nitride TEM grids using the EMPAD at (a) 100 K and (b) room temperature – 300 K. Here we observed magnetic domains of FeGe formed when imaged at cryogenic temperatures with an edge-resolution of 7 nanometers.

In this sample, the magnetic domains are much larger than the grain sizes and it is easier to distinguish the domains from the grains. However, when the two are comparable in size, we must think of a mechanism to distinguish the two effects from each other.

3.6 Previous Works on Disentangling Grain and Magnetic Contrast

As a starting point to establish a method to effectively disentangle grain effects from magnetic contrast, we must first consider how electron scattering is affected when both are present. Here, we build on previous works. Previously, Chapman et al. [59] showed that by using an annular quadrant detector instead of a solid quadrant detector, high spatial frequencies coming from grain contrast and low spatial frequencies from magnetic contrast signals can be controlled and separated from each other by modifying the collection angles of the detector. Kohl et al. [37] discussed how the annular cut-off angles relative to the direct electron beam, the bright field disk, can provide a low-pass filter for the image, enhancing the magnetic field signals as they are slowly varying long-range potentials. Diffraction contrast from grains and grain boundaries, on the other hand, are encoded as short-range potentials where this signal can be smaller than the probe size for a large electron beam. Krajnak et al. [60] showed that enhanced magnetic contrast can be achieved by suppressing the non-magnetic features by cross-correlating the intensity distribution inside of the bright field disk. Lastly, Cao et al. [61] explored the frequency limits relative to the long-range potentials represented as magnetic fields and the short-range potentials from grain contrast represented as high frequencies inside of the bright field disk.

3.7 Our Technique for Disentangling Grain from Magnetic Contrast

From the studies described above, we propose a method where we treat grain contrast as the intensity distribution inside the bright field disk giving rise to the short-

range potentials and the magnetic field as the slowly-varying long-range potential whose signal shifts the entire bright field disk[16]. We use sputtered B20 FeGe (176 nm) thin film on Silicon to test our method where we polished our sample in plan-view using a 1-3 degree polishing angle to remove the silicon region exposing a thin wedge of free-standing FeGe. Then we cooled our sample to 100 K with the objective lens off on the FEI-Tecnai F20 at 200 keV using a semi-convergence angle of 200 microradians. Here, we observe helical magnetic textures formed by the sputtered B20 FeGe on silicon substrate [57, 62] within different grains. To disentangle magnetic effects from grain contrast as long-range and short-range potentials, we vary the aperture sizes on the collected diffraction pattern. We choose aperture sizes of 50, 200, 400 and 10,000 μrad (Figure 3.8 a–d), corresponding to the radius of the apertures. When the aperture sizes are smaller than our semi-convergence angle (~200 μrad) (Figure 3.8a and 3.8 b), we find that the signal only comes from the short-range potentials - grain contrast; in this case, the signal for the magnetic field is not observed (Figure 3.8 e and Figure 3.8 f]. By increasing our aperture size to 400 μrad (Figure 3.7 c), which is slightly larger than our semi-convergence angle, our magnetic field signal appears (Figure 3.8 g). When we extend our aperture size to 10,000 μrad (Figure 3.8 d), we find that we get the signal for the magnetic field and grain contrast (Figure 3.8 h), similar to Figure 3.8 g, although the signal here is dominated by thermal diffuse scattering. Here, our magnetic field signal is not as sharp as in Figure 3.8 g. We realize that the ideal electron distribution range for magnetic imaging comes from choosing an aperture angle that is slightly larger than our semi-convergence angle. By exploring the short and long-range potentials as electron distribution of our diffraction pattern, we can enhance the signal for magnetic

fields (Figure 3.8 i) while decoupling it from the grain structures (Figure 3.8 j).

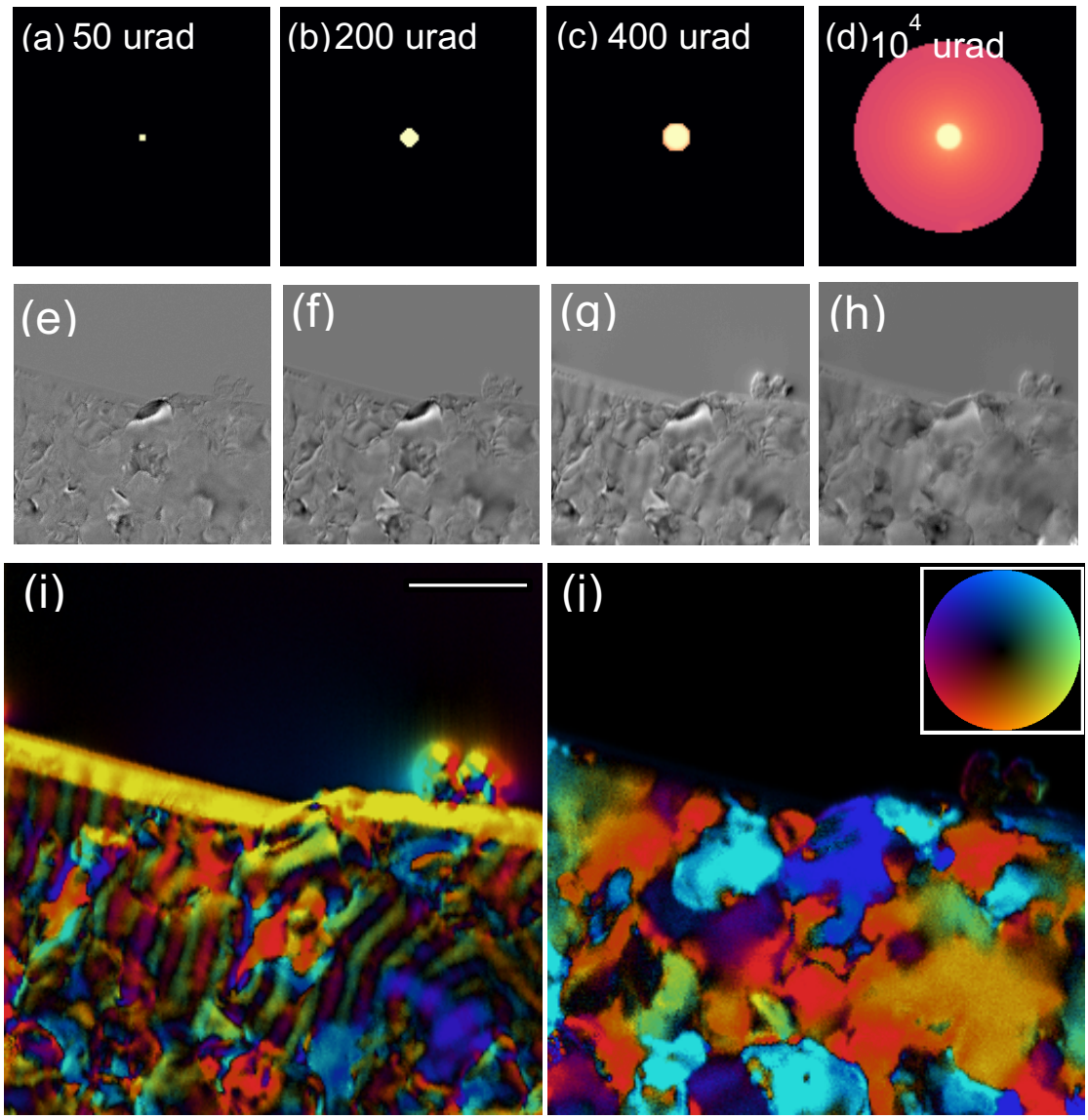

Figure 3.8. Optimizing magnetic contrast by varying the aperture size. Here we calculate our center of mass <P> with aperture sizes extending from (a) 50 µrad (b) 200 µrad (c) 400 µrad and (d) 10^4 µrad where the <P> images corresponding to apertures a – b is shown in figures e –h . By extracting the grains from the magnetic fields, we can decouple the fields from the grain structures where (i) is the image of the magnetic field and (j) shows the grain structures. White scale bar in (i) is 200 nm.

The ability to image through structural features and magnetic effects congruently has also enable us to study changes of the helical vectors along the boundary of individual FeGe grains, previously shown by electron back scattering diffraction (EBSD) to be twinned causing opposite crystal chirality [57]. For this analysis, we first reconstruct a dark field image (Figure 3.9 a) of the top leftmost spot in our diffraction pattern (Figure 3.9 c) to distinguish individual grains from one another. Then by using our technique, we decouple magnetic from grain effects and observed a shift in the phase of the helical vectors as it glides the grain boundaries on two distinguishing grains labeled as [c] and [d] in Fig. 3.9. Such shifts have not been observed in LTEM imaging of single crystal FeGe. In addition, from individual diffraction patterns of grain [c] (Figure 3.9 c) and grain [d] (Figure 3.9 d), we find that the two grains have generalized grain orientations, corresponding to an in-plane rotation of the grains. From our observation using LSTEM with the EMPAD and that from EBSD, we find evidence that the shift in phase could be coupled with the crystal chirality.

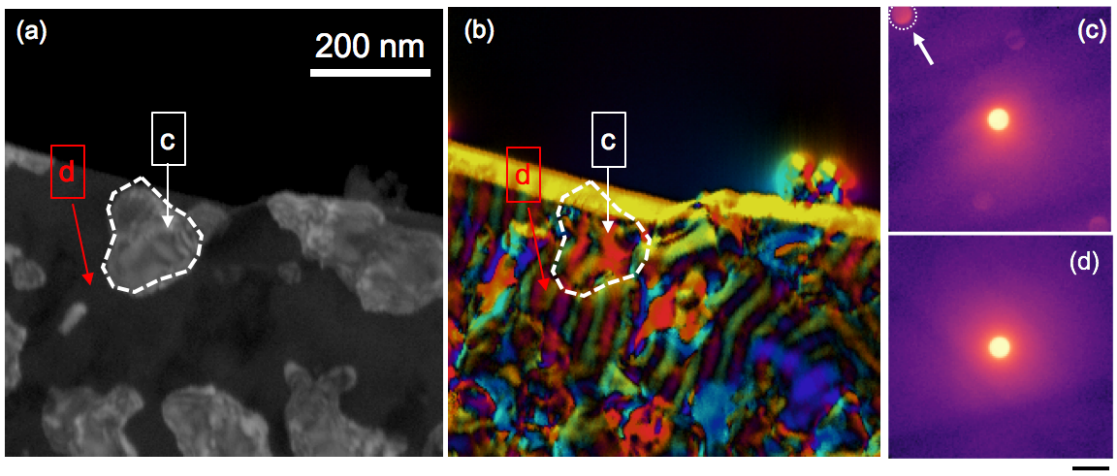

FIG. 3.9: By analyzing the grain orientations shown in the dark field image in (a) and we relate it to the magnetic field image in (b). From which, we observed that adjacent grains c and d have a generalized grain orientation, corresponding to an in-plane rotation. In addition, we observed a shift in helical vectors as it moves across the grain (c) and (d). We chose the top left spot in (c) to form our dark field image in (a). Black scale bar under (d) represent 600 micro-radians.

3.8 Micromagnetic Simulations

In order to confirm our hypothesis, we investigate the effects of the twinned grains on the helical configuration by performing micromagnetic simulations with Mumax3 [63]. We first randomly generated grains with 320 nm average size using Voronoi tessellation [63] (Figure 3.10 a). Then, in Figure 3.10 b, we assign either positive or negative DMI coefficients to these grains again randomly. From magnetometry measurements, we confirmed that our films have a small easy-plane uniaxial anisotropy, K_u, approximately -3500 J/m^3 [17]. In our simulations, we vary K_u

between 0 and -3000 J/m^3, to account for this effect. We note that the samples prepared for the current LSTEM study may have different K_u due to mechanical polishing and thickness variation. We initialize the system into a random magnetic configuration and allow it to micromagnetically relax to its ground state, which is shown in Figure 3.10 c. We notice that that helical vectors shift at the grain boundaries by a half pitch, which is in agreement with our LSTEM observation. Therefore, we conclude that for FeGe on Si[111], the crystal grain orientation couples to the crystal chirality, and thus to the DMI.

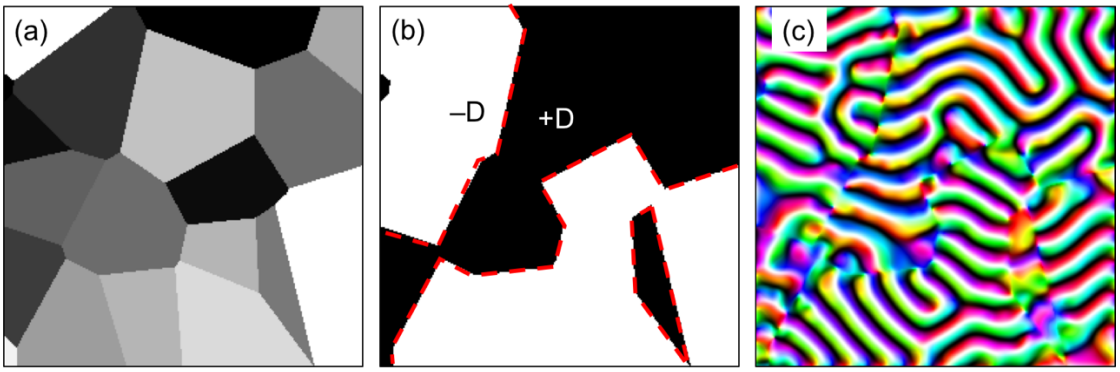

Figure 3.10. Micromagnetic simulations of disordered medium of FeGe thin films. (a) shows randomly generated grains, in which the opposite sign of DMI coefficient assigned to these grains (b). (c) shows the relaxed ground state spin texture, where spatial shift of the helical vector is observed. The simulation window is 1024 nm x 1024 nm.

3.9 Electron Energy Loss Spectroscopy on Sputtered B20 FeGe on Si

In addition, to aid our understanding as to how the effects of grain has on both

the crystal chirality and thereby the magnetization, we perform electron energy loss spectroscopy on our sample to find the chemical compositions of the grains (Figure 3.11). We observed that the helical phases are present only in regions of free-standing FeGe, whereas FeGe regions supported by Si shows no clear helical states. This is an important confirmation about the nature of magnetic phases of epitaxial B20 phases, which has been an outstanding question, i.e. how much the substrate induced stress affect the skyrmion phase? Many neutron scattering experiments have found to have only helical and conical phases in sputtered FeGe films [64-67], however, some topological Hall effect measurements have been interpreted as the existence of the skyrmion phase[62, 68]. Here, we show that suspended FeGe films can stabilize in-plane helices, therefore we assert that magnetic skyrmion can be realized in these suspended films as in the single crystal FeGe. However, FeGe films on Si substrate have easy-plane anisotropy that may prevent skyrmion formation [65].

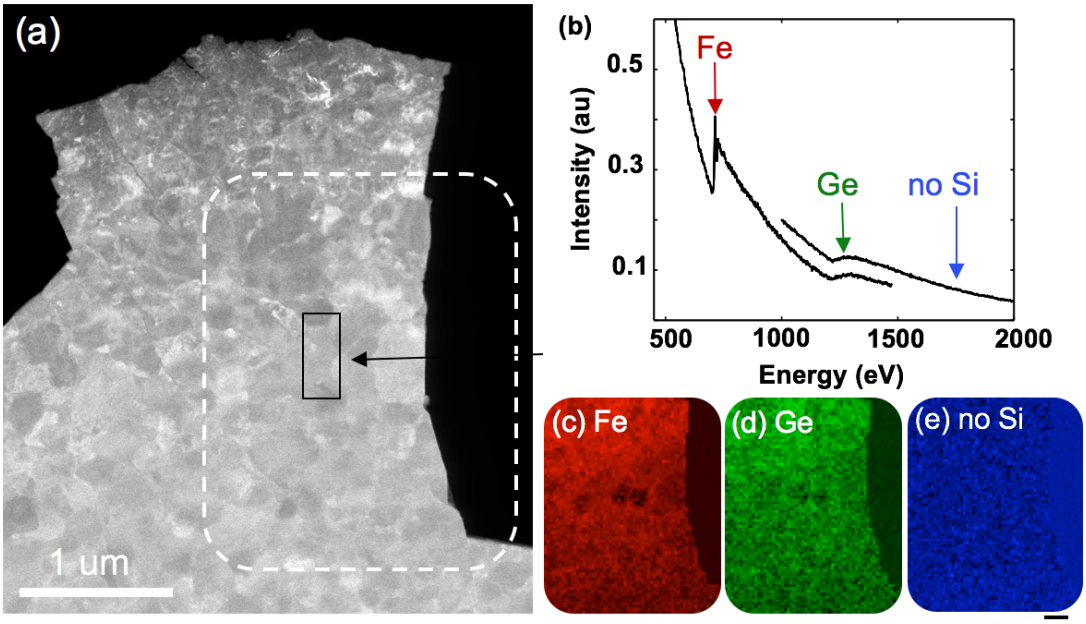

Figure 3.11: We find that magnetic images only occur in free standing FeGe where we perform electron energy loss spectroscopy (EELS). (a) The ADF image shows the region where the EELS has been done where (b) shows the Fe signal and (c) shows the Ge signal. EELS reconstructured images of (d) Fe, (e) Ge and (f) FeGe overlayed. From which, we observed that there is no Si underneath the sputtered FeGe such that the FeGe is free-standing. Black scale bar underneath (e) is 200 nm corresponding to images (c-e).

3.10 Conclusion

In conclusion, we have shown that the LSTEM with EMPAD can provide us with superior magnetic field resolution of sub-milliTesla along in addition to high spatial resolution ~ 7nm. From which, we have developed a technique that allows for decoupling of magnetic and grain contrast by filtering the signals long-range (magnetic contrast) and short-range (grain contrast) potentials for thin film of sputtered B20 FeGe on silicon. We observed that there is a shift in the helical vectors as it glides between grain structures. By performing micromagnetic simulations, we generate random grain orientations and signs of DMI. From which, we observed that the DMI is coupled to the crystal chirality, which can dictate how the helical vectors change when going in between grains. Our technique can also be applied to other chiral magnets where the acquisition of the CBED pattern at each scan position allows for the capture of the full specimen signature. Here, understanding the nanoscale physical and magnetic properties of chiral magnetic materials is key to advancing both fundamental scientific

and industrial point of views.

CHAPTER 4

NEW PHYSICS FROM IMAGING FERROELECTRIC POLARIZATION VORTICES

Topological states of electrical polarization have emerged as an area of research having both fundamental [4] and technological relevance [69]. While absent in bulk, non-trivial polarization field textures, including structures with ferroaxial or toroidal order parameters, were predicted to arise from the close interplay between the geometry of low-dimensional structures and the topology of the polarization field $\boldsymbol{P}(\boldsymbol{r})$ [70-71]. The resulting vortex-like topological features which arise from continuous rotations of the polarization field can be characterized by the electric toroidal moment order parameter, $\boldsymbol{g} = \frac{1}{2}\int \boldsymbol{r}\times\boldsymbol{P}(\boldsymbol{r})\, d^3\boldsymbol{r}$ [72 -74], where $\boldsymbol{r}$ locates the position of the local polarization, giving rise to a host of new (e.g. pyrotoroidic, piezotoroidic, electric toroidal susceptibility) coupling mechanisms. Theoretical studies have suggested possible routes to control ferroelectric order parameters in ferroelectric nanostructures [75-76], and recently vortex-like textures of electrical polarization has been experimentally stabilized [77]. These were achieved in ($SrTiO_3$)/ ($PbTiO_3$) superlattices [77], where the balance between electrostatic and strain boundary conditions resulted in nanometer-scale polarization vortex arrays possessing an electric toroidal moment.

Here, ferroelectric polarization vortex arrays in $PbTiO_3$/$SrTiO_3$ superlattice show topological features with toroidal order analogous to magnetic textures like skyrmions. Previously, measurements of their polar displacements with aberration-corrected

annular dark field scanning transmission electron microscopy (ADF-STEM) have been observed – however – this limits the field of view and sensitivity where picometer sensitivity in real space where observations are usually susceptible to scan noise and distortions Figure 4.1. In addition, soft x-ray dichroism measured on these samples has been interpreted as resulting from an underlying macroscopic chirality from ordered regions of vortex-like polar line defects [78]. While these studies provide a spatially averaged measurement of the ferrotoroidal state, the microscopic details of this state are still unclear.

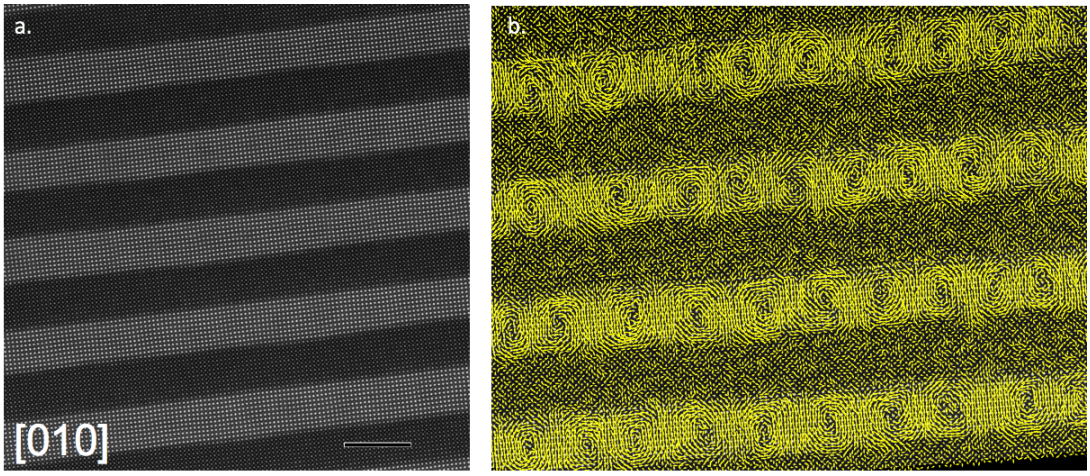

Figure 4.1. 10 x 10 $PbTiO_3/SrTiO_3$ superlattice of a) Annular dark field (ADF) image overlayed with (b) a map of the pico-meter displacement highlighting the polarization vortices [77].

In our study, we describe a 4-dimensional diffraction imaging methodology to quantitatively image the physical properties of the polarization vortices - polarity, toroidal order and the local energy landscape – giving us multiple natural order

parameters of the system. All of this is enabled by the high-speed (0.86 ms readout), high-dynamic-range (10^6:1) electron microscope pixel array detector (EMPAD) [4] developed at Cornell which captures the full convergent beam electron diffraction (CBED) pattern at each scan position. From which, we can uncover components of the macroscopic polarization.

Here, we show that the probability current flow, $\langle \boldsymbol{P} \rangle$, of conjugate diffraction disks tracks the changes in polarity and when reconstructed into an image, provides a direct visualization of the polarization vortices. The electric toroidal moment of the sample supplies a torque to the electron beam resulting in a transfer of orbital angular momentum (OAM), in units of $\hbar$**,** to the electron beam that is recorded on the EMPAD. By measuring polarity, p, and electric field, E, independently and simultaneously on the EMPAD, we use the relation $U = \vec{p} \cdot \vec{E}$, to extract the local electrostatic energy landscape of our system. The second derivative of the local energy with respect to polarity gives the capacitance of that region, showing regions of negative differential capacitance in the core of the vortices. These are the key physical parameters needed to design scalable ferroelectric devices, and adds functionality to the electron microscope at a spatial resolution inaccessible by any other tool.

4.1 Polarity Measurements Arising for Non-Centrosymmetric Crystals

The realization of polarization vortices in $(PbTiO_3)_{12}/(SrTiO_3)_{12}$ superlattices reveal an effective nonzero curl $\nabla \times \vec{P}$, from which polarity measurements would enabled

a detailed description of this occurrence. In this chapter, we investigate the non-centrosymmetric variations in the CBED patterns of $(PbTiO_3)_{12}/(SrTiO_3)_{12}$ superlattice by the EMPAD (Figure 4.2 a) where Friedel's rule is broken by the non-centrosymmetry of the crystal. We build on recent work used to recover the electric and magnetic fields from measurements of probability current flow in a thin sample [36, 43, 52, 79] with a momentum-sensitive detector [41, 44]. Here, we developed an electron microscope pixel array detector (EMPAD) that functions as a compact and high-speed, high dynamic range electron diffraction camera (Figure 4.2a) to meet the specifications needed for very sensitive polarity measurements. The EMPAD has single electron sensitivity with a signal to noise (SNR) of 140:1 for a single electron at 200 keV[40, 80]. It has an exceptionally high dynamic range 10^6:1, where it could detect 1 or 1 million electrons without saturating the detector, and reads out an image frame in 0.86 ms. These properties allow us to rapidly record a diffraction pattern containing all the transmitted electrons, including the central beam, at every probe position in a real-space, even atomic-resolution, image [81].

Using the EMPAD, we can recover the four-dimensional phase space which contains sufficient information for us to simultaneously map electric fields and polarity. To do so, we start with the scattering physics of Fig. 4.2a (for a more detailed derivation, see Methods): The incident electron beam's wavepacket, $\Psi_0(\vec{r} - \vec{r}_p)$, is focused on the sample as a diffraction-limited probe centered at $\vec{r}_p$. The exit wave scattered from the sample is $\Psi(\vec{r}, \vec{r}_p)$. The detector is placed in the back focal plane and records the Fourier

transform of the scattered beam as the diffraction pattern $\left|\Psi\left(\vec{k},\vec{r}_p\right)\right|^2$, with $\vec{k}$ and $\vec{r}$ as conjugate variables in the back focal plane and image plane respectively. Measurements in the diffraction plane are momentum-resolved and the average linear momentum transfer $\left\langle\vec{p}\left(\vec{r}_p\right)\right\rangle$ is the center of mass (CoM) of the diffraction pattern $\left\langle\vec{p}\left(\vec{r}_p\right)\right\rangle = \int \hbar\vec{k}\left|\Psi\left(\vec{k},\vec{r}_p\right)\right|^2 d\vec{k}$ [43, 52, 82]. Transforming to a position basis (see Appendix, Eq. S3), the expectation value of probability current flow is $\langle\vec{j}\rangle = \langle\vec{p}\rangle/2m$, converting the CoM maps to probability current images [43, 52]. From Eherenfest's theorem, or using the strong phase approximation, $\left\langle\vec{p}\left(\vec{r}_p\right)\right\rangle = \hbar\sigma\left|\Psi_0\left(\vec{r}_p\right)\right|^2 \otimes \vec{\nabla}V\left(\vec{r}_p\right)$, where the exit wavefunction is just a product of the initial wavefunction, Ψ_0, and a phase term from the sample potential, $V\left(\vec{r}\right)$, the probability current flow is proportional to the Lorentz Force on the beam from the sample (with some subtleties in the weighting of the expectation value for thicker samples) [43, 52].

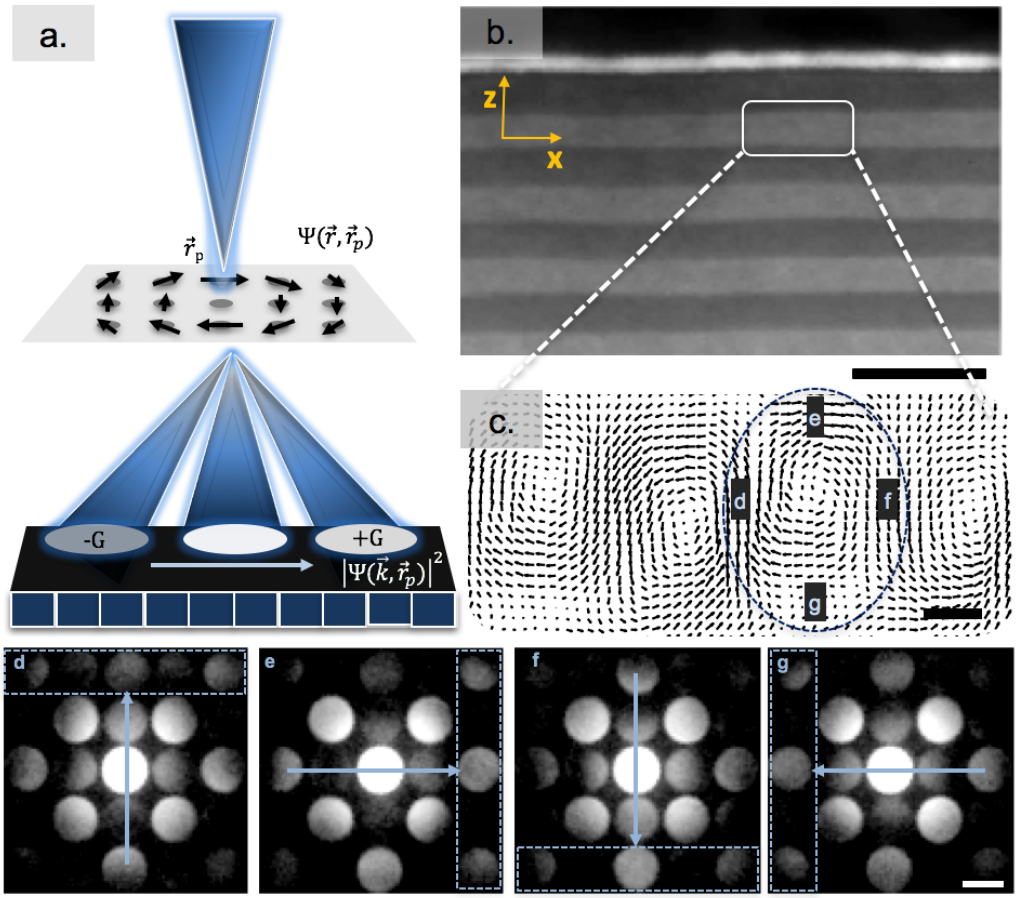

Figure 4.2. (a) Schematic of electron microscopy pixel array detector (EMPAD) placed in the diffraction plane to record the full angular scattering distribution from an electron beam focused onto a sample. (b) Low-Angle ADF image of $(PbTiO_3)_{12}/(SrTiO_3)_{12}$ superlattice. (c) Polarization vortices reconstructed from dashed region in (b). Here, the third vortex is circled and different regions of the vortex (labeled d-g) has their respective convergent beam electron diffraction (CBED) patterns (d-g). We observed that the CBED pattern changes depending on its location with respect to the vortex. Scale bar in (b) is 15 nanometers, (c) is 2 nanometers, and is 6 mrad for the CBED patterns in (d-g) shown in (h).

From the probability current flow, the electric field (or more generally, the gradient of the projected mean inner potential[28] which includes thickness variations) can be reconstructed using the $\vec{G} = (000)$ diffraction disk. From which, we observe small modulations in the macroscopic fields with the EMPAD by first filtering out the atomic fields[20-21] that otherwise dominate the image contrast. We do so by averaging over the unit cell[27], which we achieve by reducing the convergence angle of the beam so that the diffraction disks no longer overlap, producing a real space probe focused down to a spot that is just larger than the unit cell:

$$E(r_0) = \frac{1}{V_c}\int dVe(r)$$

where e(r) is microscopic field defined to be the nuclear field of the atom, and V is the volume over which the polarity encompasses. This provides a spatially invariant signal in a perfect crystal, but retains sensitivity to displacement fields that vary more slowly than the atomic lattice spacing.

In addition, we are no longer restricted to be in the field of view where we can run out of atoms to count.

To map polarity information, this requires finite $\vec{G}$: Figure 4.2 d-g shows the convergent beam electron diffraction (CBED) patterns recorded on the EMPAD from different positions around a polarization vortex (Figure 4.2 c). The momentum distribution is asymmetric and tracks the symmetry of the local polarization vector. Theoretically, it is impossible to uniquely determine the polarization from the

knowledge of the charge density in real space, a problem that is resolved with a Berry-phase treatment in *ab-initio* simulations [83]. For an electron diffraction pattern, the basis-independent and unique experimental solution arises naturally from closed multiple scattering paths which are independent of the choice of origin in real space. The result is a set of inequivalent diffraction intensities for conjugate Friedel pairs [84 - 85] such as the (200) and $(\bar{2}00)$ beams, whose combined CoM tracks the direction of polarity (Figure 4.2 c) in materials that break inversion symmetry.

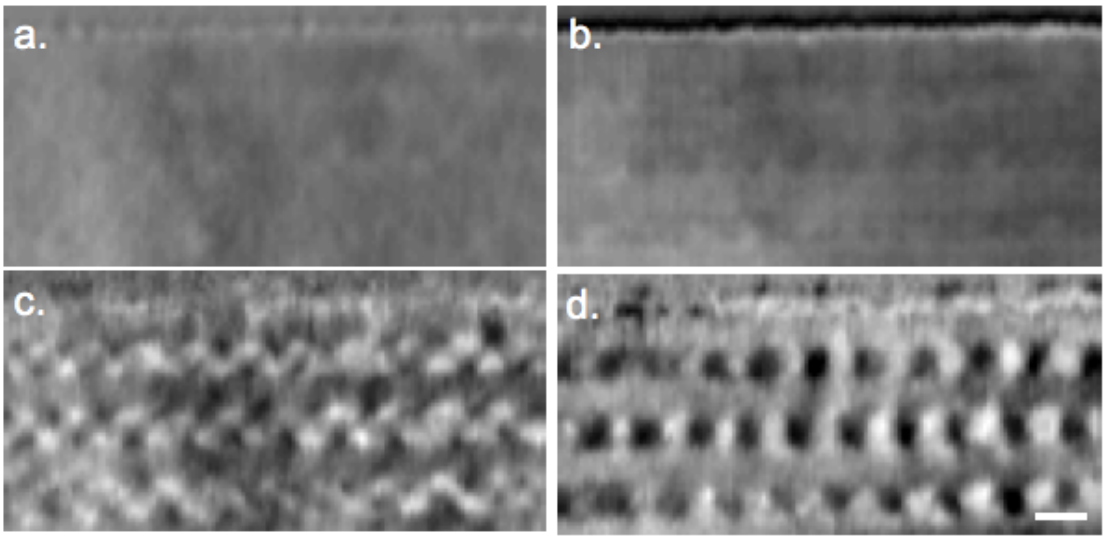

Figure 4.3. 12 x 12 $PbTiO_3/SrTiO_3$ superlattice images of (a) $\langle p_x \rangle$ and (b) $\langle p_y \rangle$ from the 000 disk showing that the sample is flat and that it is not dominated by thickness, tilt or electric field contributions, in addition, there is no polarity information in the (000) disk. To extract the polarization data, we realized that Friedel's law is broken due to an asymmetry in intensities of the conjugated pairs cause by polarity in the sample. Here we took the (b) $\langle p_x \rangle$ (200) and $(\bar{2}00)$ diffracted disks and the (d) $\langle p_y \rangle$ of the (020) and $(0\bar{2}0)$ diffracted disks to show where polarity effects break the centrosymmetry.

Scale bar is 5 nanometers for (a - d).

The strong contrast, when replotted as a vector map (Fig 4.1b and 4.2) shows the polarization vortices clearly. The angular deflections from the internal electric fields seen in $\langle \vec{p}_{000} \rangle$ are small compared to the polarity contrast in the $\{200\}$ beams suggesting little need for correction. As a quantitative test of the relationship between the probability current maps and the polarization in the presence of strong scattering, Figure 4.4 a shows the lateral polarization components of a model vortex using a 2nd principles calculation (see Appendix), while Figure 4.4 b shows the simulated probability current images, $\langle p_x \rangle$ and $\langle p_z \rangle$ (where *x* and *z* are in the microscope's coordinate system and the ***c***-axis of the sample is along *z*), calculated from multislice simulations [86] of the electron beam propagated through the model structure. Here, $\langle p_x \rangle$ and $\langle p_z \rangle$ are processed in the same way as experimental data using Friedel pairs formed from the $\{200\}$ beams, showing good agreement with underlying polarization in Figure 4.4 a.

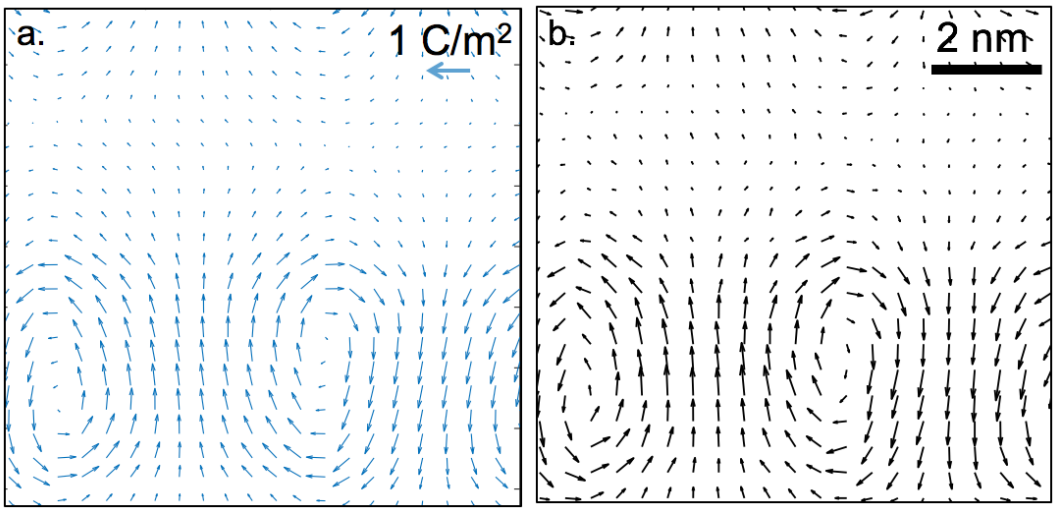

Figure 4.4. Cross-sections along the vortex axis for a simulated 10x10 $PbTiO_3/SrTiO_3$ superlattice: (a) "2nd principles" calculation of the polarization field. (b) Reconstructed vortices from $\langle p_x \rangle$ and $\langle p_z \rangle$ images of the (200) and $(\bar{2}00)$ diffracted disks calculated from the propagation of the electron beam through the simulated structure.

For polarity measurements, we found it was critical to ensure the sample is oriented exactly down the zone axis, as crystal mis-tilts and bends will dominate image contrast when present [79]; therefore, checking polarity images against COM maps formed from the central beam and Kikuchi maps was important. The tilt contrast itself is easy to identify here as it derives from and has the same periodicity as the strain dechanneling contrast seen in the annular dark field (ADF) images. For instance, in the scalar ADF images of Figure 4.5, the vortex and antivortex have similar and scalar contrast. However, the polarity contrast is opposite for vortex and antivortex, leading to double the spacing, and thus displays only the fundamental and not the 2nd harmonic in the Fourier transforms of Fig 4.5e, and f. With small mis-tilts, the tilt and dechanneling derived 2nd harmonic appears in the probability current images, following the ADF image.

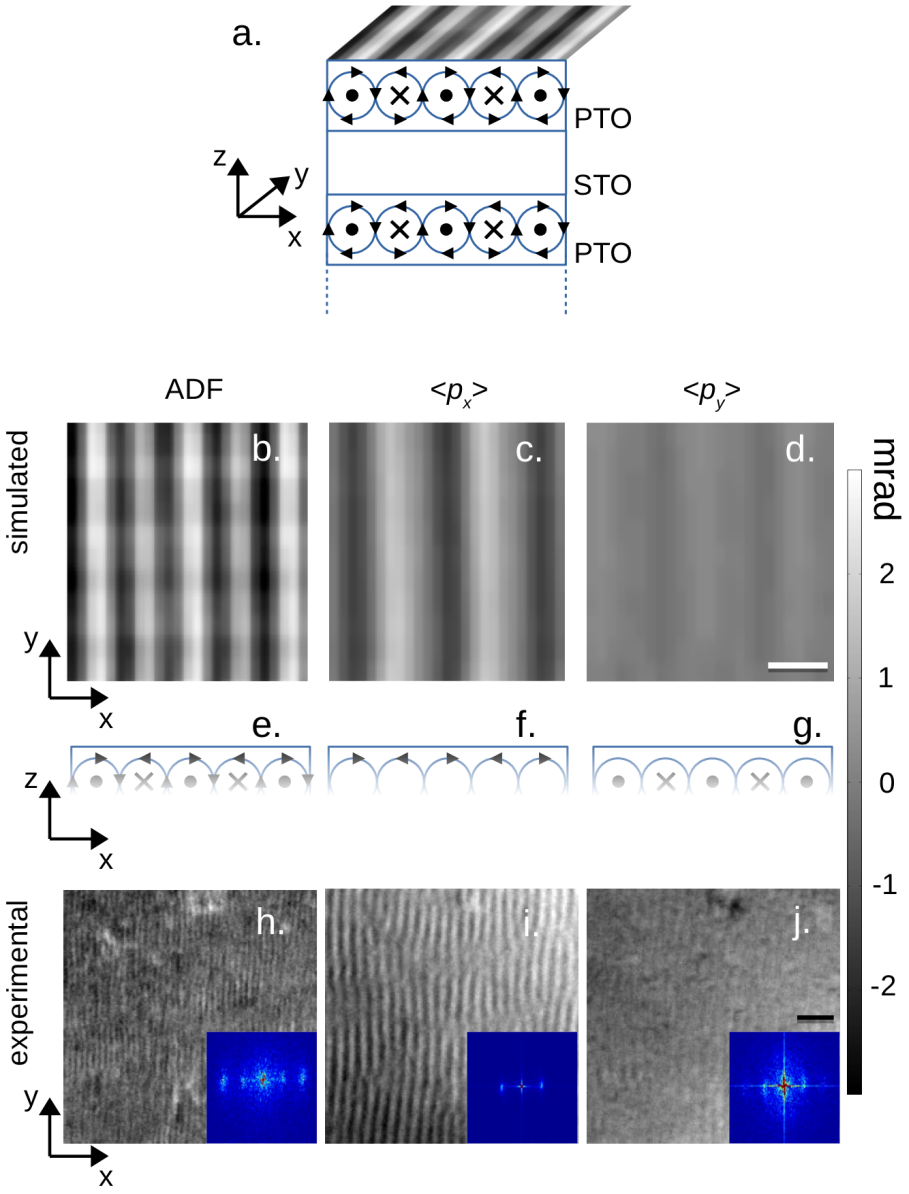

Figure 4.5. Plane view imaging of the polarization textures. The underlying polarization texture relative to the electron microscope image is sketched (a), where vortices in the superlattice are represented as arrows describing circles in the (x,z) plane plus dots and crosses indicating polarization pointing along the positive or negative z axis. (b) Annular dark field (ADF), (c) <p_x> and (d) <p_y> images reconstructed from the coordinates of a 10x10 superlattice using 1.76 mrad semi-converged angle probe at 300 keV. (e-g) Show

the features of the polarization texture for which the measurements in the panels above and below are sensitive. The fading of the sketches in (e-g) represent the fact that the probability current signal comes mostly from the top half of the vortices (see text). Experimental results from 12x12 superlattice using the same imaging parameters as simulation for (h) ADF, (i) $\langle p_x \rangle$ and (j) $\langle p_y \rangle$. By looking at a larger field of view in (h) ADF, and probability current flow (i) $\langle p_x \rangle$ and (j) $\langle p_y \rangle$ we observed that the stripes have higher contrast in $\langle p_x \rangle$ than in $\langle p_y \rangle$, although faint contrast is seen in $\langle p_y \rangle$. Fourier transforms (FT) of (h), (i), and (j) are represented as insets to each figure respectively. Here, we observed double periodicity in the FT (g), while the FT (i) and (j) show single periodicity with the (i) FT of $\langle p_x \rangle$ having 6 times more intensity than the (j) FT of $\langle p_y \rangle$. White scale bar in (d) represents 5 nm. Black scale bar under (j) represents 30 nm.

Electron channeling plays an important role in the depth dependence of the probability current signal where the signal is not a simple projection through the sample. From multislice simulations, the signal from the strongly-scattering Pb columns comes mostly from the top half of the vortex (Figure 4.6), and is scattered away after that. The dechanneling in the two in-plane directions is quite similar as it is dominated by the atomic column more so than the small displacements, where so much of the thickness variation can be compensated by comparing the relative intensities of the $\langle p_y \rangle$ and $\langle p_x \rangle$ components (Figure 4.7). Here in Figure 4.7, we observed that vorticity is still preserved, however, due to electron channeling, the sign of the vortices is switched for every 20 nanometers of thickness.

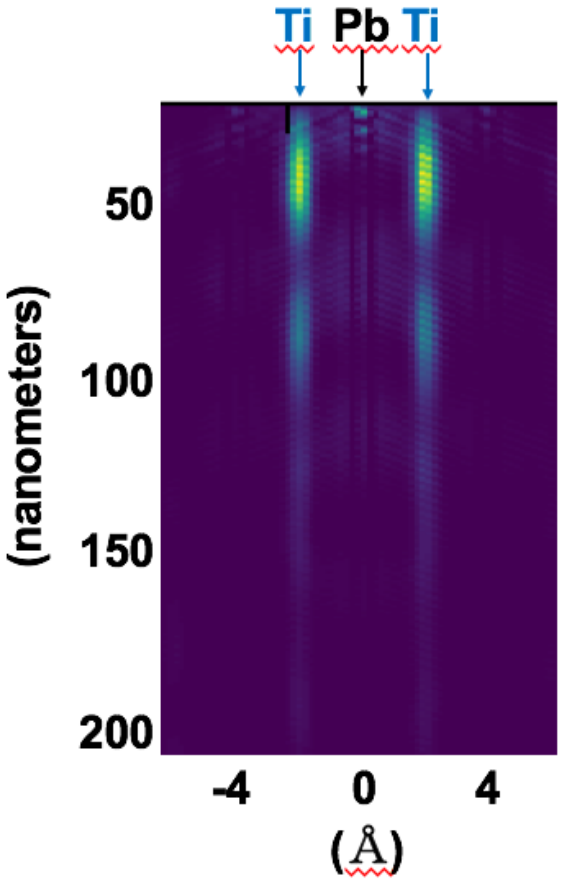

Figure 4.6. Multislice simulation of 6x6 $PbTiO_3/SrTiO_3$ down the [001] zone axis using 1.76 mrad convergence angle at 300 keV. Multislice conditions are the same as experimental conditions used to those recorded with the EMPAD on a FEI Titan Themis.

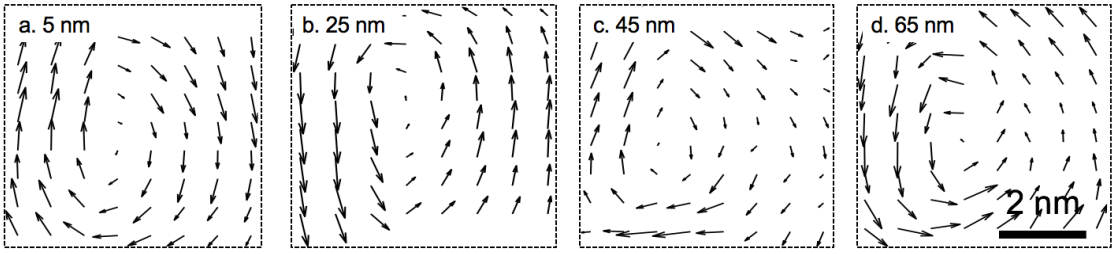

Figure 4.7. Reconstructed vortices from $\langle p_x \rangle$ and $\langle p_y \rangle$ images of the (200) and $(\bar{2}00)$ diffracted disks calculated from a simulated structure at thicknesses of 5, 20, 40

and 50 nanometers. Here, we observed that channeling of the electron beam causes the polarization direction to switch depending on the thickness with a period of 20 nanometers, reflecting contrast reversals in the underlying {200} diffraction peaks from dynamical scattering in the sample. Black scale bar represents 3 nanometers.

To show that the polarization vortices contrast is unique to the $(PbTiO_3)_{12}/(SrTiO_3)_{12}$ structure, we compared to a $(PbTiO_3)_4/(SrTiO_3)_4$, a typical ferroelectric in Figure 4.8. Here, we observed that the contrast from in Figure 4.3 c and d from $\langle p_x \rangle$ and $\langle p_z \rangle$ of the $\{200\}$ and $\{020\}$ beams do not arise in the $(PbTiO_3)_4/(SrTiO_3)_4$ specimen of Figure 4.8 d and e. The polarization vortices have unique contrast and are not an artifact of the experiment. The EMPAD allows investigation of non-centrosymmetric variations in the CBED patterns. However, quantitative reconstruction of polarization and fields can only be allowed if specimen tilt, strains, thickness and dislocations are considered. Therefore, careful investigation and analysis of the full CBED pattern and its symmetries can further our quantitative investigation of the polarization and ferroelectric fields in $(PbTiO_3)_{12}/(SrTiO_3)_{12}$ superlattice.

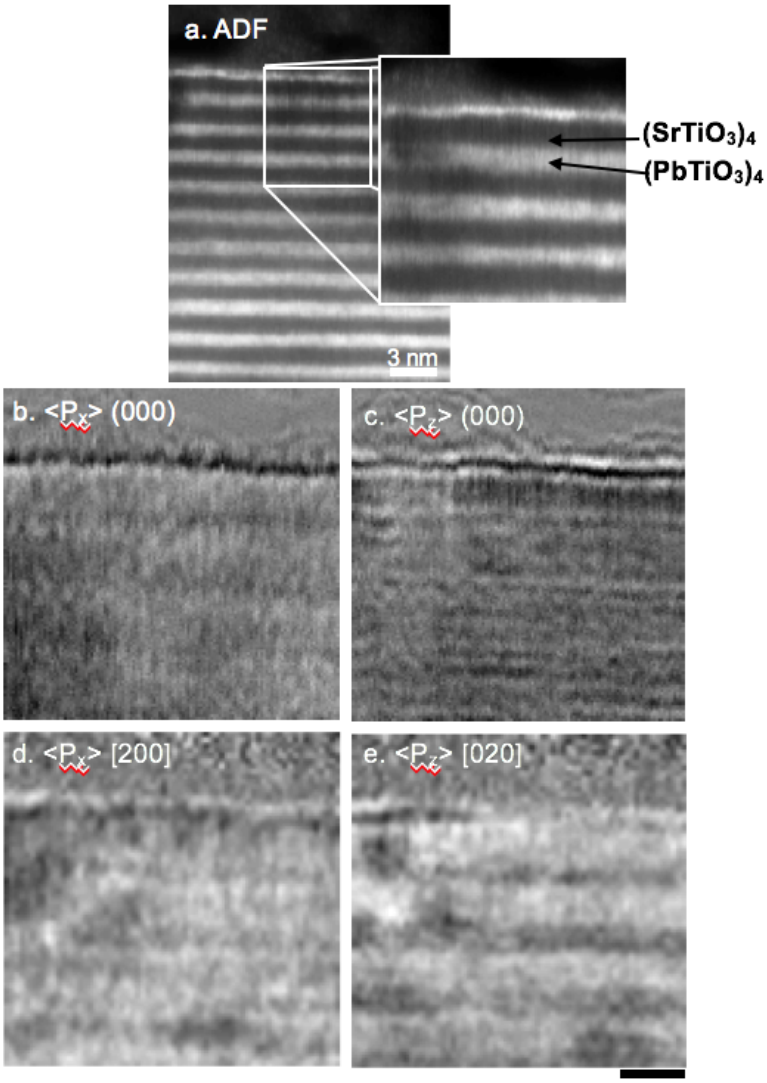

Figure 4.8. 4x4 $PbTiO_3/SrTiO_3$ superlattice has a uniform ferroelectric state without polarization vortices. Here, the (a) ADF image shows higher-atomic number $PbTiO_3$ as the white regions and lower-atomic number $SrTiO_3$ as the darker regions. We performed (b) $\langle p_x \rangle$ and (c) $\langle p_y \rangle$ mapping on the (000) beam to check that the sample is flat and not dominated by sample thickness, and tilt. The only contrast is from changes in the projected potential – both interface charge and mean inner potential. In addition, we perform (d) $\langle p_x \rangle$ on the $(\bar{2}00)$ diffracted disks and (e) $\langle p_y \rangle$ on the (020) and $(0\bar{2}0)$

diffracted disks to map the polarity. Black scale bar under (e) is 3 nanometers for images b-e.

The ability to map polarity with the EMPAD provides an understanding of the how these polarization vortices manifest. By exploiting their asymmetry using the CBED pattern, we can take advantage of mapping the polarization vortices from 1 to 100 nanometers macroscopically compared to aberration correct picometer resolution of polarity - such that we would not run out of atoms to count. In addition, we can also simultaneously and independently probe the electric field in our sample, providing us with more detailed characteristics of our sample than just by ADF-STEM techniques alone.

4.2 Measuring Orbital Angular Momentum and Torque Transfer

Orbital angular momentum and torque transfer play central roles in a wide range of magnetic textures and devices including skyrmions and spin-torque electronics [87 - 90] including analogous topological structures such as polarization vortex arrays in ferroelectric/dielectric superlattices [77], with a potential for rich textures including coexistence of phases, multi-order parameter space and large responses to small external perturbations [91]. Previously, electron microscopy methods for probing OAM have produced angular momentum dependent beams in the form of vortex beams [92 - 94], where the electron probe is divided into three separate beams each with angular momentum, $+l$, 0, and l, respectively. However, because of the division in intensity,

signal to noise remains low.

Here, we show how the natural order parameter of these ferrotoroidal phases, the toroidal moment, can be imaged using the transfer of orbital angular momentum from polarization vortices of $(PbTiO_3)_{12}/(SrTiO_3)_{12}$ superlattices to a focused, high-energy electron beam by building on recent work used to recover the electric and magnetic fields from measurements of probability current flow in a thin sample [43, 52, 82]. with a momentum-sensitive detector [41, 44] (from section 4.2). Its origin can be traced back to the integrated torque transferred to the scattered beam, which can be recovered from the measured probability current flow. Furthermore, our technique can recover OAM and torque transfer with high fidelity and resolution, without compromising the beam shape, and in a geometry where it is possible to simultaneously measure and distinguish electric fields, polarity and crystal tilt, the latter being a serious challenge for traditional approaches such as holography and differential phase contrast [79]. This is all made possible by our new design of a high-speed, momentum-resolved electron microscope pixel array detector (EMPAD) [80] whose high dynamic range allows us to record the complete angular distribution of transmitted electrons.

To date, the electron microscopy approach to measuring OAM has been to start with a beam that has been structured with special apertures to possess a well-defined OAM, such as a vortex beam. In this approach, the vortex beam scatters through the sample and a change is recorded with a localized detector. This approach has been used for magnetic measurements from inelastic scattering [92-96], but precludes the

simultaneous momentum measurements needed to reliably recover polarity in ferroelectrics. Our approach is in a sense to run this experiment backwards, i.e., using a simple and local beam (i.e. with zero OAM), and having it scatter through a sample that has vorticity where the final OAM is recorded with an angle-resolved and phase-sensitive detection method. This allows us to optimize the beam shape for the desired scattering experiment, be it diffraction or atomic resolution imaging. More importantly, it allows us to selectively interrogate the scattering potential in momentum space, and identify the underlying structural distortions that form the ferroelectric polarization vortices.

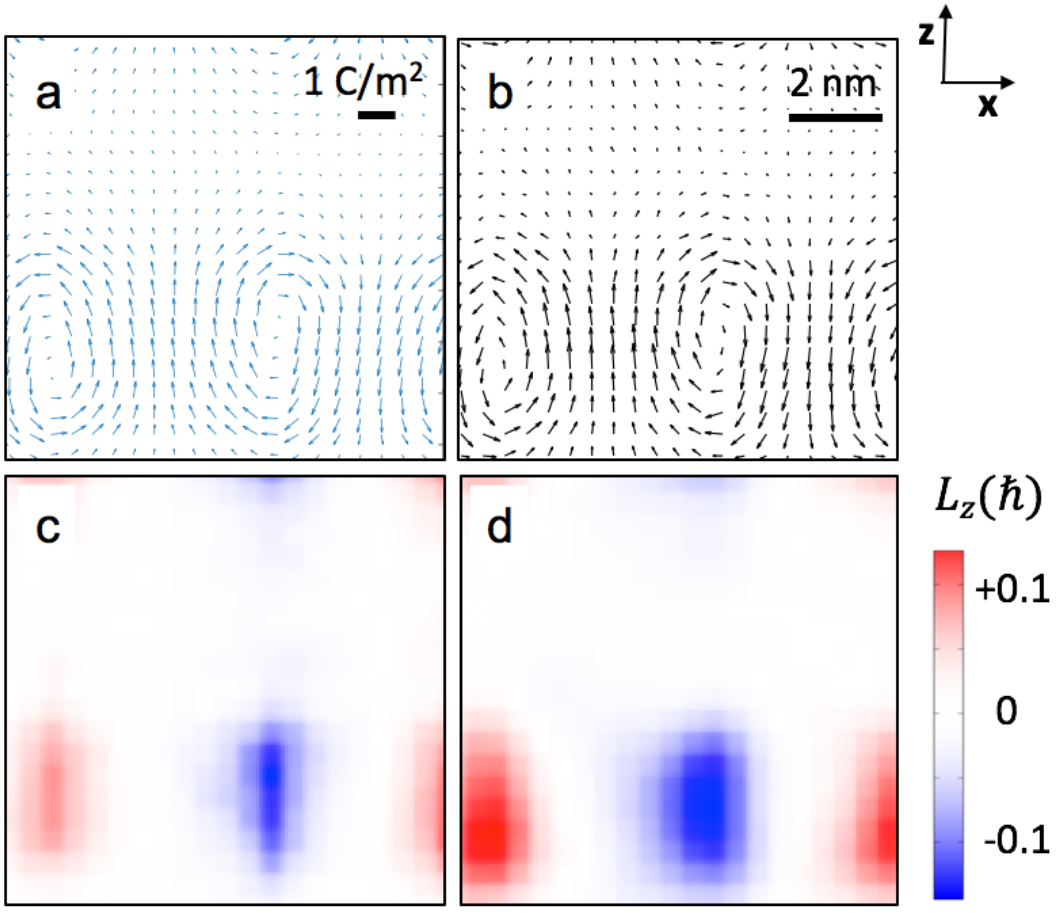

Figure 4.9. Cross-sections along the vortex axis for a simulated 10x10 $PbTiO_3/SrTiO_3$

superlattice: (a) "2nd principles" calculation of the polarization field. (b) Reconstructed vortices from $\langle p_x \rangle$ and $\langle p_z \rangle$ images of the (200) and $(\bar{2}00)$ diffracted disks calculated from the propagation of the electron beam through the simulated structure. (c) Change in orbital angular momentum reconstructed from the full wave function and (d) integrated torque transfer from the electron to the sample calculated from eqn (Appendix, S18) showing good agreement with the exact momentum transfer.

Here, we can explicitly calculate the OAM $\langle \boldsymbol{L} \rangle = \langle \Psi | \hat{\boldsymbol{r}} \times \hat{\boldsymbol{p}} | \Psi \rangle = \int \Psi^*(\vec{r}) [\hat{\boldsymbol{r}} \times \hat{\boldsymbol{p}}] \Psi(\vec{r}) d\vec{r}$ by using ptychography [97-98] to recover the phase and amplitude of the exit wave, which is exact for all sample thicknesses to within the accuracy of the ptychographic reconstruction. However, this approach is computationally intensive and requires high sampling densities in real space. Another approach, which is faster and less restricted by sampling requirements, comes from noting that the time evolution of expectation value of the OAM is given by $\langle \boldsymbol{\Gamma} \rangle$, the torque on the sample, i.e. $\langle \boldsymbol{\Gamma} \rangle \equiv d\langle \boldsymbol{L} \rangle / dt = \langle \Psi | [\boldsymbol{r} \times (-\nabla V)] | \Psi \rangle$. For elastic scattering, the electron travels at constant velocity where the integration over time for the propagation of the wave packet through the sample becomes an integration over sample thickness. We then use the strong phase approximation to connect the probability current images $\langle \boldsymbol{p} \rangle$ to ∇V (see Appendix, Eq. S8-S18). The result provides the $\boldsymbol{z}$-component of the torque (in the microscope's coordinate system) convolved incoherently with the probe shape

$$\langle \Gamma_z(\vec{r}_p)\rangle = \int \left[(\vec{r}-\vec{r}_p)\times(-\vec{\nabla}V(\vec{r}))\right]_z \left|\Psi(\vec{r}_p-\vec{r})\right|^2 d\vec{r}$$

which can be separated in Fourier space, and then corrected for probe shape (equation S18). Since we image in projection, the beam's passage through the through the sample gives $\langle L_z\rangle = \int \langle \Gamma_z\rangle dt$.

To test the numerical accuracy of both torque transfer and direct approaches, we return to the multislice simulations[31] on the model polarization vortex structures. Figure 4.9c is the change in OAM calculated from the expectation value $\langle L_z\rangle$ of the exit wave from the multislice simulation and Figure 4.9 d is the total torque transfer calculated from the CoM images using equation S18, where there is good agreement between the torque and angular momentum approaches for a moderate thickness sample (< 20nm). In thick simulated samples, the two approaches begin to diverge as the strong phase approximation breaks down once beam propagation effects become significant (Figure 4.7).

Our detection scheme overcomes a limitation of real-space imaging; here, the sensitivity is set by the SNR on the detector in momentum space, rather than picometer-scale instabilities in the scan position of the electron beam itself. This greatly reduces the environmental dependence of the measurement, and makes picometer-precision measurements possible over arbitrarily large fields of view as it is no longer necessary to resolve and count individual atoms. A similar approach can also be taken for magnetic systems to simultaneously map magnetic fields and torque transfer. For ferroaxial

textures, $\langle \boldsymbol{L} \rangle$, takes on an additional significance, as it is proportional to the toroidal moment and order parameter $\boldsymbol{g}$ (see Appendix). We return to the experimental $(PbTiO_3)_{12}/(SrTiO_3)_{12}$ superlattice of Figure 4.2 b, with the $\{200\}$ probability current plotted in Figure 4.10a as a vector map to show the ordered arrays of polarization vortices. The vortices have offset cores and slightly asymmetric shapes. Figure 4.10b shows the measured $\langle L_z \rangle$ from the region of Figure 4.10a using the total torque transfer equation S18, and from a larger field of view in Figure 4.10c. Figure 4.10b shows the toroidal ordering is that of off-centered, alternating and asymmetric vortices that lack an axis of symmetry.

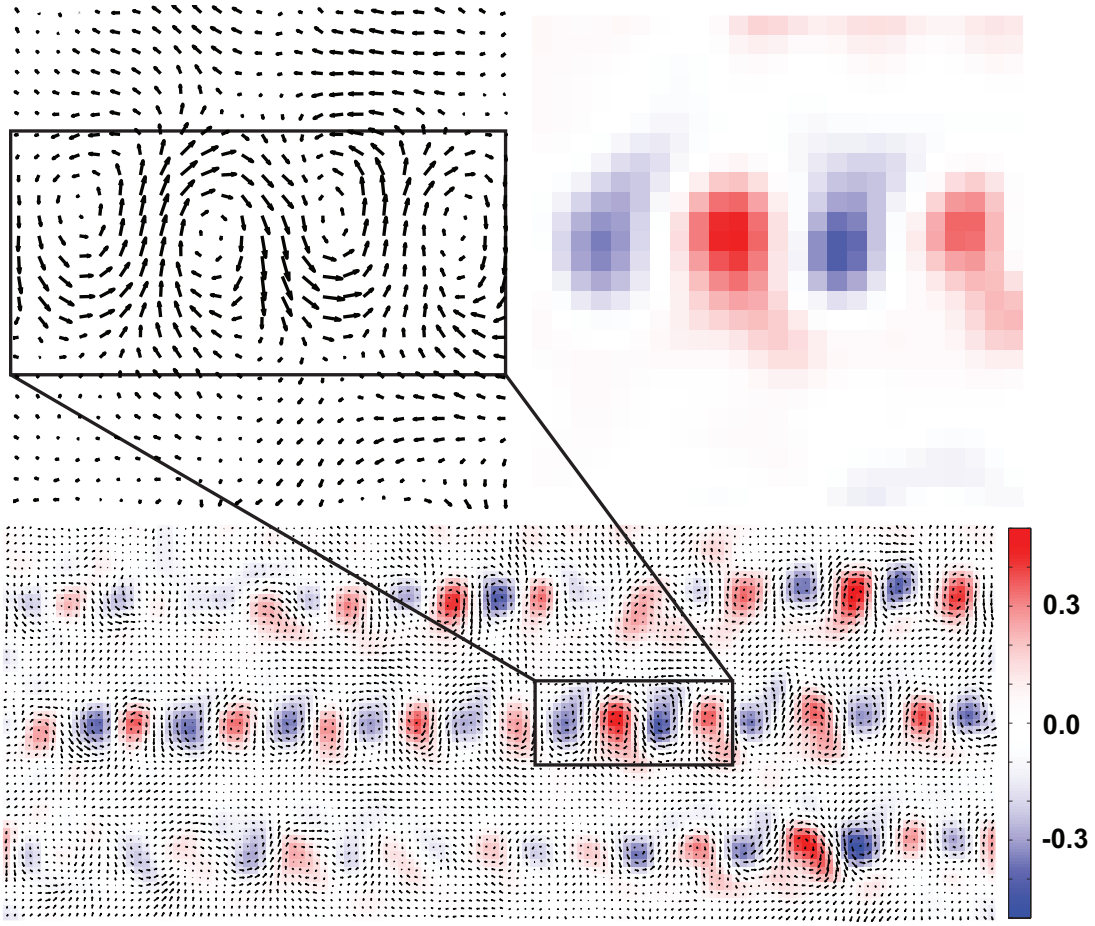

Figure 4.10. (a) Polarity vortices reconstructed from experimentally measured $\langle p_x \rangle$ and $\langle p_z \rangle$ along with (b) the measured torque transfer to electron beam for the same region. (c) Larger field of view of the sample showing torque transfer overlayed with the polarity map. Colorbar shows the change in angular momentum from the torque transfer in units of ħ. Black scale bar in (b) is 2 nanometers and (c) is 5 nanometers.

While orbital angular momentum (OAM) and torque transfer play central roles in a wide range of physical processes and devices ranging from skyrmions to spin torque transfer electronics, recent experimental realization of polarization vortex arrays in ferroelectric

materials offers analogous roles for topological structures encoded in polarization fields. By demonstrating a new phase-sensitive detection method for measuring the OAM of an electron beam where its shape and resolution are not compromised, measurements extracted from this method can range over five orders of magnitude in length scales - making it well suited for measuring polarization fields and torque transfer in complex, extended patterns. From which, we highlight the electron microscope pixel array detector (EMPAD), whose high dynamic range makes it possible to record the complete angular distribution of all transmitted electrons from a focused electron beam at every scanned position, building up a 4-dimensional phase space. Although this imaging method should work equally well for electric and magnetic structures, we observed that this technique is uniquely well suited for imaging the toroidal order parameter of ferroelectric polarization vortex arrays.

4.3 Solving the Chiral Structure of the Polarization Vortices

In this section, we utilize the asymmetry in probability current flow and our technique's high detection sensitivity. From which we show directly how the complex polarization patterns that arise in these heterostructures are chiral, with a non-trivial axial component of the polarization. To determine if the vortex structures are chiral, we need to investigate if there exists a net polarization along the axial direction of the vortex.

To do this, we prepared plan-view thinned samples of the $(PbTiO_3)_{12}/(SrTiO_3)_{12}$ superlattice and imaged down the [001] zone of the superlattice (Figure 4.11a). In this orientation, the net polarity needed for a chiral structure will appear as a non-zero $\langle p_y \rangle$ component on the EMPAD (again *x* and *y* are in the detector coordinate system with *y* along the axial direction of the vortices). Figure 4.11b and 4.11c show $\langle p_x \rangle$ and $\langle p_y \rangle$ images where a small, but non-zero $\langle p_y \rangle$ is indeed detected, having 6 times less intensity than $\langle p_x \rangle$. The reduced axial intensity is a consequence of the strong dechanneling of the electron beam on Pb atom columns (Figure 4.6) which means we do not sample all depths through the sample with equal weighting, here; we observed that most of our signal for $\langle p_x \rangle$ and $\langle p_y \rangle$ comes from the top half of the vortices (shown as the red-shaded region in Figure 4.11a). This reduces sensitivity to the axial component, and is present both for our method and the less-sensitive ADF-based method to measure polar displacements.

To determine the handed-ness of our structure, we first obtain the projected polarization from '2nd principles' simulations, where we sum the intensity of the polarization for only the top half of the polarization vortices from which most of our signal for $\langle p_x \rangle$ and $\langle p_y \rangle$ comes from, to obtain line profiles for right-handed and left-handed chiral structures (Figure 4.11d and Figure 4.11e, Figure 4.12). Here, we observed that a right-handed chiral structure has $\langle p_x \rangle$ and $\langle p_y \rangle$ components tracking one another whereas a left-handed chiral structure show them as out of phase. We then compare it to experimental results where $\langle p_x \rangle$ and $\langle p_y \rangle$ (Figure 4.11 b and c) are shown

overlaid with false color, red and cyan respectively (Figure 4.11h). Here, we observed both right-handed and left-handed chirality (Figure 4.11 f and g); this is aligned with the small signal for chirality observed by x-ray [99] where evidence of both chiralities can reduce the overall signal. From our simulation and experiment, we find that this is a strongly chiral material, exhibiting both right-handed and left-handed chirality.

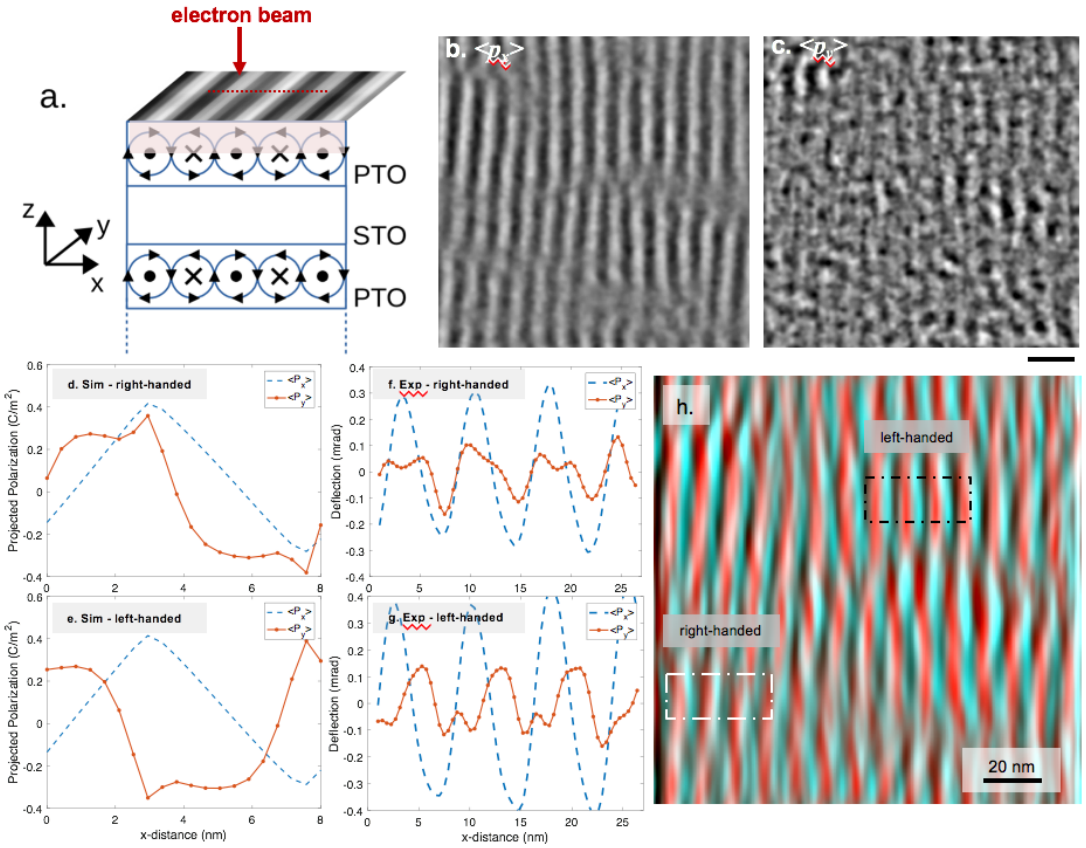

Figure 4.11. Plane view imaging of the polarization textures. The underlying polarization texture relative to the electron microscope image is sketched in (a), where vortices in the superlattice are represented as arrows describing circles in the (*x*,*z*) plane plus dots and crosses indicating polarization pointing along the positive or negative *z*

axis. Here, the top half of the vortices is highlighted in red representing the fact that the probability current signal comes mostly from the top half of the vortices (see text). Experimental images of (b) $\langle p_x \rangle$ and (c $\langle p_y \rangle$ images from a 12x12 superlattice using a 1.4 mrad semi-converged angle probe at 300 keV. We observed that the stripes have higher contrast in $\langle p_x \rangle$ than in $\langle p_y \rangle$, although faint contrast is seen in $\langle p_y \rangle$. "2nd principles" calculation of the polarization field show projected polarization of $\langle p_x \rangle$ and $\langle p_y \rangle$ as line profiles for both (d) right-handed and the (e) left-handed chiral structures. Experimentally, we overlay our results from (b) $\langle p_x \rangle$ and (c) $\langle p_y \rangle$ images with false color in (h), red and cyan respectively. From the line profiles in (h) at two different regions in the same image, we observed both (f) right-handed and (g) left-handed chirality in different domain regions. Black scale bar under (c) represents 20 nm.

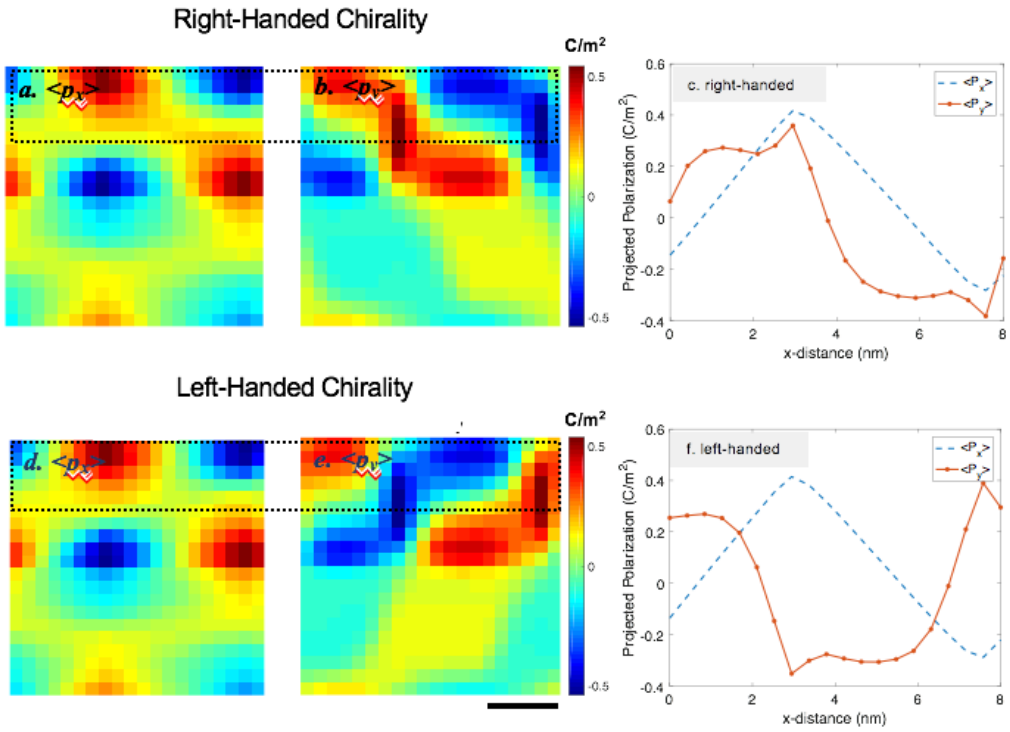

Figure 4.12. "2nd principles" calculation of the projected polarization. Here, we obtain line profiles of the polarization by summing the top half of the vortex structures (shown in dashed line region in a, b, d, and e) from polarization maps $\langle p_x \rangle$ and $\langle p_y \rangle$ for right-handed (a-b) and left-handed (d-e) chiral structures. From which, we observed the projected polarization of $\langle p_x \rangle$ and $\langle p_y \rangle$ for (c) right-handed chirality are in phase and (f) left-handed chirality are out of phase. Black scale bar on the bottom of (e) represents 2 nanometers.

By investigating the chirality of our structure, we observed that the chiral order can either co-exists with or emerge from a polar order. Therefore, we can hardness this chirality leading to the possibility for an electrically controllable phase transition which can give rise to a host of coupling phenomena between the toroidal order and electric and mechanical degrees of freedom.

4.4 Mapping the Local Energy Landscape and Uncovering Negative Capacitance

Negative capacitance is a new equilibrium state of ferroelectric materials that promises to revolutionize modern day electronics by exploiting a region of thermodynamic space that is normally not accessible[1-14] where existing reports of negative capacitance have been focused on its macroscopic realization. Although, these macroscopic properties hints at steady state negative capacitance, they constitute only indirect measurements of the local state of negative capacitance at which the ferroelectric resides. A spatial mapping of this phenomenon is thus critical for a

microscopic understanding, and for the optimal design of devices with potential technological applications. Here we demonstrate a direct measurement of the steady state negative capacitance in a ferroelectric-dielectric heterostructure.

We use electron microscopy in $SrTiO_3/PbTiO_3$ superlattices, to directly determine, the local regions in the ferroelectric material where a state of negative capacitance is stabilized. By measuring polarity, p, and electric field, E, independently and simultaneously on the EMPAD, we use the relation $U = \vec{p} \cdot \vec{E}$, to extract the local electrostatic energy landscape of our system. The second derivative of the local energy with respect to polarity gives the capacitance of that region, showing regions of negative differential capacitance in the core of the vortices. These are the key physical parameters needed to design scalable ferroelectric devices, and adds functionality to the electron microscope at a spatial resolution inaccessible by any other tool.

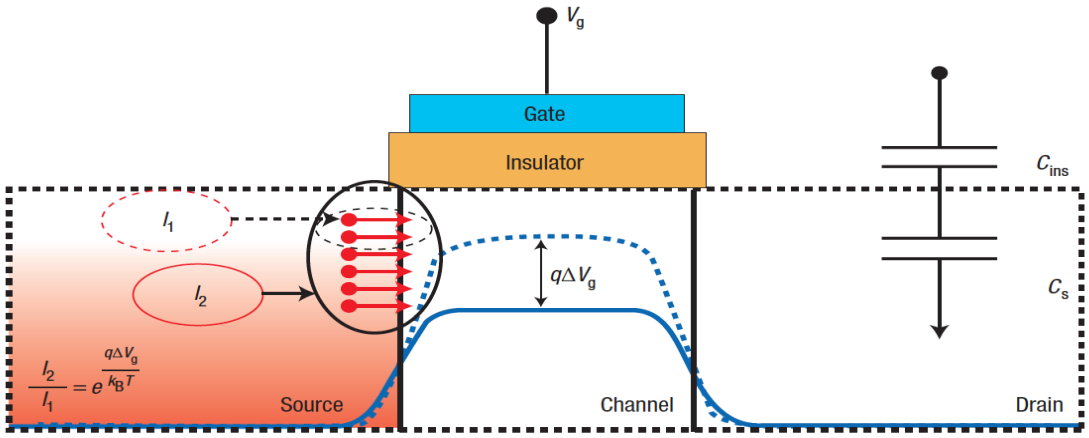

Figure 4.13. Schematic of a field-effect transistor (FET). In a FET, the source, channel and drain are made from a semiconductor, and the energy barrier in the channel is formed by doping. The channel is separated from the metal gate electrode by an

insulating layer. When a voltage is applied across the source and drain, electrons can flow from the source to the drain if they have enough energy to get over the barrier in the channel, resulting in a current of I_2. By increasing the gate voltage, V_g, by an amount ΔV_g, this raises the energy barrier and reduces the current to I_1. However, doing so costs energy and generates heat due to the capacitance of the FET. Using a material that has negative capacitance can aid this process and reduce heat by reducing the switching energy of the device [100].

To understand the impact of negative capacitance practically, it is first easier to discuss its used in a transistor system (Fig 4.13). When you have a capacitor, the potential changes when charge is added - if you add charge, the potential goes up. When I'm trying to make a transistor, voltage applied to dielectric changes the charge in the channel, this tells you the efficiency of the switch in the transistor. If you can change the dielectric function such as replacing the insulator for a material that has negative differential capacitance, this lowers the potential barrier. The cost of adding an electron is reduced instead of raised for a given potential making it easier to get more electron into the channel than with an insulating dielectric alone.

By using the superlattices of $(SrTiO_3)_{12}/(PbTiO_3)_{12}$ as our model Ferroelectric-Dielectric heterostructure system, a state of negative capacitance is expected to be stabilized in the equilibrium where the gradual suppression of polarization near the center of the vortex. We investigate the realization of the negative capacitance by first recovering the local internal energy where we revisit classical thermodynamics. We

know that the internal energy is equal to the change in enthalpy $d\boldsymbol{Q}$ and the change in work $d\boldsymbol{W}$ for a closed system (Equation 1). Here, we assume that temperature is constant (Equation 2), we can get our internal energy from the electric field and the polarization field (Equation 3).

$$dU = dQ + dW \tag{1}$$

$$dQ = 0 \tag{2}$$

$$dW = EdP \tag{3}$$

To demonstrate this, we utilized the EMPAD to perform detailed characterization of phase states. Here, CBED mapping of the probability current flow $<p>$ of conjugate disks, {200} and {020}, quantitatively measures the polarization field (Figure 14 c and d) in a 12 x 12 $SrTiO_3/PbTiO_3$ superlattice[12]. Next, the electric field distribution (Figure 14 a and b) was also measured, whose results are independent of the polarization field from the same region (details in Section 4.2). From our electric field result, we find that the mean inner potential is constant and that our specimen is relatively flat and thickness effects do not dominate our signal – hence the electric field that we observed is due to charge density distribution.

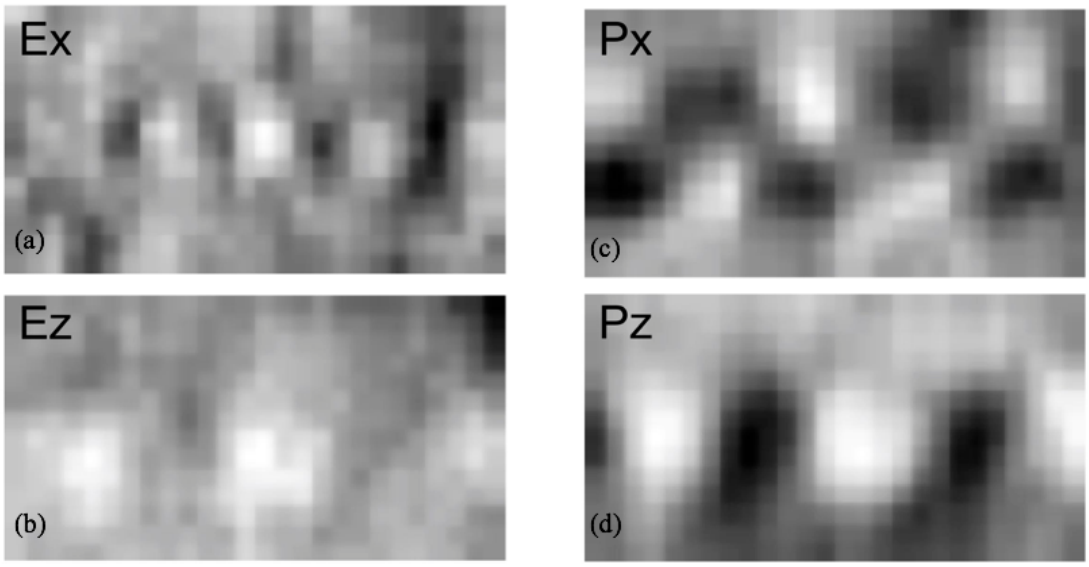

Figure 4.14. We measure the polarization field and electric field independently in the same subregion of a 12 x 12 superlattice,

Here, we derive the z-component of total energy (Figure 4.15 a) by relating our findings back to thermodynamics with a simple integration:

$$U = \int (E_x \frac{\partial P_x}{\partial x} + E_y \frac{\partial P_x}{\partial y}) dx + \int (E_x \frac{\partial P_y}{\partial x} + E_y \frac{\partial P_y}{\partial y}) dy \quad (4)$$

The total energy landscape estimated from this calculation is plotted as a 2-D color map in Figure 4.15a overlay by the polarization field (indicated by black arrows) measured from the same region. We observed that the total energy maintains a local maximum near the core of polarization vortices. As expected, and the regions corresponding to suppressed polarization states coincides with that of local maximum

in the energy landscape. In addition, we observed from our results that the polarization cores are slightly shifted from the centers of the total energy U due to integration from background subtraction. From which regions of suppressed polarization, we observed non-zero polarization states stabilized at or near the local maxima of the potential energy landscape, i.e., where the curvature $\partial^2 U/\partial P^2$ is negative. This gives a mapping of the local energy densities along the x direction as shown in Figure 4.15a. Note how the shape and amplitude of the energy density function looks very similar from core to core. Based on this analysis, we would expect that local regions of negative capacitance will appear in the regions at and near the core.

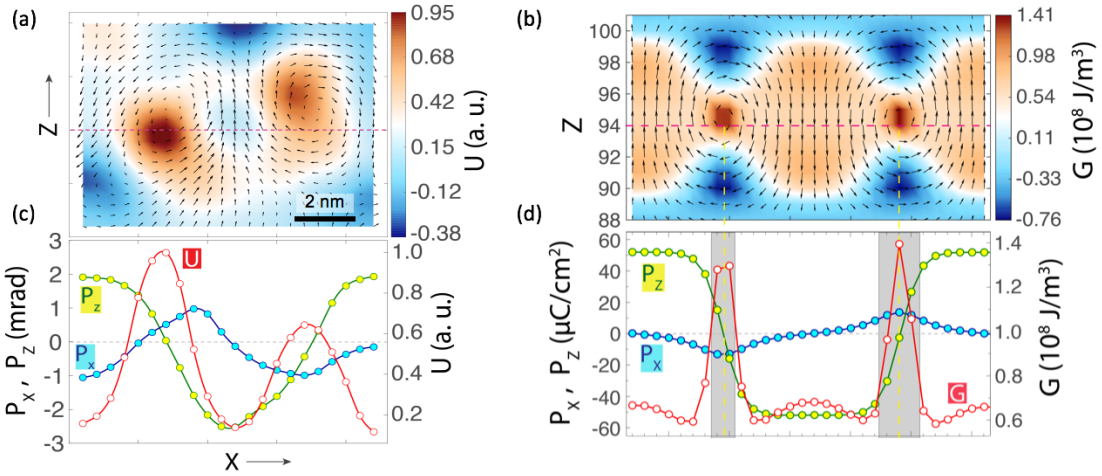

Figure 4.15. (a) The local energy landscape U measurements taken by the EMPAD and (b) local free energy density obtained through the solution of time-dependent Ginzburg-Landau (TDGL) equation for a 10 x 10 superlattice. In a line profile taken from an intermediate region to a core, the evolution of polarization magnitude, indicated by yellow data points connected by green line, exhibits exactly similar behavior where the suppression of polarization when approaching the core and reaching zero at the core.

And, the local free energy density correspondingly approaches a local maximum near the vortex core.

We compare our energy landscape U to the local free energy density result simulated by the time-dependent Ginzburg-Landau (TDGL). From which, we observed that the local maximum in potential energy is reached at the core of the vortex patterns (both clockwise and counter-clockwise) in both Figure 4.15 a and b. We find that the defining characteristic of these topologies, is the gradual suppression of polarization near the center of the vortex configuration from experiment and simulation. Using the EMPAD, we can uncover the occurrence of negative capacitance in vortex structures from a perovskite ferroelectric; from which, we can develop new techniques to perform detailed characterization of local variations in these structures.

4.5 Conclusions

By applying our new detection methods for mapping polar, toroidal order and the local energy landscape, we directly observe the emergence of chirality and negative capacitance in such vortices. This is a direct experimental demonstration that one can take two materials that by themselves are non-handed, but when assembled under certain boundary conditions in which the two primary energy scales (the elastic and electrostatic energies) are almost of the same order of magnitude, they compete with one another. This leads to order parameter topologies that are chiral with a characteristic length scale of 5-10nm. If the chirality can be controlled with an electric field or strain,

this would point to pathways by which the chirality can be used as an independent order parameter. Also, the realization of negative capacitance at the core of such vortices displays regions of larger energy densities. Here, the curvature $\frac{\partial^2 G}{\partial D^2}$ can be estimated to be negative. The fact that two different theoretical models can reproduce the experimental observation indicates that such stabilization in the 'forbidden' region of the thermodynamic landscape should be amenable to predictive material design. The EMPAD allows for multiple capabilities as shown in this chapter where the techniques developed for the polarization vortices can be applied to other material systems leading to further scientific breakthroughs.

CHAPTER 5

CONCLUSION

5.1 Summary

In this dissertation, there were two themes. The first corresponds to the design of the EMPAD and how it compares to the other detectors currently available. The second theme corresponds to the applications of the EMPAD on different material systems.

In the first theme, we noted that the EMPAD was best used as a diffraction-space detector due to its large pixel size ~150 um and also its low numbers of pixels 128 x 128 compared to the pnCCD, Medipix3 and the Gatan K2 Summit. However, from our results, we observed that sensitivity of field measurements is not strongly dependent on the number of pixels on a detector, but is more sensitive to the electron dose and the convergence angle. In addition, the large pixel size of the EMPAD allows for less charge spreading to adjacent pixels where the MTF and the diffraction pattern will appear sharper at higher beam energies than the other competing detectors. Overall, to push the field of diffractive imaging, instead of designing a detector with more pixels, we should focus on faster acquisitions with the current detector design. From which, we could do time-resolved experiments with more details, precision and information than before.

In the second theme, we explore the applications of the EMPAD to imaging magnetic fields and ferroelectric properties. For magnetic imaging, current works on skyrmions with ptychography can push spatial resolution such that more sensitive magnetic fields can be detected at higher spatial resolution. In addition, tomographic studies of magnetic and electric fields can also help scientist reconstruct not only the structure but also the electromagnetic field of the sample in three dimensions. For new physics applications, ferroelectric materials are a good case study. Here, the intensity inside of the diffracted disks have been traditionally interpreted using Bloch waves in conjunction with the three-beam condition [83]. Now with the capability to extract more information from the sample using the EMPAD, a relation between the probability current flow and Bloch-wave conditions could be used to explain the effects of polarization, thus bridging the gap among the two fields for the ferroelectric theorists (enthusiasts) and diffraction aficionados. In addition, theory from HOLZ line breaking can lead us to interpret the polarization effects in the out of plane direction, this is interesting physics that can be explained further.

5.2 Future Works

The applications for the EMPAD can range from biology, material science, chemistry and physics. This dissertation is just a simple beginning to the impact of the EMPAD for the future of electron microscopy. For future work, I will talk about my own proposed work after graduating from Cornell.

I plan to work with Professor Pinshane Huang at the University of Illinois as part of Materials Science and Engineering, to develop new high-precision electron microscopy techniques on 2D materials enabled by the EMPAD. My work at the University of Illinois will have two main objectives: 1) To use 2D materials to demonstrate the new capabilities of the EMPAD to measure the structure and properties of materials at the atomic scale and 2) to develop new ways to extract and interpret the large datasets generated by the EMPAD using recent advances in data mining and machine learning.

2D nanoelectronic materials: The study of atomic-monolayer materials has been extremely popular within the last decade from the realization of semi-metal properties of graphene to the emergence of a family of two-dimensional (2D) with an expansive range of unique electrical properties. Here, heterojunctions designed from 2D semiconductors can mimic their three-dimensional (3D) counterparts to enable band engineering within the 2D plane to unveil new device physics and material science properties. However, subtle changes in 2D materials from charge density at atomically sharped p-n junctions, strain fields and dislocations are extremely important when tuning the electronic and mechanical properties to make actual devices.

As a postdoctoral researcher, I plan to use the EMPAD to provide insight by directly measuring the electromagnetic fields to recover charge densities at atomically sharp p-n junctions and investigate how band alignment is expected to change at the

heterojunction, where mapping charge density distributions can be used to localize and separate regions of electrons and holes. This fundamental understanding is extremely important when building electronic and optoelectronic devices and especially more important when tailoring these devices for future applications.

Computational and machine learning techniques for efficient interpretation of EMPAD data: Over the last decade, a revolution in electron microscopy hardware, including my work on the EMPAD, has resulted in a new era where electron microscopes can generate terabytes of data each day —data that encodes atomic-scale information on local structure, bonding, chemistry, as well as built-in electrical and magnetic fields in matter. In this new era of big data in electron microscopy, the next revolutions will be driven by adapting developments in image processing, data mining, neural networks, and machine learning to harness and interpret these new sources of data. By collecting the full scattering distribution at each scan position, the EMPAD can generate over a 150 gigabytes of data a day.

The large datasets from the EMPAD are computationally expensive, which can limit the effectiveness of sample interpretation and throughput of sample analysis. 2D materials make it easy to rapidly generate simulated datasets, compare them to real experimental data. Methods for processing these complex, correlated datasets such as multiplexed and 4D datasets, are an ideal knowledge base for developing new methods for extracting and analyzing atomic-scale electron microscopy data. Here, I plan to develop new material characterization techniques to extract real physical quantities

aided by machine learning where cluster analysis can help decipher new interesting physics.

As a scientist, my goal is to continue making scientific breakthroughs with breadth and with depth.

APPENDIX

A.1 Analytical Derivation of Center of Mass Signal and Resolution

To determine the accuracy of the magnetic field using differential phase contrasting imaging, one must calculate how the shift of the electron beam as it scatters through the sample is related to the noise. From [40, 103], a simple model is produced where the scattered electron is detected by a split detector. Here we derived analytical the dependence of the electron beam on two factors: 1) α, the semi-convergence angle of the electron beam (who has a dependence on brightness), and 2) N, the dose which tells you how many electrons are needed to such that the signal is adequately above the noise.

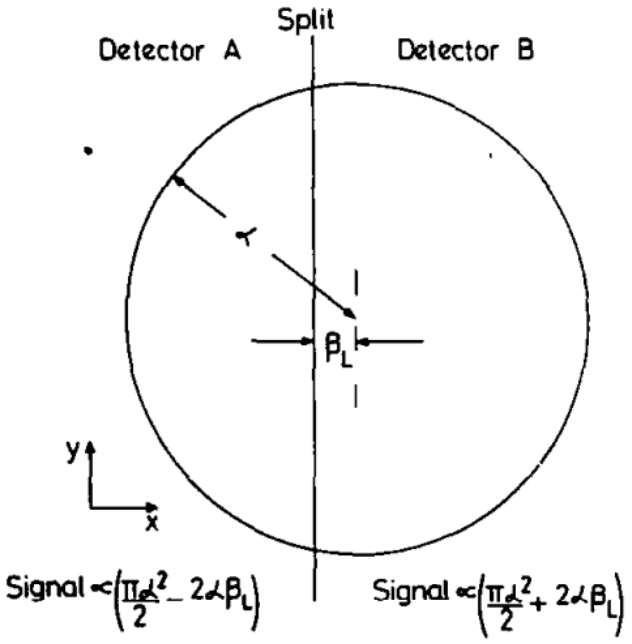

Figure A.1. Schematic of signal distribution given for a split circular detector from. Here, α is the semi-convergence angle and $\beta_L$the deflection from the local magnetic

field of the sample [40].

We can say that the signal S is the difference over the entire detector, which then becomes:

$$S = \frac{4\beta_L}{\pi\alpha} \tag{A.1}$$

where β_L corresponds to the deflection angle of the electron beam from the local magnetic field of the sample. Here, we observed that the dose, N, represents the total number of electrons:

$$N = {B\pi^2\alpha^2D^2\tau}/{4e} \tag{A.2}.$$

where B is the brightness of the electron gun, D is the beam diameter, τ is the time interval, and e is the electron charge. The signal with respect to the dose, N, then becomes $N_s = S * N$ and the noise in the detector is $N_n = \sqrt{N}$. Then we can set the signal to noise ratio as $s = S * \sqrt{N}$ from which we assume s = 1, then we can rewrite the equation such that we see the dependence of deflection β_L on:

$$\beta_L = {\pi\alpha}/{4\sqrt{N}} \tag{A.3}.$$

From this, we find that the minimum deflection angle β_L and essentially magnetic field depends on α is the semi-convergence angle and N the dose or the number of electrons.

If we want to get the minimum deflection β_L in terms $1/\sqrt{Hz}$, we can rewrite $\beta_t = \beta_L\sqrt{\tau}$. Here, we observed that there is a directly analytical dependence of the minimum deflection on only the semi-convergence angle and the dose, parameters that can be easily modified in the electron microscope and therefore a simpler methodology to obtain a sensitive magnetic field without electron microscopy jargon.

A.2 Methods for Characterization of Ferroelectric Polarization Vortices

Superlattice samples were imaged using both a 200 keV uncorrected FEI Tecnai F20 and a 60-300 keV probe-corrected FEI Titan Themis. The same EMPAD detector was used on both instruments.

A.2.1 Scanning Transmission Electron Microscopy (STEM)

Atomic resolution imaging was performed on the Titan instrument at 300 keV with a 29 mrad convergence angle. As a practical demonstration of dynamic range, Figure A.2 shows the diffraction patterns of $SrTiO_3$ recorded from 1ms, 10ms and 100 ms acquisitions with a ~1Å beam containing 100 pA probe current at 120 keV in Titan Themis. The high-angle scattering is detected with single electron sensitivity simultaneously with the unsaturated high-intensity central beam and crystallographic Bragg discs. The Kikuchi bands are detectable and HOLZ lines are visible at 1, 10 and 100ms.

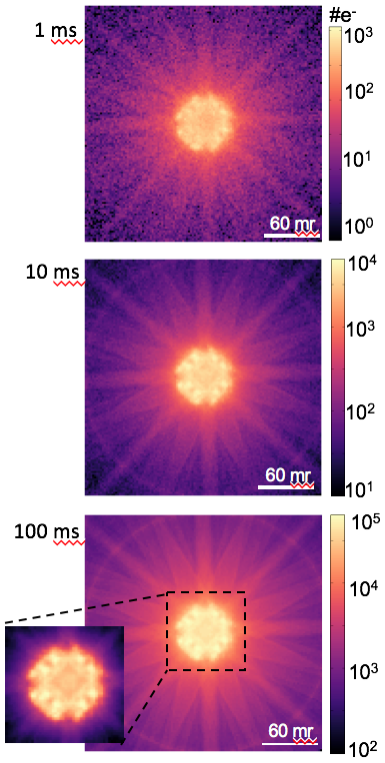

Figure A.2. Convergent Beam Electron Diffraction patterns recorded in 1,10 and 100 ms from [100] oriented $SrTiO_3$ using a 30 mrad convergence angle at 120 keV recorded with the EMPAD on a FEI Titan Themis.

There is more than sufficient information at 1 ms/frame to quantitatively recover all the elastic imaging modes simultaneously and on an absolute scale and a select set of useful atomic-resolution modes are show in Figure A.3, including the integrated center of mass image that measures the change in projected potential [52, 101], resolving the oxygen sublattice cleanly.These images are from an interface between $SrTiO_3$ and $PbTiO_3$ in a $(PbTiO_3)_{12}/(SrTiO_3)_{12}$ superlattice that show polarization vortices in the ferroelectric $PbTiO_3$ layers, similar to those reported in reference [77]. There is a portion of a vortex in top right hand corner of the images, but it is extremely

difficult to discern without further processing because the images are all dominated by the strong nuclear contrast. In other words, the electric fields from the nuclei and core electrons mask the macroscopic fields and structural modulations. This is especially the case for Figure A.3, which shows the net torque transfer from the sample to the electron beam. For a small beam placed exactly over an atom column, the torque transfer is zero as this closely approximates a central potential, which must conserve orbital angular momentum. Integrating over beam positions near the nucleus averages to almost zero but with large, noise sensitive cancellations.

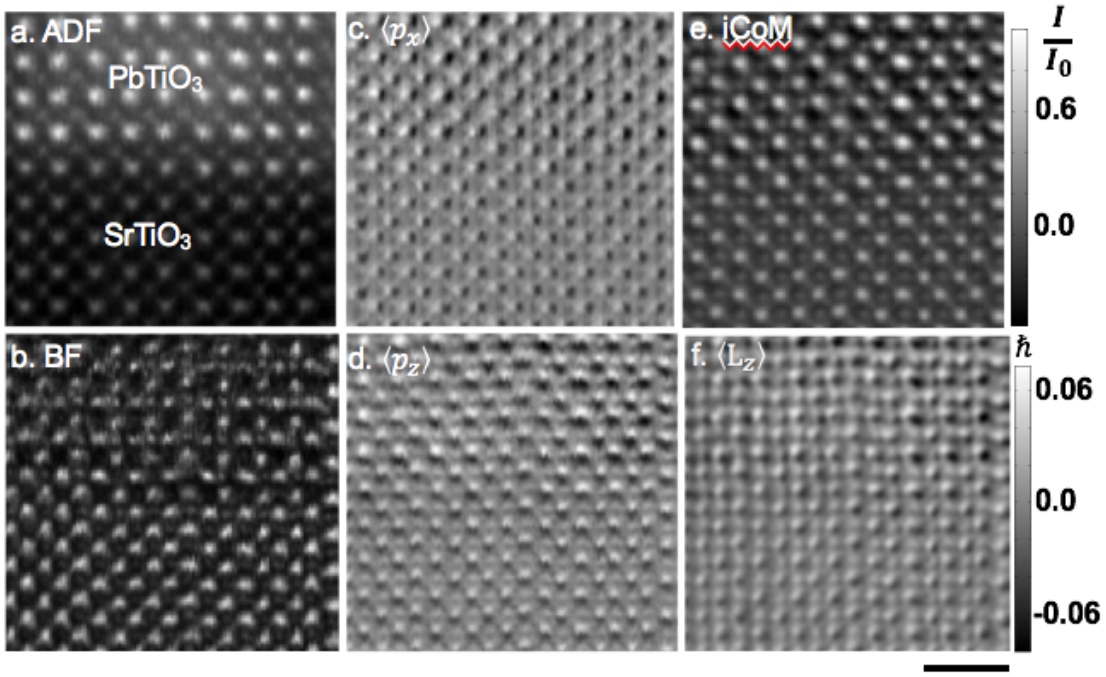

Figure A.2. Scanning the electron beam across a $PbTiO_3/SrTiO_3$ interface and recording CBED patterns, we extract the simultaneous (a) annular dark field (ADF), (b) bright field (BF), and center of mass components (c) $\langle p_x \rangle$ and (d) $\langle p_y \rangle$. The center of mass signals are proportional to the gradient of the projected potential, which is recovered by

integration. The resulting integrated center of mass (iCOM) image (e) shows both the light atoms (oxygen) and heavy atom columns (Pb, Sr, Ti-O). The transfer of torque image, $\langle \Gamma_z \rangle$, (f) reconstructed from this data set, is plotted as the change in orbital angular momentum with respect to the incident beam. There is a vortex core in upper right portion of the image, but it is hard to discern visually without quantitative processing, and the image contrast is dominated by the nuclear modulations. Black scale bar represents 1 nm for Figures A.2 (a-f).

It is easier to see the macroscopic modulations in the material by filtering out the atomic fields and work with the average or macroscopic quantities and fields, which we did by adjusting the convergence angle of the beam until the diffraction disks on EMPAD no longer touched each other. This corresponded to angles of 3.0 mrad at 200 keV and 1.76 and 1.4 at 300 keV.

For reasonably thin specimens where the strong phase approximation holds (Suppl. Equation S7), the probability current images can be further simplified as a convolution of the incident beam shape and the gradient of the sample potential $V(\vec{r}_p)$ [39]:

$$\langle \vec{p}(\vec{r}_p) \rangle = \hbar\sigma \left| \Psi_0(\vec{r}_p) \right|^2 \otimes \vec{\nabla} V(\vec{r}_p) \qquad (3).$$

From which we can now calculate, and measure the OAM, $\langle \boldsymbol{L} \rangle$. We note that $\langle \boldsymbol{L} \rangle$ $(= \langle \hat{\boldsymbol{r}} \times \hat{\boldsymbol{p}} \rangle)$ is proportional to the toroidal moment and order parameter $\boldsymbol{g} = \frac{1}{2} \int \boldsymbol{r} \times \boldsymbol{P}(\boldsymbol{r})\, d^3\boldsymbol{r}$, where $\boldsymbol{P}(\boldsymbol{r})$ is local dipole density[13], as $\boldsymbol{P}(\boldsymbol{r})$ is proportional to the $\langle \boldsymbol{p} \rangle$ constructed from Friedel pairs in thin samples. This can be seen numerically in Figure

2a vs b where the polarization field tracks the contrast in the probability current images $\langle p_x \rangle$ and $\langle p_z \rangle$.

The COM image formed from integrating over the entire diffraction pattern has the potential for contributions from tilt, electric field, changes in sample thickness and polarity. We can get a better idea of their possible influences by decomposing the potential of the crystal $V(\vec{r}) = \sum_{\vec{G}} U_{\vec{G}} \exp\left(i\phi_{\vec{G}}\right) e^{i(\vec{G}\cdot\vec{r})}$ in terms of its Fourier components (with amplitude $U_{\vec{G}}$ and phase $\phi_{\vec{G}}$) at reciprocal lattice vectors $\vec{G}$ and then using the linearity of equation (3) to form CoM images from individual diffracted beams $V_{\vec{G}}$. The CoM images $\langle \vec{p}_{000} \rangle$ using the central beam (Figure 4.3 a,b) show changes in the projected mean inner potential V_{000} from the thickness change at the surface, differences between Pb and Sr in the multilayers and small electric field variations inside the film. As the (000) beam lacks a Friedel pair, there is no polarity contribution. Inside the film, the $\langle \vec{p}_{000} \rangle$ image is relatively flat, suggesting little tilt variation.

To visualize the polarity changes in the sample, we form COM images (Figure 4.3 c, d) summed from the Friedel pairs in the $\{200\}$ beams, corresponding to the Ti-Pb planar spacings – key components in the ferroelectric distortions. For a Friedel pair of diffraction spots at $\vec{G}_1$ and $-\vec{G}_1$ (e.g. the Fourier coefficients of the potential V_{200} and $V_{\bar{2}00}$), the leading non-zero term in the strong phase approximation for the measured momentum transfer is given by supplementary equation S3.13 where the center of mass of Friedel pair is $\langle \vec{p}_{\{\vec{G}_1\}} \rangle \propto 2\vec{G}_1 \sum_{\vec{G}_2} U_{\vec{G}_1} U_{\vec{G}_2} U_{\vec{G}_1 - \vec{G}_2} \sin(\phi)$, and the three-phase invariant

is $\phi = \phi_{\vec{G}_1} - \phi_{\vec{G}_2} - \phi_{\vec{G}_1 - \vec{G}_2}$. $\mathrm{Sin}(\phi)$ is a useful metric for tracking the polarization order parameter along $\vec{G}_1$, and is zero for a non-polar structure and independent of the coordinate system chosen (see section A.3).

The strong contrast, when replotted as a vector map (Fig 4.4 b and 4.10) shows the polarization vortices clearly. The angular deflections from the internal electric fields seen in $\langle \vec{p}_{000} \rangle$ are small compared to the polarity contrast in the $\{200\}$ beams suggesting little need for correction.

For polarity measurements, we found it was critical to ensure the sample is oriented exactly down the zone axis, as crystal mis-tilts and bends will dominate image contrast when present [43]; therefore, checking polarity images against COM maps formed from the central beam and Kikuchi maps was important. The tilt contrast itself is easy to identify here as it derives from and has the same periodicity as the strain dechanneling contrast seen in the annular dark field (ADF) images.

Electron channeling plays an important role in the depth dependence of the probability current signal where the signal is not a simple projection through the sample. From multislice simulations, the signal from the strongly-scattering Pb columns comes mostly from the top half of the vortex (Figure 4.6), and is scattered away after that. The dechanneling in the two in-plane directions is quite similar as it is dominated by the atomic column more so than the small displacements, where so much of the thickness

variation can be compensated by comparing the relative intensities of the $\langle p_y \rangle$ and $\langle p_x \rangle$ components (Figure 4.7).

A.2.2 $PbTiO_3/SrTiO_3$ Growth

Pulsed Laser Deposition (PLD) was used to synthesize superlattice films of $PbTiO_3/SrTiO_3$. All films were grown on $SrRuO_3$-buffered (110) oriented $DyScO_3$ single crystalline substrate. Reflection High Energy Electron Diffraction (RHEED) was used to monitor the growth dynamics of $PbTiO_3$ and $SrTiO_3$. The growth conditions were carefully optimized to obtain layer-by-layer (Frank-van der Merwe) growth of $PbTiO_3$ and $SrTiO_3$, which was sustained for the entire growth of 100 nm thick superlattice film. For detailed account on growth conditions and optimization of other parameters, see Methods section of reference [77].

A.2.3 Density Functional Calculations of Superlattice Structure and Polarization, second principles simulations of $PbTiO_3/SrTiO_3$ superlattices

The interactions within the $PbTiO_3$ or $SrTiO_3$ layers were based on the previously introduced potentials for the bulk compounds, which give a qualitatively correct description of the lattice dynamical properties and structural phase transitions of both materials. For the interactions between ion pairs at the interface simple numerical averages were used. For the periodicities of the superlattices studied in this work, the main effects of the stacking are purely electrostatic. Those long-range dipole-dipole

interactions are governed by the Born effective charges of the bulk parent compounds and a bare electronic dielectric constant ε^{∞} that is taken as a weighted average of the first-principles results for bulk $PbTiO_3$ ($\varepsilon^{\infty,\,PTO} = 8.5$) and $SrTiO_3$ ($\varepsilon^{\infty,\,STO} = 6.2$) with weights reflecting the composition of the superlattice. In order to preserve the electrostatic interactions within each material as close as possible to the bulk parent compounds, we have rescaled the Born effective charge tensors of the inner atoms by $\sqrt{\varepsilon^{\infty}/\varepsilon^{\infty,ABO_3}}$ (where ABO_3 stands for $PbTiO_3$ or $SrTiO_3$ depending on the layer to which the atom belongs). In this way, the dipole-dipole interactions remain the same as in bulk even if we adopt a common value of ε^{∞} for the whole heterostructure. The Born tensors corresponding to the atoms at the interfaces were left untouched.

We assume in-plane lattice constants of $a = b = 3.901$ Å and $\gamma = 90°$. To counteract the underestimate of the lattice constant due to the well-known overbinding error of the local density approximation, which is the first-principles theory used to compute the parameters of our model, an external expansive hydrostatic pressure of -11.2 GPa is imposed. These approximations and adjustments allow us to construct models for superlattices of arbitrary n stacking. For computational feasibility, we have focused on a simulation supercell made from a periodic repetition of $2n \times n \times 2n$ elemental perovskite unit cells, sufficiently large to simulate domains in the $n = 10$ superlattice. We solved the models by running Monte Carlo simulations typically comprising 10,000 thermalization sweeps followed by 40,000 sweeps to compute thermal averages. We ran Monte Carlo simulated annealing down to very low temperatures to perform structural relaxations and find the ground state or metastable solutions.

A.3 Measuring Polarity and Torque Transfer from Probability Current Images

Here we derive the central relationship that connects the measured probability current flow of an electron beam with wave function $\Psi(\vec{r},\ \vec{r}_p)$ centered about probe position $\vec{r}_p$ to the torque transfer using the strong phase approximation. The starting point is the measurement of the center of mass image, $\langle\vec{p}\rangle$ formed by scanning the probe position $\vec{r}_p$ and measuring the angular distribution of scattered electron beam at each probe position, $\left|\Psi(\vec{k},\vec{r}_p)\right|^2$, where $\vec{k}$ and $\vec{r}$ are the conjugate variables in the back focal plane and image plane respectively [36, 41]. A center of mass (COM) image has each pixel value equal to the centroid of the associated diffraction pattern where

$$\langle\vec{p}(\vec{r}_p)\rangle = \int \hbar\vec{k}\left|\Psi(\vec{k},\vec{r}_p)\right|^2 d\vec{k} \qquad \text{(S1)}$$

which follows from the definition of $\langle\vec{p}\rangle$ written out in a momentum basis [36, 41]. For a thin slice, Ehrenfest's theorem connects $\langle\vec{p}\rangle$ to the gradient of the projected potential [36, 41].

Expanding $\langle\vec{p}\rangle = \langle\Psi|\hat{p}|\Psi\rangle$ in a position basis and using $\hat{p} = -i\hbar\vec{\nabla}$ we obtain

$$\langle\vec{p}(\vec{r}_p)\rangle = -\hbar i\int \Psi^*(\vec{r},\vec{r}_p)\vec{\nabla}\Psi(\vec{r},\vec{r}_p)d\vec{r} \qquad \text{(S2)}$$

Equation (S3) is an exact relationship for any exit wave from the sample. $\langle\vec{p}\rangle$ differs from the expectation value of probability current flow $\langle\vec{j}\rangle$ by a factor of twice the electron's mass, m [36, 41]:

$$\langle \vec{p}(\vec{r}_p) \rangle = \frac{\hbar}{2i} \int \Psi^*(\vec{r}, \vec{r}_p) \vec{\nabla} \Psi(\vec{r}, \vec{r}_p) - \Psi(\vec{r}, \vec{r}_p) \vec{\nabla} \Psi^*(\vec{r}, \vec{r}_p) \, d\vec{r}$$

$$= 2m\langle \vec{j} \rangle \qquad \text{(S3)}$$

In section 1 we review the already-derived connection between the center of mass images and the gradient of the potential to establish a consistent notation. In section 2 we derive the new relationship between torque transfer and the center of mass images. In section 3, we show how polarity is encoded in the probability current flow to a pair of conjugate diffracted beams.

A.3.1 Relation between Center of Mass and Potential Gradient Images

To connect $\langle \vec{p} \rangle$ of the exit wave to the scattering potential, we next make the strong phase approximation which should hold so long as the probe amplitude does not change dramatically in sample. In the strong phase approximation, the exit wavefunction is just a product of the initial wavefunction, Ψ_0, and a phase term from the sample potential, $V(\vec{r})$.

$$\Psi(\vec{r}, \vec{r}_p) = exp\big(i\sigma V(\vec{r})\big)\Psi_0(\vec{r} - \vec{r}_p), \qquad \text{(S4)}$$

where σ is the usual interaction parameter [95]. Substituting eqn. (S4) into eqn. (S2) gives:

$$\langle \vec{p}(\vec{r}_p) \rangle =$$

$$-i\hbar \int \left[i\sigma\vec{\nabla}V(\vec{r})\Psi_0(\vec{r}-\vec{r}_p) + \vec{\nabla}\Psi_0(\vec{r}-\vec{r}_p)\right] \exp(i\sigma V(\vec{r}))\exp(-i\sigma V(\vec{r}))\Psi_0^*(\vec{r}-\vec{r}_p)\, d\vec{r}$$

(S5)

$$\langle\vec{p}(\vec{r}_p)\rangle = -i\hbar \int \Psi_0^*(\vec{r}-\vec{r}_p)\vec{\nabla}\Psi_0(\vec{r}-\vec{r}_p)d\vec{r} + \hbar\sigma \int \vec{\nabla}V(\vec{r})\left|\Psi_0(\vec{r}-\vec{r}_p)\right|^2 d\vec{r}$$

If the beam is symmetric [101], then the first term goes to zero and the second term can be written as a convolution:

$$\langle\vec{p}(\vec{r}_p)\rangle = \hbar\sigma\left|\Psi_0(\vec{r}_p)\right|^2 \otimes \vec{\nabla}V(\vec{r}_p) \qquad \text{(S7)}$$

which establishes the conditions under which the center of mass image is a convolution of the potential gradient and the probe. If the beam is not symmetric, then the first term, which depends only on the incident beam, provides a constant offset uniform background which can be subtracted off, and the second term changes equation S7 to a cross correlation [83].

A.3.2 Calculating Torque from COM Images

The torque operator for an electron in the beam can be

$$\hat{\Gamma} = \hat{\vec{r}} \times -\vec{\nabla}\hat{V} \qquad \text{(S8)}$$

We can calculate its expectation value by expanding in the position basis.

$$\langle\hat{\Gamma}\rangle = \langle\Psi|\hat{\Gamma}|\Psi\rangle \qquad \text{(S9)}$$

and the z-component is

$$\langle\hat{\Gamma}_z\rangle = \begin{array}{l} \int\langle\Psi|\vec{r}''\rangle\langle\vec{r}''|\hat{x}|\vec{r}'\rangle\left\langle\vec{r}'\left|-\frac{\partial\hat{V}}{\partial y}\right|\vec{r}\right\rangle\langle\vec{r}|\Psi\rangle d\vec{r}d\vec{r}'d\vec{r}'' \\ +\int\langle\Psi|\vec{r}''\rangle\langle\vec{r}''|\hat{y}|\vec{r}'\rangle\left\langle\vec{r}'\left|\frac{\partial\hat{V}}{\partial x}\right|\vec{r}\right\rangle\langle\vec{r}|\Psi\rangle d\vec{r}d\vec{r}'d\vec{r}'' \end{array} \quad \text{(S10)}$$

Since the position basis are eigenkets of the position and potential operators, we can expand the integral

$$\langle\hat{\Gamma}_z\rangle = \int \square\frac{-\partial V}{\partial y}(\vec{r}')\Psi^*(\vec{r}'')\Psi(\vec{r})\delta(\vec{r}''-\vec{r}')\delta(\vec{r}'-\vec{r^{\rightarrow}})+\cdots \text{(S11)}$$

We only show the calculation for one of the terms in the sum. Both are similar, and combining gives

$$\langle\hat{\Gamma}_z\rangle = \int x\frac{-\partial V}{\partial y}|\Psi(\vec{r})|^2 d\vec{r} + \int y\frac{\partial V}{\partial x}|\Psi(\vec{r})|^2 d\vec{r} \qquad \text{(S12)}$$

This is the general formula where $\Psi(\vec{r})$ is the exit wavefunction. In the context of a scanning beam, we can write our exit wavefunction as the probe shifted to the relevant scan point $\Psi(\vec{r}-\vec{r}_p)$. We also want to measure with respect to $\vec{r}_p$ as the origin. Therefore, we re-write for the torque in the z direction as

$$\Gamma_z(\vec{r}_p) = \int\left[(\vec{r}-\vec{r}_p)\times(-\vec{\nabla}V(\vec{r}))\right]_z\left|\Psi(\vec{r}-\vec{r}_p)\right|^2 d\vec{r} \qquad \text{(S13)}$$

where $V(\vec{r})$ is the potential of the sample.

We take advantage of the symmetry of the probe to re-write this equation to look like a convolution (for asymmetric probes this will remain a cross-correlation, a result which will carry through without loss of generality):

$$\Gamma_z(\vec{r}_p) = \int \left[(\vec{r}_p - \vec{r}) \times -\vec{\nabla} V(\vec{r})\right]_z \left|\Psi(\vec{r}_p - \vec{r})\right|^2 d\vec{r} \qquad \text{(S14)}$$

This form is convenient because convolutions in real space are multiplications in Fourier space. Taking a Fourier transform gives

$$\mathcal{F}[\Gamma_z(\vec{r})] = -\mathcal{F}\left[\frac{-\partial V}{\partial y}(\vec{r})\right] \mathcal{F}[x|\Psi(\vec{r})|^2] + \mathcal{F}\left[\frac{-\partial V}{\partial x}(\vec{r})\right] \mathcal{F}[y|\Psi(\vec{r})|^2] \qquad \text{(S15)}$$

At this point, we need to find the gradient of the potential. As shown in **equation S7**, that by using the strong phase approximation, our COM images are related to the gradient of the potential by a convolution. For example, the COM in the x direction is with Ψ_0 being the incident wavefunction given by

$$\langle p_x(\vec{r}_p)\rangle = \hbar\sigma \left|\Psi_0(\vec{r}_p)\right|^2 \otimes \frac{\partial V(\vec{r}_p)}{\partial x} \qquad \text{(S16)}$$

Taking a Fourier transform gives

$$\mathcal{F}\left[\langle p_x(\vec{r}_p)\rangle\right] = \hbar\sigma\, \mathcal{F}[|\Psi_0(\vec{r})|^2]\, \mathcal{F}\left[\frac{\partial V}{\partial x}(\vec{r})\right] \qquad \text{(S17)}$$

We can now write Eq. (S15) as

$$\Gamma_z(\vec{r}) = \mathcal{F}^{-1}\left\{\frac{-\mathcal{F}[\langle p_y(\vec{r})\rangle]\mathcal{F}[x|\Psi_0(\vec{r})|^2] + \mathcal{F}[\langle p_x(\vec{r})\rangle]\mathcal{F}[y|\Psi_0(\vec{r})|^2]}{\hbar\sigma\mathcal{F}[|\Psi_0(\vec{r})|^2]}\right\} \qquad \text{(S18)}$$

This is the desired result, describing the torque in terms of only the experimentally-measured quantities $\langle p_x(\vec{r}_p)\rangle$, $\langle p_y(\vec{r}_p)\rangle$, $|\Psi_0(\vec{r})|^2$. A key observation here is that in the strong phase approximation (equation S4), $|\Psi(\vec{r})|^2 = |\Psi_0(\vec{r})|^2$and the incident beam shape can be measured directly at medium resolution, or with the aberration-correction software at high-resolution. At medium spatial resolution (non-overlapping disks), multislice simulations indicate this approximation is robust for sample thicknesses up

to 20 nm at 300 keV.

Now $\mathcal{F}[|\Psi_0(\vec{r})|^2]$ is peaked at zero frequency and is zero at frequencies with k-vectors magnitudes larger than the diameter of the probe-forming aperture. To avoid dividing by zero or by values arbitrarily close to zero in $\mathcal{F}[|\Psi_0(\vec{r})|^2]$, we pass this through a low-pass filter to suppress the high frequency noise beyond the aperture cutoff. Equation S18 can be trivially modified to incorporate an optimal Wiener filter, recognizing that eqn. (S18) is essentially deconvolving the effect of the probe contrast transfer function (CTF) from the torque measurement. Omitting the division by the probe CTF leaves us with the torque measurement blurred out to probe resolution. This may be preferable for noisy data or thick samples where the strong phase approximation may no longer hold.

A.3.3 Measuring Polarity from the COM image in the Strong Phase Approximation

Polarity is usually calculated within a Bloch-wave formalism [6] to account for the multiple scattering of the electron beam through the sample. While there are analytic results for special cases, that approach is more useful computationally than for insight. Here we consider a thin sample described by the strong phase approximation that provides a simpler result, useful for understanding the contributions to the polarity measurement, while still retaining the key symmetries of the more complicated theory.

Starting with equation (S4), the diffraction pattern expanded out to third order is:

$$\left|\Psi\left(\vec{\mathrm{k}},\vec{\mathrm{r}}_{\mathrm{p}}\right)\right|^2 = \begin{matrix} \left|\Psi_0\left(\vec{\mathrm{k}}\right)\right|^2 + \frac{\sigma}{\pi}\mathrm{Im}\left\{\Psi_0\left(\vec{\mathrm{k}},\vec{\mathrm{r}}_{\mathrm{p}}\right)\left[\Psi_0^*\left(\vec{\mathrm{k}},\vec{\mathrm{r}}_{\mathrm{p}}\right)\otimes \mathrm{V}^*\left(\vec{\mathrm{k}}\right)\right]\right\} \\ + \frac{\sigma^2}{4\pi^2}\left\{\left|\Psi_0\left(\vec{\mathrm{k}},\vec{\mathrm{r}}_{\mathrm{p}}\right)\otimes \mathrm{V}\left(\vec{\mathrm{k}}\right)\right|^2 - \mathrm{Re}\left[\Psi_0\left(\vec{\mathrm{k}},\vec{\mathrm{r}}_{\mathrm{p}}\right)\left(\Psi_0^*\left(\vec{\mathrm{k}},\vec{\mathrm{r}}_{\mathrm{p}}\right)\otimes \mathrm{V}_2^*\left(\vec{\mathrm{k}}\right)\right)\right]\right\} \\ + \frac{\sigma^3}{8\pi^3}\left\{\begin{matrix}\mathrm{Im}\left[\left(\Psi_0\left(\vec{\mathrm{k}},\vec{\mathrm{r}}_{\mathrm{p}}\right)\otimes \mathrm{V}\left(\vec{\mathrm{k}}\right)\right)\left(\Psi_0^*\left(\vec{\mathrm{k}},\vec{\mathrm{r}}_{\mathrm{p}}\right)\otimes \mathrm{V}_2^*\left(\vec{\mathrm{k}}\right)\right)\right] \\ -\frac{1}{3}\mathrm{Im}\left[\Psi_0\left(\vec{\mathrm{k}},\vec{\mathrm{r}}_{\mathrm{p}}\right)\left(\Psi_0^*\left(\vec{\mathrm{k}},\vec{\mathrm{r}}_{\mathrm{p}}\right)\otimes \mathrm{V}_3^*\left(\vec{\mathrm{k}}\right)\right)\right]\end{matrix}\right\} \\ + \cdots \end{matrix}, \quad (S3.1)$$

where

$$\Psi_0\left(\vec{k},\vec{r}_p\right) = \Psi_0\left(\vec{k}\right)\exp\left(-i\vec{k}\cdot\vec{r}_p\right), \quad (S3.2)$$

$$V_2\left(\vec{k}\right) = V\left(\vec{k}\right)\otimes V\left(\vec{k}\right), \quad (S3.3)$$

$$V_3\left(\vec{k}\right) = V\left(\vec{k}\right)\otimes V\left(\vec{k}\right)\otimes V\left(\vec{k}\right). \quad (S3.4)$$

The only term outside the bright disk field that is asymmetric and therefore contributes to the Center-of-Mass signal from the diffracted beams is the third order term

$$\mathrm{Im}\left[\left(\Psi_0\left(\vec{\mathrm{k}},\vec{\mathrm{r}}_{\mathrm{p}}\right)\otimes \mathrm{V}\left(\vec{\mathrm{k}}\right)\right)\left(\Psi_0^*\left(\vec{\mathrm{k}},\vec{\mathrm{r}}_{\mathrm{p}}\right)\otimes \mathrm{V}_2^*\left(\vec{\mathrm{k}}\right)\right)\right]. \quad (S3.5)$$

We assume our sample is a crystal and can therefore write our crystal potential in reciprocal space as

$$V\left(\vec{k}\right) = \mathcal{F}[V(\vec{r})] = \sum_{\vec{G}} U_{\vec{G}}\exp\left(i\phi_{\vec{G}}\right)\delta\left(\vec{k}-\vec{G}\right), \quad (S3.6)$$

where $\vec{G} = h\vec{g}_1 + k\vec{g}_2 + l\vec{g}_3$ is a reciprocal lattice vector and $U_{\vec{G}}$ and $\phi_{\vec{G}}$ are real. Substituting $V\left(\vec{k}\right)$ from equation (S3.6) into equation (S3.5) introduces 3 sums over reciprocal lattice vectors labelled $\vec{G}_1, \vec{G}_2, \vec{G}_3$, and after some algebra, equation (S3.5) becomes

$$\sum_{\vec{G}_1,\vec{G}_2,\vec{G}_3} \Psi_0(\vec{k}-\vec{G}_1)\Psi_0^*(\vec{k}-\vec{G}_2-\vec{G}_3)U_{\vec{G}_1}U_{\vec{G}_2}U_{\vec{G}_3}\sin\left(\phi_{\vec{G}_1}-\phi_{\vec{G}_2}-\phi_{\vec{G}_3}\right). \quad (S3.7)$$

The phase portion in equation (S3.7) is recognized as the three-phase invariant of crystallography:

$$\phi = \phi_{\vec{G}_1}-\phi_{\vec{G}_2}-\phi_{\vec{G}_1-\vec{G}_2}. \quad (S3.8)$$

which is invariant under a change of origin in real space: A shift in the origin by $\vec{r}_0$ leads to a phase shift $\phi'_{\vec{G}} = \phi_{\vec{G}} + \vec{G}\cdot\vec{r}_0$, but as the vectors $\vec{G}_1-\vec{G}_2-\vec{G}_1+\vec{G}_2=0$, the offset $\left(\vec{G}_1-\vec{G}_2-\vec{G}_1+\vec{G}_2\right)\cdot\vec{r}_0=0$ as well, thus there is no phase shift when choosing a new origin, making $\sin(\phi)$ a good metric for tracking components of the polar order parameter.

A.3.3.1 Polarity from the Center of Mass of Conjugate Diffraction Spots

Polarity can be sensed most simply through the use of Friedel pairs at $\vec{G}_1$ and $-\vec{G}_1$. Focusing on the diffraction spot centered around $\vec{G}_1$, we remove the $\vec{G}_1$ summation from equation (S3.7), and similarly for $-\vec{G}_1$. The probability current flow given by the CoM measurement will then become the sum of the first moments of the $\vec{G}_1$ and $-\vec{G}_1$ spots:

$$\begin{aligned}&\int \vec{k}\sum_{\vec{G}_2}\left|\Psi_0(\vec{k}-\vec{G}_1)\right|^2 U_{\vec{G}_1}U_{\vec{G}_2}U_{\vec{G}_1-\vec{G}_2}\sin\left(\phi_{\vec{G}_1}-\phi_{\vec{G}_2}-\phi_{\vec{G}_1-\vec{G}_2}\right)d\vec{k}\\ &+\int \vec{k}\sum_{\vec{G}_3}\left|\Psi_0(\vec{k}+\vec{G}_1)\right|^2 U_{-\vec{G}_1}U_{\vec{G}_3}U_{\vec{G}_1-\vec{G}_3}\sin\left(\phi_{-\vec{G}_1}-\phi_{\vec{G}_3}-\phi_{\vec{G}_1-\vec{G}_3}\right)d\vec{k}\end{aligned}, \quad (S3.9)$$

where we have separated the integral for later convenience. We can make a variable substitution for the integration variables $\vec{k}$ so that they are centered around the diffraction spot:

$$\begin{aligned}&\sum_{\vec{G}_2} U_{\vec{G}_1}\square_{\vec{G}_2}U_{\vec{G}_1-\vec{G}_2}\sin\left(\phi_{\vec{G}_1}-\phi_{\vec{G}_2}-\phi_{\vec{G}_1-\vec{G}_2}\right)\int\left(\vec{k}+\vec{G}_1\right)\left|\Psi_0\left(\vec{k}\right)\right|^2 d\vec{k}\\+&\sum_{\vec{G}_3} U_{-\vec{G}_1}U_{\vec{G}_3}U_{\vec{G}_1-\vec{G}_3}\sin\left(\phi_{-\vec{G}_1}-\phi_{\vec{G}_3}-\phi_{\vec{G}_1-\vec{G}_3}\right)\int\left(\vec{k}-\vec{G}_1\right)\left|\Psi_0\left(\vec{k}\right)\right|^2 d\vec{k}\end{aligned}. \quad (S3.10)$$

The first part of each integral $\int \vec{k}\left|\Psi_0\left(\vec{k}\right)\right|^2 d\vec{k}$ is just the first moment of the un-scattered bright-field disk, which is zero for a non-aberrated or symmetric incident beam. The second part is just the total intensity of the beam I_0 times the reciprocal lattice vector. This simplifies the expression to

$$\begin{aligned}&\vec{G}_1 I_0\sum_{\vec{G}_2} U_{\vec{G}_1}U_{\vec{G}_2}U_{\vec{G}_1-\vec{G}_2}\sin\left(\phi_{\vec{G}_1}-\phi_{\vec{G}_2}-\phi_{\vec{G}_1-\vec{G}_2}\right)\\-&\vec{G}_1 I_0\sum_{\vec{G}_3} U_{-\vec{G}_1}U_{\vec{G}_3}U_{\vec{G}_1-\vec{G}_3}\sin\left(\phi_{-\vec{G}_1}-\phi_{\vec{G}_3}-\phi_{\vec{G}_1-\vec{G}_3}\right)\end{aligned}. \quad (S3.11)$$

We can re-index $\vec{G}_3 = -\vec{G}_2$ without changing the second summation:

$$\vec{G}_1 I_0\sum_{\vec{G}_2}\begin{aligned}&U_{\vec{G}_1}U_{\vec{G}_2}U_{\vec{G}_1-\vec{G}_2}\sin\left(\phi_{\vec{G}_1}-\phi_{\vec{G}_2}-\phi_{\vec{G}_1-\vec{G}_2}\right)\\-&U_{-\vec{G}_1}U_{-\vec{G}_2}U_{-\vec{G}_1+\vec{G}_2}\sin\left(\phi_{-\vec{G}_1}-\phi_{-\vec{G}_2}-\phi_{-\vec{G}_1+\vec{G}_2}\right)\end{aligned}. \quad (S3.12)$$

For a real potential $V(\vec{r})$, $V^*\left(\vec{k}\right) = V\left(-\vec{k}\right)$. This means $U_{\vec{G}} = U_{-\vec{G}}$ and $\phi_{\vec{G}} = -\phi_{-\vec{G}}$ which gives our final expression for the Center of mass of the Friedel pair:

$$\langle\vec{p}_{\{\vec{G}_1\}}\rangle = \left(\frac{\hbar\sigma^3}{8\pi^3}\right)2\vec{G}_1 I_0\sum_{\vec{G}_2} U_{\vec{G}_1}U_{\vec{G}_2}U_{\vec{G}_1-\vec{G}_2}\sin(\phi) \quad (S3.13)$$

where three-phase invariant $\phi = \phi_{\vec{G}_1} - \phi_{\vec{G}_2} - \phi_{\vec{G}_1-\vec{G}_2}$ as before. However, if the crystal is also centrosymmetric, i.e. $V(\vec{r}) = V(-\vec{r})$, then the Fourier transform is also pure real, so all $\phi_{\vec{G}} = 0$ which means equation (S3.13) simplifies to 0 for non-polar materials. This result remains 0 even under a shift in origin that breaks the even symmetry of the crystal potential $V(\vec{r})$ thanks to the three-phase invariant. More generally, as $\sin(\phi)$ is independent of the choice of origin in real space, it can be used as a good order parameter for describing the component of the polarity along $\vec{G}_1$.

Finally, the Fourier coefficients of the potential, $U_{\vec{G}}$, are sensitive to both the nuclear and electronic contributions of the total potential for electron scattering. In other words the measured dipole density probed is net/total dipole density.

A.3.4 Fourier Convention

Fourier Transform convention:

$$F(\vec{k}) = \frac{1}{2\pi}\int f(\vec{r})exp(-i\vec{k}\cdot\vec{r})d\vec{r} \quad \text{(A1)}$$

$$f(\vec{r}) = \frac{1}{2\pi}\int F(\vec{k})exp(i\vec{k}\cdot\vec{r})d\vec{k} \quad \text{(A2)}$$

When using this convention, we get these properties:

$$\mathcal{F}[A(\vec{r})B(\vec{r})] = \frac{1}{2\pi}A(\vec{k}) \otimes B(\vec{k}) \quad \text{(A3)}$$

$$\mathcal{F}[A(\vec{r}) \otimes B(\vec{r})] = 2\pi A(\vec{k})B(\vec{k}) \quad \text{(A4)}$$

$$\mathcal{F}\left[\frac{\partial^n}{\partial x_i^n} A(\vec{r})\right] = (ik_i)^n A(\vec{k}) \qquad \text{(A5)}$$

where $\otimes$ represents the convolution operator.

BIBLIOGRAPHY

[1] Ryll, H., Simson, M., Hartmann, R., Holl, P., Huth, M. , Ihle, S., Kondo, Y., Kotula, P., Liebel, A., Müller-Caspary, K., Rosenauer, A., Sagawa, R, Schmidt, J., Soltau H., and Strüder L. (2016). A pnCCD-based, fast direct single electron imaging camera for TEM and STEM. Journal of Instrumentation **11**, 1-18.

[2] McMullan, G., Faruqi, A.R., Clare, D. and Henderson, R. (2014). Comparison of optimal performance at 300 keV of three direct electron detectors for use in low dose electron microscopy. Ultramicroscopy **147**, 156-163.

[3] Mir, J.A., Plackett, R., Shipsey, I., and dos Santos, J.M.F., Using the Medipix3 detector for direct electron imaging in the range 60 keV to 200 keV in electron microscopy (2017). Journal of Instrumentation, **12**, 1-8.

[4] M. W. Tate, P. Purohit, D. Chamberlain, K. X. Nguyen, R. Hovden, C. S. Chang, P. Deb, E. Turgut, J. T. Heron, D. G. Schlom, D. C. Ralph, G. D. Fuchs, K. S. Shanks, H. T. Philipp, D. A. Muller and S. M. Gruner, Microsc Microanal **22** (1), 237-249 (2016).

[5] Zuo, J.M. (2000). Electron detection characteristics of a slow-scan CCD camera, imaging plates and film, and electron image restoration. Microscopy Research and Technique **49**(3), 245-268.

[6] Jin, L., Milazzo, A.C., Kleinfelder, S., Li, S.D., Leblanc, P., Duttweiler, F., Bouwer, J.C., Peltier, S.T., Ellisman, M.H. & Xuong, N.H. (2008). Applications of direct detection device in transmission electron microscopy. Journal of Structural Biology **161**(3), 352-358.

[7] Boyle, W.S. & Smith, G.E. (1970). Charge Coupled Semiconductor Devices. Bell System Technical Journal **49**(4), 587.

[8] Fan, G.Y. & Ellisman, M.H. (2000). Digital imaging in transmission electron microscopy. Journal of Microscopy-Oxford **200**, 1-13.

[9] Meyer, R.R. & Kirkland, A. (1998). The effects of electron and photon scattering on signal and noise transfer properties of scintillators in CCD cameras used for electron detection. Ultramicroscopy **75**(1), 23-33.

[10] Jones, L., Yang, H., MacArthur, K. E., Ryll, H., Simson, M., Soltau, H., Kondo, Y., Sagawa, R., Banba, H., and Nellist, P.D. (2015). Opportunities in Angularly Resolved Dark-Field STEM using Pixelated Detectors. Microsc. Microanal, **21** (Supp 3), 2411 – 2412.

[11] Caswell, T.A., Ercius, P., Tate, M.W., Ercan, A., Gruner, S.M. & Muller, D.A. (2009). A high-speed area detector for novel imaging techniques in a scanning transmission electron microscope. Ultramicroscopy **109**(4), 304-311.

[12] Battaglia, M., Contarato, D., Denes, P., Doering, D., Giubilato, P., Kim, T.S., Mattiazzo, S., Radmilovic, V. & Zalusky, S. (2009). A rad-hard CMOS active pixel sensor for electron microscopy. Nuclear Instruments and Methods in Physics Research Section A: Accelerators, Spectrometers, Detectors and Associated Equipment **598**(2), 642-649.

[13] Fan, G.Y., Datte, P., Beuville, E., Beche, J.F., Millaud, J., Downing, K.H., Burkard, F.T., Ellisman, M.H. & Xuong, N.H. (1998). ASIC-based event-driven 2D digital electron counter for TEM imaging. Ultramicroscopy **70**(3), 107-113.

[14] Faruqi, A.R., Henderson, R. & Tlustos, L. (2005). Noiseless direct detection of

electrons in Medipix2 for electron microscopy. Nuclear Instruments & Methods in Physics Research Section a-Accelerators Spectrometers Detectors and Associated Equipment **546**(1-2), 160-163.

[15] Faruqi, A.R., Cattermole, D.M., Henderson, R., Mikulec, B. & Raeburn, C. (2003). Evaluation of a hybrid pixel detector for electron microscopy. Ultramicroscopy **94**(3-4), 263-276.

[16] McGrouther, D., Krajnak, M., MacLaren, I., Maneuski, D., O'Shea, V. & Nellist, P.D. (2015). Use of a hybrid silicon pixel (Medipix) detector as a STEM detector. Microscopy and Microanalysis **21**(Supplement S3), 1595-1596.

[17] Milazzo, A.-C., Leblanc, P., Duttweiler, F., Jin, L., Bouwer, J.C., Peltier, S., Ellisman, M., Bieser, F., Matis, H.S., Wieman, H., Denes, P., Kleinfelder, S. & Xuong, N.-H. (2005). Active pixel sensor array as a detector for electron microscopy. Ultramicroscopy **104** (2), 152-159.

[18] Ballabriga R, Campbell M., Heijne E., Llopart X., Tlustos L., and Wong W. (2011). Medipix3: A 64 k pixel detector readout chip working in single photon counting mode with improved spectrometric performance. Nuclear Instruments and Methods in Physics Research Section A: Accelerators, Spectrometers, Detectors and Associated Equipment, **633** (Suppl. 1), S15-S18.

[19] Frojdh, E., R. Ballabriga, M. Campbell, M. Fiederle, E. Hamann, T. Koenig, X. Llopart, D. D. P. Magalhaes, and M. Zuber (2014). Count Rate Linearity and Spectral Response of the Medipix 3RX Chip Coupled to a 300μm Silicon Sensor under High Flux Conditions. Journal of Instrumentation **9**, C04028.

[20] Yang, H., Pennycook, T.J. & Nellist, P.D. (2015). Efficient phase contrast

imaging in STEM using a pixelated detector. Part II: Optimisation of imaging conditions. Ultramicroscopy **151**, 232-239.

[21] Thompson, R.E., Larson, D.R. & Webb, W.W. (2002). Precise nanometer localization analysis for individual fluorescent probes. Biophysical Journal **82**(5), 2775-2783.

[22] Chapman, J.N. (1984). The Investigation Of Magnetic Domain-Structures In Thin Foils By Electron-Microscopy. Journal of Physics D-Applied Physics **17**(4), 623-647.

[23] Cowley, J.M. (1993). Configured detectors for STEM imaging of thin specimens. Ultramicroscopy **49**(1–4), 4-13.

[24] Kimoto, K. & Ishizuka, K. (2011). Spatially resolved diffractometry with atomic-column resolution. Ultramicroscopy **111**(8), 1111-1116.

[25] Ozdol, V.B., Gammer, C., Jin, X.G., Ercius, P., Ophus, C., Ciston, J. & Minor, A.M. (2015). Strain mapping at nanometer resolution using advanced nano-beam electron diffraction. Applied Physics Letters **106**(25).

[26] Zaluzec, N.J. (2002). Quantitative Measurements Of Magnetic Vortices Using Position Resolved Diffraction In Lorentz STEM. Microscopy and Microanalysis **8**(Supplement S02), 376-377.

[27] Nellist, P.D., McCallum, B.C., Rodenburg, J.M. (1995). Resolution beyond the information limit in transmission electron microscopy. Nature, **374**, 630 – 632.

[28] Pennycook, T.J., Lupini, A.R., Yang, H., Murfitt, M.F., Jones, L. & Nellist, P.D. (2015). Efficient phase contrast imaging in STEM using a pixelated detector. Part 1: Experimental demonstration at atomic resolution. Ultramicroscopy **151**, 160-167.

[29] Angello, A.G., Augustine, F., Ercan, A., Gruner, S., Hamlin, R., Hontz, T., Renzi, M., Schuette, D., Tate, M., Vernon, W. (2004). Development of a mixed-mode pixel array detector for macromolecular crystallography. IEEE Nucl. Sci. Symposium **7**, 4667-4671.

[30] Schuette, D.R. (2008). A mixed analog and digital pixel array detector fro synchrotron x-ray imaging. Ph.D. thesis, Cornell University, Ithaca, NY USA. **Ph.D.**

[31] Tate, M.W., Chamberlain, D., Green, K.S., Philipp, H.T., Purohit, P., Strohman, C. & Gruner, S.M. (2013). A Medium-Format, Mixed-Mode Pixel Array Detector for Kilohertz X-ray Imaging. 11th International Conference on Synchrotron Radiation Instrumentation (SRI 2012) **425**, 062004.

[32] Vernon, W., Allin, M., Hamlin, R., Hontz, T., Nguyen, D., Augustine, F., Gruner, S.M., Xuong, N.H., Schuette, D.R., Tate, M.W. & Koerner, L.J. (2007). First results from the 128x128 pixel mixed-mode Si x-ray detector chip - art. no. 67060U. Hard X-Ray and Gamma-Ray Detector Physics IX **6706**, U7060-U7060.

[33] Gauvin, R., Lifshin, E., Demers, H., Horny, P. & Campbell, H. (2006). Win X-ray: A New Monte Carlo Program that Computes X-ray Spectra Obtained with a Scanning Electron Microscope. Microscopy and Microanalysis **12**(01), 49-64.

[34] McMullan, G., Chen, S., Henderson, R. & Faruqi, A.R. (2009). Detective quantum efficiency of electron area detectors in electron microscopy. Ultramicroscopy **109**(9), 1126-1143.

[35] LeBeau, J.M., Findlay, S.D., Allen, L.J. & Stemmer, S. (2010). Standardless Atom Counting in Scanning Transmission Electron Microscopy. Nano Letters **10**(11), 4405-4408.

[36] Lubk, A. & Zweck, J. (2015). Differential phase contrast: An integral perspective. Physical Review A **91**(2), 023805.

[37] Majert, S. & Kohl, H. (2015). High-resolution STEM imaging with a quadrant detector Conditions for differential phase contrast microscopy in the weak phase object approximation. Ultramicroscopy **148**, 81-86.

[38] Rose, H. (1976). Nonstandard imaging methods in electron microscopy. Ultramicroscopy **2**, 251-267.

[39] Waddell, E.M. & Chapman, J.N. (1979). Linear Imaging Of Strong Phase Objects Using Asymmetrical Detectors In STEM. Optik **54**(2), 83-96.

[40] Chapman, J.N., Batson, P.E., Waddell, E.M. & Ferrier, R.P. (1978). The direct determination of magnetic domain wall profiles by differential phase contrast electron microscopy. Ultramicroscopy **3**(0), 203-214.

[41] Muller, K., Krause, F.F., Beche, A., Schowalter, M., Galioit, V., Loffler, S., Verbeeck, J., Zweck, J., Schattschneider, P. & Rosenauer, A. (2014). Atomic electric fields revealed by a quantum mechanical approach to electron picodiffraction. Nature Communications **5**, 5653.1-6.

[42] Rose, H. (1974). Phase-Contrast In Scanning-Transmission Electron-Microscopy. Optik **39**(4), 416-436.

[43] MacLaren, I., Wang, L.Q., McGrouther, D., Craven, A.J., McVitie, S., Schierholz, R., Kovacs, A., Barthel, J. & Dunin-Borkowski, R.E. (2015). On the origin of differential phase contrast at a locally charged and globally charge-compensated domain boundary in a polar-ordered material. Ultramicroscopy **154**, 57-63.

[44] Dekkers, N.H. & Lang, H.D. (1974). Differential Phase-Contrast In A STEM.

Optik **41**(4), 452-456.

[45] Takahashi, Y. & Yajima, Y. (1994). Nonmagnetic contrast in scanning Lorentz electron microscopy of polycrystalline magnetic films. Journal Of Applied Physics **76**(12), 7677-7681.

[46] Yajima, Y. (2009). Lorentz Scanning Transmission Electron Microscopy (Lorentz STEM): Model Analyses of Detector Performance. Bull. Col. Edu. Ibaraki Univ. (Nat. Sci.) **58** 19-24

[47] N. Nagaosa and Y. Tokura, Nat Nanotechnol **8** (12), 899-911 (2013).

[48] X. Z. Yu, N. Kanazawa, Y. Onose, K. Kimoto, W. Z. Zhang, S. Ishiwata, Y. Matsui and Y. Tokura, Nature Materials **10**, 106 (2010).

[49] X. Z. Yu, Y. Onose, N. Kanazawa, J. H. Park, J. H. Han, Y. Matsui, N. Nagaosa and Y. Tokura, Nature **465** (7300), 901-904 (2010).

[50] J. N. Chapman, E. M. Waddell, P. E. Batson and R. P. Ferrier, Ultramicroscopy **4** (3), 283-292 (1979).

[51] T. Matsumoto, Y. G. So, Y. Kohno, H. Sawada, R. Ishikawa, Y. Ikuhara and N. Shibata, Sci Rep-Uk **6** (2016).

[52] R. Close, Z. Chen, N. Shibata and S. D. Findlay, Ultramicroscopy **159**, 124-137 (2015).

[53] Emori, S., Bauer, U., Ahn, S.M., Martinez, E., and Beach, G. S. D. (2013). Current-driven dynamics of chiral ferromagnetic domain walls. Nature Materials, **12**, 611-616.

[54] Fert, A., Cros, V., and Sampaio, J. (2013). Skyrmions on the track. Nature Nanotechnology, **8**, 152 -156.

[55] Hrabec, A., Porter, N. A., Wells, A., Benitez, M. J., Burnell, G., McVitie, S., McGrouther, D., Moore, T. A., and Marrows, C. H. (2014)., Measuring and tailoring the Dzyaloshinkii-Moriya interaction in perpendicular magnetized thin films. Physical Review B, **90**, 1-5.

[56] I. Dzyaloshinsky, J Phys Chem Solids **4** (4), 241-255 (1958).

[57] E. Turgut, A. Park, K. Nguyen, A. Moehle, D. A. Muller and G. D. Fuchs, Phys Rev B **95** (13) (2017).

[58] T. Matsumoto, Y. G. So, Y. Kohno, H. Sawada, R. Ishikawa, Y. Ikuhara and N. Shibata, Sci Rep-Uk **6** (2016).

[59] J. N. Chapman, I. R. Mcfadyen and S. Mcvitie, Ieee T Magn **26** (5), 1506-1511 (1990).

[60] M. Krajnak, D. McGrouther, D. Maneuski, V. O'Shea and S. McVitie, Ultramicroscopy **165**, 42-50 (2016).

[61] Michael C. Cao, Yimo Han, Zhen Chen, Yi Jiang, Kayla X. Nguyen, Emrah Turgut, Gregory D. Fuchs, David A. Muller, Theory and Practice of Electron Diffraction from Single Atoms and Extended Objects Using an EMPAD. Microscopy, 67: i150 – i161, 2018.

[62] S. X. Huang and C. L. Chien, Phys Rev Lett **108** (26) (2012).

[63] A. Vansteenkiste, J. Leliaert, M. Dvornik, M. Helsen, F. Garcia-Sanchez and B. Van Waeyenberge, Aip Adv **4** (10) (2014).

[64] E. A. Karhu, U. K. Rossler, A. N. Bogdanov, S. Kahwaji, B. J. Kirby, H. Fritzsche, M. D. Robertson, C. F. Majkrzak and T. L. Monchesky, Phys Rev B **85** (9) (2012).

[65] M. N. Wilson, A. B. Butenko, A. N. Bogdanov and T. L. Monchesky, Phys Rev B **89** (9) (2014).

[66] M. N. Wilson, E. A. Karhu, D. P. Lake, A. S. Quigley, S. Meynell, A. N. Bogdanov, H. Fritzsche, U. K. Rossler and T. L. Monchesky, Phys Rev B **88** (21) (2013).

[67] N. A. Porter, C. S. Spencer, R. C. Temple, C. J. Kinane, T. R. Charlton, S. Langridge and C. H. Marrows, Phys Rev B **92** (14) (2015).

[68] J. C. Gallagher, K. Y. Meng, J. T. Brangham, H. L. Wang, B. D. Esser, D. W. McComb and F. Y. Yang, Phys Rev Lett **118** (2) (2017).

[69] Choudhury, N., Walizer, L., Lisenkov, S. & Bellaiche, L. Geometric frustration in compositionally modulated ferroelectrics. *Nature* **470**, 513-517, (2011).

[70] Martin, L. W. & Rappe, A. M. Thin-film ferroelectric materials and their applications. *Nature Reviews Materials* **2**, (2016).

[71] Nahas, Y., Prokhorenko, S., Louis, L., Gui, Z., Kornev, I. & Bellaiche, L. Discovery of stable skyrmionic state in ferroelectric nanocomposites. *Nat Commun* **6**, (2015).

[72] Hong, J., Catalan, G., Fang, D. N., Artacho, E. & Scott, J. F. Topology of the polarization field in ferroelectric nanowires from first principles. *Physical Review B* **81**, 172101, (2010).

[73] Prosandeev, S., Ponomareva, I., Naumov, I., Kornev, I. & Bellaiche, L. Original properties of dipole vortices in zero-dimensional ferroelectrics. *Journal of Physics: Condensed Matter* **20**, 193201, (2008).

[74] Hans, S. Some symmetry aspects of ferroics and single phase multiferroics *.

Journal of Physics: Condensed Matter **20**, 434201, (2008).

[75] Naumov, I. I., Bellaiche, L. & Fu, H. Unusual phase transitions in ferroelectric nanodisks and nanorods. *Nature* **432**, 737-740, (2004).

[76] Baudry, L., Sené, A., Luk'yanchuk, I. A., Lahoche, L. & Scott, J. F. Polarization vortex domains induced by switching electric field in ferroelectric films with circular electrodes. *Physical Review B* **90**, 024102, (2014).

[77] Yadav, A. K., Nelson, C. T., Hsu, S. L., Hong, Z., Clarkson, J. D., Schlepüetz, C. M., Damodaran, A. R., Shafer, P., Arenholz, E., Dedon, L. R., Chen, D., Vishwanath, A., Minor, A. M., Chen, L. Q., Scott, J. F., Martin, L. W. & Ramesh, R. Observation of polar vortices in oxide superlattices. *Nature* **530**, 198-201, (2016).

[78] Chen, W. J., Zheng, Y. & Wang, B. Large and Tunable Polar-Toroidal Coupling in Ferroelectric Composite Nanowires toward Superior Electromechanical Responses. **5**, 11165, (2015).

[79] Shafer, P., García-Fernández, P., Aguado-Puente, P., Damodaran, A. R., Yadav, A. K., Nelson, C. T., Hsu, S.-L., Wojdeł, J. C., Íñiguez, J., Martin, L. W., Arenholz, E., Junquera, J. & Ramesh, R. Emergent chirality in the electric polarization texture of titanate superlattices. *Proceedings of the National Academy of Sciences*, (2018).

[80] Nelson, C. T., Winchester, B., Zhang, Y., Kim, S., Melville, A., Adamo, C., Folkman, C. M., Baek, S. H., Eom, C. B., Schlom, D. G., Chen, L. Q. & Pan, X. Spontaneous Vortex Nanodomain Arrays at Ferroelectric Heterointerfaces. *Nanoletters* **11**, 828-834, (2011).

[81] Nguyen, K. X., Hovden, R., Tate, M. W., Purohit, P., Heron, J., Chang, C.,

Gruner, S. M. & Muller, D. A. Lorentz-STEM imaging of Fields and Domains using a High-Speed, High-Dynamic Range Pixel Array Detector at Atomic Resolution. *Microsc. Microanal.* **21 (S3)**, 2309, (2015).

[82] Jiang, Y., Chen, Z., Han, Y., Deb, P., Gao, H., S. Xie, Purohit, P., Tate, M. W., Park, J., Gruner, S. M., Elser, V. & Muller, D. A. Deep Sub-Angstrom Imaging of 2D Materials with a High Dynamic Range Detector (2018). Nature, **559**, 343 -349.

[83] Zuo, J. M. & Spence, J. C. H. *Electron Microdiffraction*. 1st edn, (Springer US, 1993).

[84] Kittel, C. *Introduction to Solid State Physics*. 8th edn, (Wiley, 2005).

[85] King-Smith, R. D. & Vanderbilt, D. Theory of polarization of crystalline solids. *Physical Review B* **47**, 1651-1654, (1993).

[86] Bijvoet, J. M., Peerdeman, A. F. & van Bommel, A. J. Determination of the Absolute Configuration of Optically Active Compounds by Means of X-Rays. *Nature* **168**, 271-272, (1951).

[87] Berger, L. Emission of spin waves by a magnetic multilayer traversed by a current. *Physical Review B* **54**, 9353-9358, (1996).

[88] Myers, E. B., Ralph, D. C., Katine, J. A., Louie, R. N. & Buhrman, R. A. Current-Induced Switching of Domains in Magnetic Multilayer Devices. *Science* **285**, 867-870, (1999).

[89] Slonczewski, J. C. Current-driven excitation of magnetic multilayers. *Journal of Magnetism and Magnetic Materials* **159**, L1-L7, (1996).

[90] Tsoi, M., Jansen, A. G. M., Bass, J., Chiang, W. C., Seck, M., Tsoi, V. & Wyder, P. Excitation of a Magnetic Multilayer by an Electric Current. *Physical*

Review Letters **80**, 4281-4284, (1998).

[91] Damodaran, A. R., Clarkson, J. D., Hong, Z., Liu, H., Yadav, A. K., Nelson, C. T., Hsu, S. L., McCarter, M. R., Park, K. D., Kravtsov, V., Farhan, A., Dong, Y., Cai, Z., Zhou, H., Aguado-Puente, P., Garcia-Fernandez, P., Iniguez, J., Junquera, J., Scholl, A., Raschke, M. B., Chen, L. Q., Fong, D. D., Ramesh, R. & Martin, L. W. Phase coexistence and electric-field control of toroidal order in oxide superlattices. *Nat Mater* **16**, 1003-1009, (2017).

[92] McMorran, B. J., Agrawal, A., Anderson, I. M., Herzing, A. A., Lezec, H. J., McClelland, J. J. & Unguris, J.

[93] Verbeeck, J., Tian, H. & Schattschneider, P. Production and application of electron vortex beams. *Nature* **467**, 301-304, (2010).

[94] Uchida, M. & Tonomura, A. Generation of electron beams carrying orbital angular momentum. *Nature* **464**, 737-739, (2010).

[95] Kirkland, E. J. *Advanced Computing in Electron Microscopy*. (Plenum, 1998).

[96] Grillo, V., Gazzadi, G. C., Karimi, E., Mafakheri, E., Boyd, R. W. & Frabboni, S. Highly efficient electron vortex beams generated by nanofabricated phase holograms. *Applied Physics Letters* **104**, 043109, (2014).

[97] Humphry, M. J., Kraus, B., Hurst, A. C., Maiden, A. M. & Rodenburg, J. M. Ptychographic electron microscopy using high-angle dark-field scattering for sub-nanometre resolution imaging. *Nat Commun* **3**, 730, (2012).

[98] Rodenburg, J. M. & Bates, R. H. T. The Theory of Super-Resolution Electron Microscopy Via Wigner-Distribution Deconvolution. *Philosophical Transactions of the Royal Society of London A: Mathematical, Physical and Engineering Sciences*

339, 521-553, (1992).

[99] Chen, W. J., Zheng, Y. & Wang, B. Large and Tunable Polar-Toroidal Coupling in Ferroelectric Composite Nanowires toward Superior Electromechanical Responses. **5**, 11165, (2015).

[100] Zhirnov V. V., and Cavin, R. K., Nature Nanotechnology **3**, 77-78 (2008).

[101] Lazić, I., Bosch, E. G. T. & Lazar, S. Phase contrast STEM for thin samples: Integrated differential phase contrast. *Ultramicroscopy* **160**, 265-280, (2016).

[102] Zuo, J. M. & Spence, J. C. H. *Electron Microdiffraction*. 1st edn, (Springer US, 1993).

[103] Georgakopoulos, A., Scattering and Magnetic Deflection Simulations, Master of Engineering Research, Cornell University (2012).